Université Catholique de Louvain
Faculté des Sciences Appliquées
Département d'ingénierie mathématique

SPECTRAL SCHEME FOR ANALYSIS OF DYNAMIC DELAMINATION OF A THIN FILM

Advisors :

Prof. Philippe H. Geubelle
Prof. Issam Doghri

Undergraduate thesis presented for the obtention of the grade of Ingénieur Civil en Mathématiques Appliquées by

Julien Hendrickx

June 2004

Acknowledgments

I am very grateful to Prof. Philippe H. Geubelle for giving me the opportunity of doing my undergraduate thesis in the University of Illinois at Urbana-Champaign and for his guidance and availability throughout all my research. I would also like to thank Prof. Issam Doghri and Dr. Laurent Delannay for their help in Belgium.

I want to thank Dr. Spandan Maiti, Soma Kandula, Varma Dantuluri, Helen Hinglis and my other labmates for their help and advices at various stages of the redaction of my thesis. I also want to thank Scot Breitenfeld for his help on the use of the computer system.

Finally, I would like to thank my parents and my sister for their support during all my studies. I want to thank Sylvie, and also all the friends who supported me during this year.

Contents

Chapter 1

Introduction

Thin film applications are increasingly prevalent in engineering applications. They are crucial components in a wide range of multilayer microelectronic and optical devices and are also desirable candidates for micro-actuators in micro-electro-mechanical devices. In the design of such devices, Interfacial adhesion is a critical parameter governing the mechanical behavior and reliability of a thin film on a substrate. Understanding the possible propagation of the delamination cracks along the interface between the thin film and the substrate and extracting the interface failure properties are therefore important.

Various experimental techniques have been proposed to extract delamination properties of thin films. The most common are the scratch test [1] [2] [3], peel test [4] [5], pull test [3] [6] [7], blister test [8] [9], and indentation test [10] [11]. One of the most successful recent additions to this list is the laser-induced spallation test shown schematically in Figure 1.1 for the tensile delamination case [12]. A laser pulse is sent on a metallic absorbing layer sandwiched between a confining layer and the substrate. This results in the emission from the metallic layer of a compressive stress wave of rise time comparable to that of the laser pulse. This stress wave then propagates towards the film/substrate interface, is reflected off the traction free surface of the thin film and loads the interface in tension. This technique load thus the interface in a precise and non-contacting manner. A mode II shear loading can be obtained using a reflection off an oblique surface, as shown in Figure 1.2. Figure 1.3 shows an example of the obtained damage after the spallation of a thin aluminium film deposited on a silica substrate.

The analysis supporting these laser induced spallation experiments has so far been based on the propagation of 1-D waves [12]. However, this assumption breaks down as soon as the initial failure takes place, since the problem then becomes 2-D. More advanced tools are thus needed and the development of such a tool is the primary objective of this work. In the simulation of fracture propagation in infinite media, the spectral formulation has prove to be one of

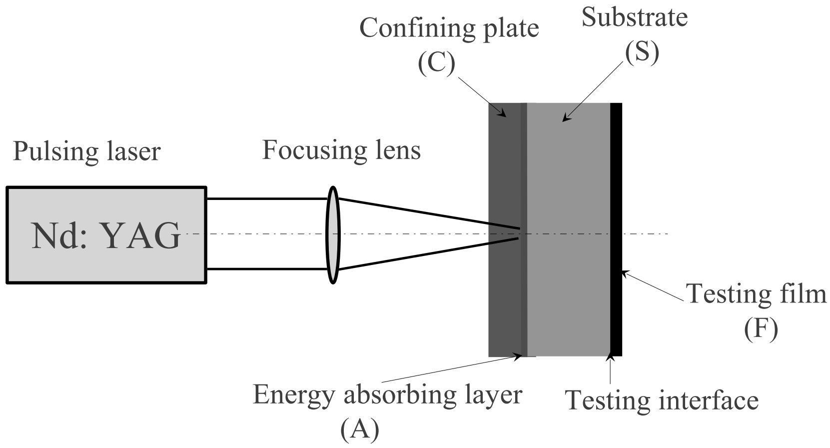

Figure 1.1: Experimental setup used in [12] to analyze the delamination of a thin film in mode I.

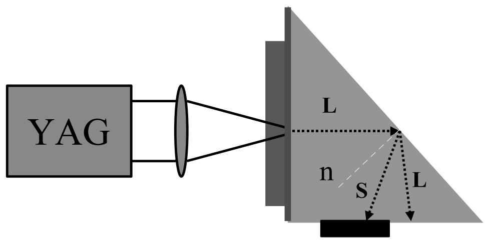

Figure 1.2: Experimental setup used in [12] to analyze the delamination of a thin film under shear.

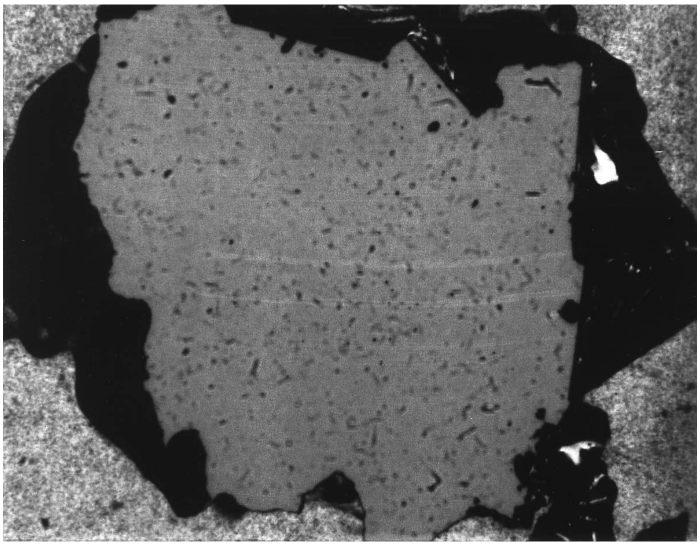

Figure 1.3: Damage observed for 1.2 μm thick aluminium film deposited on 600 μm thick silicon substrate. Taken from [12].

the most efficient tools. It was used to analyze the behavior of a fracture propagating in an infinite 2-D medium under an anti-plane shear loading [13], or at the interface between two different semi-infinite materials [14]. It also provides a way to analyze propagation of crack in a 3-D infinite material [15] or at the interface between two semi-infinite materials [16]. The objective of this project is to propose a spectral formulation for the thin film delamination problem. In this initial "feasibility study", we only consider the mode III problem, i.e., the case of an anti-plane shear loading. This problem is chosen because, although it captures most of the wave propagation characteristics of the in-plane cases, its mathematical treatment is somewhat simpler.

In Chapter 2, we present the problem description and derive the spectral formulation of the elastodynamic relations for the thin film and the substrate. Two formulations are considered for the thin film, the first involves two convolutions with the applied load and the interface displacement. However, in this formulation, the convolution kernels do not decay to zero and contain an infinite number of discontinuities. The second formulation involves an additional convolution with the traction stress at the interface. Despite the additional computational work that this formulation implies, it is attractive because it involves smoother, decaying convolution kernels that are much easier to manipulate. We then analyze the stability and accuracy of our formulation in Chapter 3, and address instability issues in Chapter 4. This analysis is done by comparing the results of our simulations with the analytical solution for the single-mode case, for which there is no fracture, and the loading has only one mode, and by analyzing some simple thin film fracture cases. We also derive in Chapter 5 a spectral scheme able to analyze the behavior of the external boundary of the thin film where measurements are made in the laser induced spallation experiments. We apply then our spectral scheme to some practical situations involving a fused silica substrate and an aluminium thin film. In Chapter 6, we treat the case of a non-propagating crack and analyze the evolution stress intensity factor (SIF) characterizing the near-tip stress field, while we consider in Chapter 7 the case of a propagating crack. To show the effect of large differences between the material properties, we also consider systems involving aluminium and steel thin films and substrates. Finally, we extend our scheme to the case of materials of finite length in Chapter 8, and we show that this extended scheme is able to capture some very interesting boundary effects.

Chapter 2

Formulation and implementation

2.1 Description and general solution

As indicated earlier, our main goal is to analyze the behavior of a dynamic fracture event that takes place at the interface between a semi-infinite linearly elastic substrate and a linearly elastic thin film of thickness H subjected to a time- and space-dependent anti-plane shear load $\tau^H(x,t)$ along its external boundary (Figure 2.1). To reach this goal, our approach is similar to the independent formulation used in [14] to solve interface fracture problems: we derive a relation between the traction stress and the displacement along the interface for both materials, and then bind these relations with a cohesive failure model. To derive this relation, we use a Fourier transform in space and a Laplace transform in time to turn the elastodynamic partial differential equation (PDE) into an ordinary differential equation (ODE). Its solution gives us a way to link the Laplace transform of the Fourier transform of the traction stress and the displacement at the interface. We then perform the inverse transforms back in the space and time domains.

Let us define a Cartesian coordinate system such that the interface is given by $y = 0$ (Figure 2.1). Inside both materials, following the anti-plane shear-assumption, the only non-vanishing displacement component $u_z(x, y, t)$ is independent of the z-coordinate and satisfies the scalar wave equation

$$c_s^2 \left(u_{z,xx} + u_{z,yy}\right) = \ddot{u}_z. \tag{2.1}$$

where a superposed dot means a derivation with respect to the time, and $*_{,\alpha}$ means $\frac{\partial *}{\partial \alpha}$. The shear wave speed c_s that appears in the previous equation is given by

$$c_s = \sqrt{\frac{\mu}{\rho}},$$

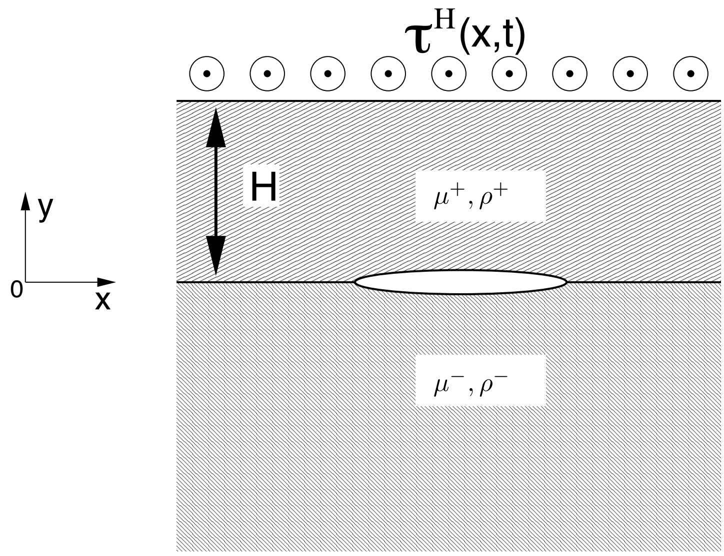

Figure 2.1: Geometry of the mode III interface fracture problem.

where μ denotes the shear modulus and ρ the density. Since these parameters are material-dependent, we use (μ^+, ρ^+, c_s^+) for the thin film, (μ^-, ρ^-, c_s^-) for the substrate, and (μ, ρ, c_s) when the equation can be applied to both of them. The same convention is used for the displacements and stresses.

If $\Omega(y, t; q)$ is the Fourier transform of $u_z(x, y, t)$ with respect to the x-coordinate, we get

$$\ddot{\Omega} = c_s^2 \left(-q^2\Omega + \Omega_{,yy}\right).$$

Taking a Laplace transform with respect to time, we rewrite the wave equation as

$$\hat{\Omega}_{,yy} = q^2 \alpha_s^2 \hat{\Omega}, \tag{2.2}$$

where $\hat{\Omega} = \mathscr{L}(\Omega)$ and

$$\alpha_s = \sqrt{1 + \frac{p^2}{q^2 c_s^2}}.$$

The general solution of this linear ODE is given by

$$\hat{\Omega}(y; p, q) = \hat{A}(p, q) e^{|q|\alpha_s y} + \hat{B}(p, q) e^{-|q|\alpha_s y}. \tag{2.3}$$

Since, as we mentioned before, we are mainly interested in the behavior along the interface plane, let us define the interface displacement $u(x, t)$ and traction stress $\tau(x, t)$ as

$$\left\{ \begin{array}{lll} u(x,t) & = & u_z(x, y=0, t), \\ \tau(x,t) & = \mu & u_{z,y}(x, y=0, t). \end{array} \right.$$

In the Fourier/Laplace domain, these quantities are expressed as

$$\begin{cases} \hat{U}(q,p) & = & \hat{\Omega}(y=0;q,p), \\ \hat{T}(q,p) & = \mu & \hat{\Omega}_{,y}(y=0;q,p), \end{cases}$$

so that, using (2.3), we get

$$\begin{cases} \hat{U} & = & \hat{A} & + & \hat{B} \\ \hat{T} & = & \mu\,|q|\,\alpha_s\hat{A} & - & \mu\,|q|\,\alpha_s\hat{B} \quad . \end{cases} \tag{2.4}$$

Since we want to link $\hat{T}$ and $\hat{U}$, we need one more relation, which is provided by the boundary condition at $y \to -\infty$ for the substrate and at $y = H$ for the thin film, as described in the next two sections.

2.2 Solution in the substrate

Since the substrate is a semi-infinite medium, we need to keep the value of u_z bounded when $y \to -\infty$, which translates to $\hat{B} = 0$ in (2.3). We can then eliminate $\hat{A}$ in (2.4) to obtain

$$\hat{T}^- = \mu^-\,|q|\,\alpha_s^-\hat{U}^-,$$

which can be reformulated by extracting the so-called radiation term [15] as

$$\hat{T}^- = \frac{\mu^-}{c_s^-}p\ \hat{U}^- + \mu^-\,|q|\left(\alpha_s^- - \frac{p}{|q|\,c_s^-}\right)\hat{U}^-. \tag{2.5}$$

We have now a relation between the traction stress and the displacement along the interface, which, in the time domain, takes the form

$$T^-(t;q) = \frac{\mu^-}{c_s^-}\ \dot{U}^-(t;q) + F^-(t;q),$$

where F^- denotes the result of the convolution of U^- and the inverse Laplace transform of the term in parenthesis in (2.5),

$$F^-(t;q) = \mu^-\,|q|\int_{-\infty}^{t} C_\infty(|q|\,c_s^- t')U^-(t-t';q)\,|q|\,c_s^- dt'. \tag{2.6}$$

The introduced convolution kernel is plotted Figure 2.2 and is defined by

$$C_\infty(T) = \mathscr{L}^{-1}\left(\sqrt{1+s^2} - s\right) = \frac{J_1(T)}{T}, \tag{2.7}$$

where J_1 denotes de Bessel function of the first kind.

Finally, an inverse Fourier transform back in the space domain yields the desired relation between u^- and τ^-,

$$\tau^-(x,t) - \frac{\mu^-}{c_s^-}\dot{u}^-(x,t) = f^-(x,t), \tag{2.8}$$

where $f^-(x,t) = \mathscr{F}^{-1}\left(F^-(t;q)\right)$ denotes the convolution term.

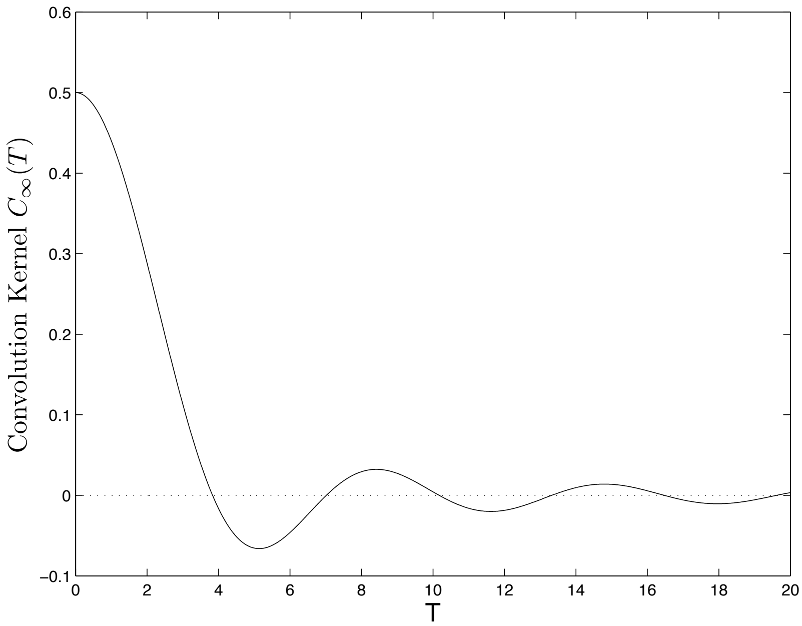

Figure 2.2: Convolution kernel for the substrate $C_\infty(T)$.

2.3 Solution in the thin film

The solution in the thin film can be expressed by two formulations. The first one is similar to the solution in the substrate and involves two convolutions. It is therefore referred to as the *two-convolution approach*. However the convolution kernels involved in this approach do not decay to zero and their complexity increase with time. In the second formulation, referred to as the *three-convolution approach*, an additional convolution is introduced on the traction stress history. The convolution kernels involved in this approach are however much simpler and decay to zero as time increases. This formulation is therefore preferred to the first one.

2.3.1 Two-convolution approach

As described in Section 2.1, an anti-plane shear traction $\tau^H(x,t)$ is applied at $y = H$. The corresponding boundary condition is thus

$$\tau^H(x,t) = \mu^+ u^+_{z,y}(x, y = H, t).$$

Taking again a Fourier transform with respect to the x-coordinate and then a Laplace Transform with respect to time, we obtain

$$\hat{T}^H(q,p) = \mu^+ \hat{\Omega}_{,y}(y = H; p, q).$$

Introducing the solution derived in (2.3), we get

$$\hat{T}^H(q,p) = \mu^+ |q| \alpha_s^+ \hat{A}(p,q) e^{|q|\alpha_s^+ H} - \mu^+ |q| \alpha_s^+ \hat{B}(p,q) e^{-|q|\alpha_s^+ H}. \tag{2.9}$$

We can use this last relation to eliminate $\hat{A}$ and $\hat{B}$ in (2.4),

$$\hat{T}^+ = -\mu^+ |q| \alpha_s^+ \tanh(a\alpha_s^+) \hat{U}^+ + \frac{1}{\cosh(a\alpha_s^+)} \hat{T}^H, \tag{2.10}$$

where the non-dimensional wave number a is defined by

$$a = |q| H.$$

Back in the time and space domain, relation (2.10) yields (see Appendix A.4)

$$\begin{array}{rlll} \tau^+(x,t) + \frac{\mu^+}{c_s^+} \dot{u}^+(x,t) = & +2\frac{\mu^+}{c_s^+} & \sum_{n=1}^{\infty} (-1)^{n-1} \dot{u}^+ \left(x, t - 2n\frac{H}{c_s^+} \right) & +f^+(x,t) \\ & +2 & \sum_{n=0}^{\infty} (-1)^n \tau^H \left(x, t - (2n+1)\frac{H}{c_s^+} \right) & +h^+(x,t), \end{array}$$

where the Fourier transform of the convolution terms are

$$\left\{ \begin{array}{lll} F^+(t;q) = & \mathscr{F}\left(f^+(x,t)\right) = & \mu^+ |q| \sum_{n=1}^{\infty} (-1)^n n a U^+ \left(t - 2n\frac{H}{c_s^+}; q \right) H(t - 2n\frac{H}{c_s^+}) \\ & & -\mu^+ |q| \int_0^t \left\{ C_\infty(|q| c_s^+ t') + C_{H2}(|q| c_s^+ t') \right\} U^+(t-t';q) |q| c_s^+ dt', \\ & & \\ H^+(t;q) = & \mathscr{F}\left(h^+(x,t)\right) = & -\int_0^t E_2(|q| c_s^+ t') T^H(t-t';q) |q| c_s^+ dt'. \end{array} \right. \tag{2.11}$$

The kernel C_∞ entering (2.11) has been defined in (2.7). The two other kernels are given by

$$\left\{ \begin{array}{ll} C_{H2}(T) & = 2\sum_{n=1}^{\infty} (-1)^n \left(\frac{J_1\left(\sqrt{T^2 - 4n^2a^2}\right)}{\sqrt{T^2 - 4n^2a^2}} + 4n^2a^2 \frac{J_2\left(\sqrt{T^2 - 4n^2a^2}\right)}{T^2 - 4n^2a^2} \right) H(T - 2na), \\ & \\ E_2(T) & = 2\sum_{n=0}^{\infty} (-1)^n (2n+1) a \frac{J_1\left(\sqrt{T^2 - (2n+1)^2a^2}\right)}{\sqrt{T^2 - (2n+1)^2a^2}} H\left(T - (2n+1)a\right), \end{array} \right. \tag{2.12}$$

where $H(t)$ denotes the Heaviside step function.

Looking at the two kernels defined by (2.12), we can see that new terms are added with a periodicity $2\frac{H}{c_s^+}$ and, as shown in Figure 2.3, each new term produces a discontinuity. This period corresponds to the time needed by a wave to cross the thin film, to be reflected off its upper boundary, and to come back to the interface. Moreover, because E_2 is convoluted with the anti-plane shear load applied along $y = H$, all its terms appear with a delay $\frac{H}{c_s^+}$, since it is the time needed for the information to reach the interface from the upper applied along the upper boundary of the thin film.

This periodic addition of new terms implies that the complexity of the kernels increases with time and that we need to keep in memory the whole history

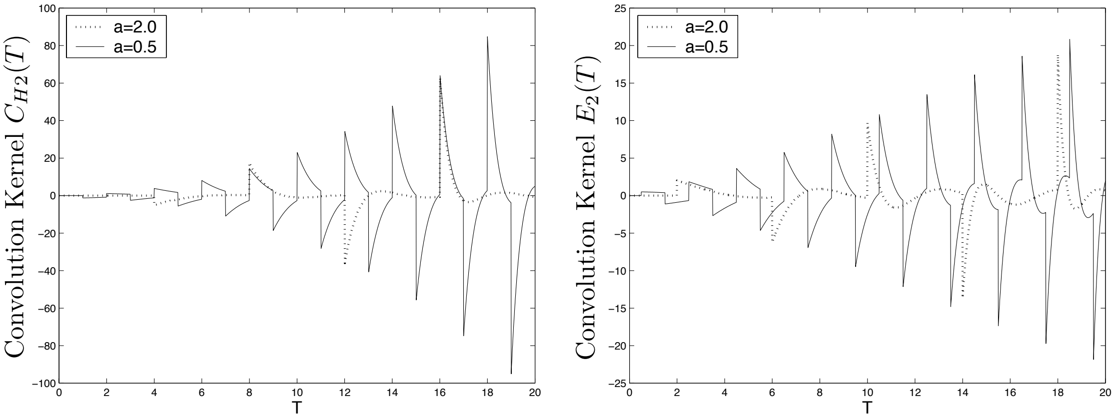

(a) (b)

Figure 2.3: Convolutions kernels appearing in the *two-convolution* formulation of the thin film solution for two values of the non-dimensional wave number a: (a) $C_{H2}(T)$, (b) $E_2(T)$. Unlike $C_\infty(T)$, they do not decay to zero, present an infinite number of discontinuities, and their complexity increases with time.

of the velocity, displacement and traction stress. In order to be efficiently implemented, this formulation needs thus to be improved. This can be done by transforming (2.10). A convolution with the applied shear stress is then introduced, but the three kernels are less complex and decay to zero when time increases.

2.3.2 Three-convolution approach

Since the cause of the infinite sum in (2.11) and (2.12) is the presence of a sum containing exponential functions of p in the denominators of (2.10), let us multiply this equation by $\left(1 + e^{-2\alpha_s^+ a}\right)$ to get

$$\left(1 + e^{-2\alpha_s^+ a}\right) \hat{T}^+ = \mu^+ \left|q\right| \alpha_s^+ \left(e^{-2\alpha_s^+ a} - 1\right) \hat{U}^+ + 2e^{-\alpha_s^+ a} \hat{T}^H. \tag{2.13}$$

Back in the time and space domain (see Appendix A.5), this yields

$$\begin{aligned} \frac{\mu^+}{c_s^+}\dot{u}^+(x,t) + \tau^+(x,t) \quad = & \quad\quad \frac{\mu^+}{c_s^+}\dot{u}^+(x,t-2\frac{H}{c_s^+}) \quad + \quad f^+(x,t) \\ & - \quad \tau^+(x,t-2\frac{H}{c_s^+}) \quad - \quad g^+(x,t) \\ & + \quad 2\tau^H(x,t-\frac{H}{c_s^+}) \quad + \quad h^+(x,t) \\ \doteq & \; l^+(x,t), \end{aligned} \tag{2.14}$$

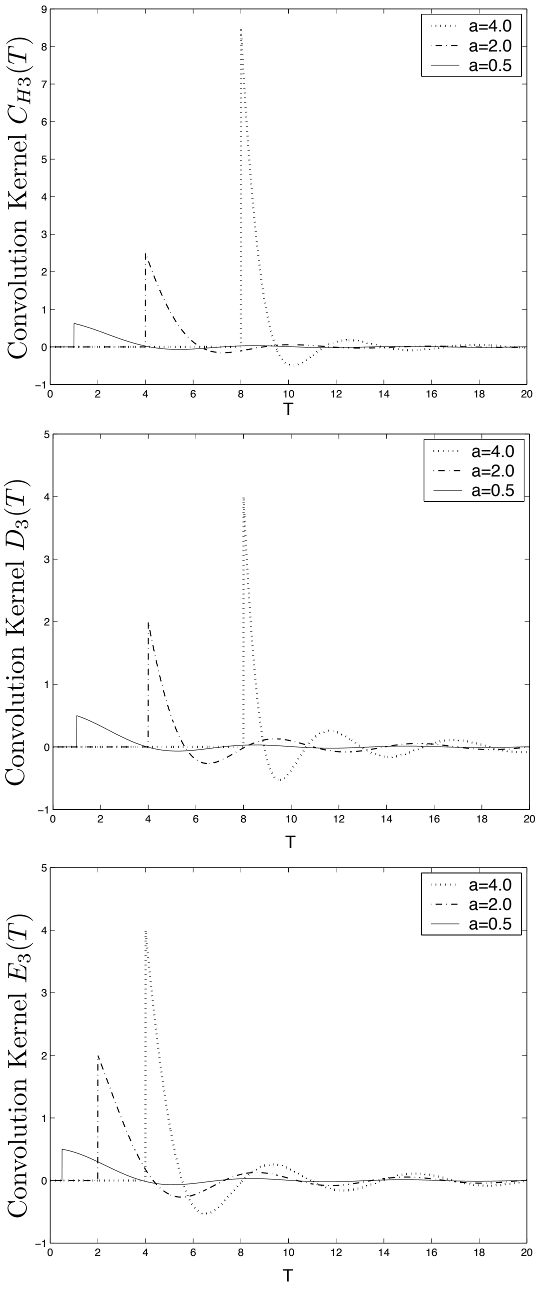

Figure 2.4: Convolution kernels $C_{H3}(T), D_3(T)$ and $E_3(T)$ specific to the *three-convolution* formulation for the thin film for three values of a. These kernels decay to zero and present only one discontinuity.

where the convolution terms are given in the Fourier domain by

$$\begin{cases} F^+(t;q) = & -\mu^+ \left|q\right| aU^+ \left(t - 2\frac{H}{c_s^+}; q\right) \\ & +\mu^+ \left|q\right| \int_0^t \left\{-C_\infty(\left|q\right| c_s^+ t') + C_{H3}(\left|q\right| c_s^+ t')\right\} U^+(t-t';q) \left|q\right| c_s^+ dt', \\ G^+(t;q) = & -\int_0^t D_3(\left|q\right| c_s^+ t') T^+(t-t';q) \left|q\right| c_s^+ dt', \\ H^+(t;q) = & -\int_0^t E_3(\left|q\right| c_s^+ t') T^H(t-t';q) \left|q\right| c_s^+ dt'. \end{cases} \tag{2.15}$$

The newly introduced kernels are

$$\begin{cases} C_{H3}(T) = \left(\frac{J_1\left(\sqrt{T^2-4a^2}\right)}{\sqrt{T^2-4a^2}} + 4a^2 \frac{J_2\left(\sqrt{T^2-4a^2}\right)}{T^2-4a^2}\right) H(T-2a), \\ D_3(T) = 2a \frac{J_1\left(\sqrt{T^2-4a^2}\right)}{\sqrt{T^2-4a^2}} H(T-2a), \\ E_3(T) = 2a \frac{J_1\left(\sqrt{T^2-a^2}\right)}{\sqrt{T^2-a^2}} H(T-a). \end{cases} \tag{2.16}$$

As shown in Figure 2.4, these kernels behave much better than those appearing in (2.11): they contain only one jump and decrease to zero when the value of T increases. One can also see that E_3 and $C_{H3}(T)$ are similar to E_2 and $C_{H2}(T)$ with only one reflection (i.e. with only the first two values of n).

2.4 Cohesive model

We have so far derived a relation between the traction stress $\tau^\pm(x,t)$ and the displacement $u^\pm(x,t)$ along the interface and their history, for each material independently. We now need to link these two solutions by a cohesive failure model, in a way similar to the independent formulation used in [14]. Since there is no external load applied on the interface, τ^+ is necessary equal to τ^-. If the two materials are connected, this results from the continuity of the traction, and if they are not, both surfaces are traction free. We designate thus $\tau^+ = \tau^-$ by τ.

To model the cohesive behavior of the interface, let us introduce the strength τ_{str} representing the maximal traction stress that can take place along the interface. In general, τ_{str} could depend on current and previous values of the slip between de two materials and its rate, and on space for non-uniform models. In the following, we adopt a simple linearly decreasing model illustrated in Figure 2.5:

$$\tau_{str} = \tau_{str0} \left(1 - \frac{|\delta|}{\delta_c}\right) H\left(\delta_c - |\delta|\right), \tag{2.17}$$

where $\delta(x,t) = u^+(x,t) - u^-(x,t)$ denotes the displacement jump or slip across the fracture plane, and the value of the critical slip δ_c and the initial strength

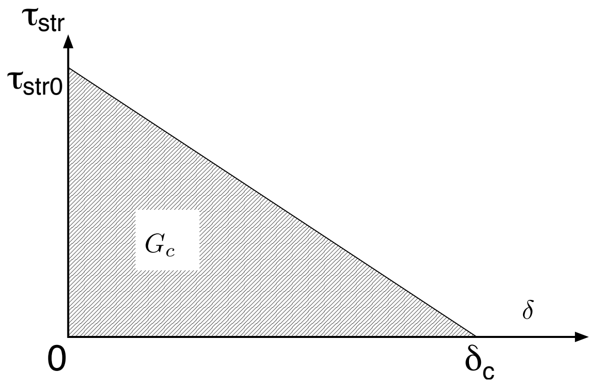

Figure 2.5: Cohesive strength τ_{str} versus slip $\delta = |u^+ - u^-|$. The grey zone represents the set of the possible $(\delta, |\tau|)$ with a non-null values of the norm of the traction stress. The area under the curve corresponds to the fracture toughness G_c.

τ_{str0} characterize the failure properties of the interface. Note that, to prevent the fracture surfaces from re-adhering, the strength should only be allowed to decrease. For this model, the fracture toughness G_c is given by $\frac{1}{2}\tau_{str0}\delta_c$

The traction stress along the interface can thus be determined by resolving the linear system provided by (2.8) and (2.14)

$$\begin{cases} \tau(x,t) - \frac{\mu^-}{c_s^-}\dot{u}^-(x,t) = f^-(x,t), \\ \tau(x,t) + \frac{\mu^+}{c_s^+}\dot{u}^+(x,t) = l^+(x,t), \end{cases} \tag{2.18}$$

assuming first that $\dot{u}^-(x,t) = \dot{u}^+(x,t)$. If the computed traction stress is larger than the strength given by (2.17), one replaces $\tau(x,t)$ by $\tau_{str}(x,t)$ and reintroduces this value in (2.18) to compute $\dot{u}^-(x,t)$ and $\dot{u}^+(x,t)$.

2.5 Implementation issues

To implement the spectral formulation derived in the previous sections, we need to discretize and limit the space and the frequencies. We consider thus the behavior of the interface on a length X represented by $N+1$ equidistant points. The gap between two consecutive points is thus $\Delta x = \frac{X}{N}$.

To link the space domain and the frequencies domain, we use a Discrete Fourier Transform and Inverse Transform,

$$\begin{array}{lcccl} X = \mathrm{DFT}(x) & \rightarrow & X(k) & = & \sum_{n=1}^{N} x(n)e^{-2\pi i(k-1)(n-1)/N} \\ x = \mathrm{DFT}^{-1}(X) & \rightarrow & x(n) & = \frac{1}{N} & \sum_{k=1}^{N} X(k)e^{2\pi i(k-1)(n-1)/N}. \end{array}$$

This automatically sets the discretization of the frequency domain,

$$q_0 = \frac{2\pi}{X}, \qquad q_j = jq_0, \quad j = 1, ..., N/2, \qquad q_{max} = \frac{2\pi}{\Delta x},$$

where q_{max} is the maximal frequency and q_0 is the smallest frequency and the discretization gap. Since all the used frequencies are integers multiple of q_0, the use of a discrete Fourier transform also implies that the problem that is really solved is periodic and results of the infinite juxtaposition of domains of length X. The last point behaves then exactly as the first one and needs therefore to have the same initial condition.

The time is also discretized with an uniform time step size Δt. The integration of the velocity used to compute the displacement is performed with an explicit first order scheme. As explained in [17], we need thus to satisfy the CFL condition $\beta < 1$, where

$$\beta \Delta x = \max\left(c_s^+, c_s^-\right) \Delta t. \tag{2.19}$$

We are now able to compute f^- and l^+. The main idea of the remainder of the spectral scheme is represented in the algorithm listed below, where $*_{(j,i)}$ denotes $*(x_j, t_i)$, and $*_{(j;k)}$ denotes $*(x_j, q_k)$

for each i **do** (loop over time steps)

- Perform FFT on $(u^+, u^-)_{(*,i)}, \tau_{(*,i)}, \tau^H_{(*,i)}$
- **for each** k **do** (loop over space modes)
  - Compute $L^+_{(j;k)}, F^-_{(j;k)}$ (sum of all the convolutions and the additional terms in the Laplace-Fourier domain)
- **end do**
- $(l^+, f^-)_{(j;*)} = FFT^{-1}(L^+, F^-)_{(j,*)}$
- **for each** j **do** (loop over space steps)
  - Solve (2.18) assuming $\dot{u}^+_{(j,i)} = \dot{u}^-_{(j,i)}$
  - **if** $\left|\tau_{(j,i)}\right| > \tau_{str}\left(u^+_{(j,i)} - u^-_{(j,i)}\right)$ **then**
    - $\tau_{(j,i)} := \tau_{str}\left(u^+_{(j,i)} - u^-_{(j,i)}\right)$
    - compute $(\dot{u}^+, \dot{u}^-)_{(j,i)}$ using (2.18)
  - **end if**
  - Update $(u^+, u^-)_{(j,i+1)} = (u^+, u^-)_{(j,i)} + (\dot{u}^+, \dot{u}^-)_{(j,i)}.\Delta t$
- **end do**

end do

Chapter 3

Modal analysis

In this chapter, we consider the case of a single-mode loading for which an analytical solution is available under certain conditions as explained Section 3.1. This allows us to understand the behavior of each mode, and also provides a tool to evaluate the precision and stability of our spectral scheme by comparing the numerical results to an exact solution.

3.1 Analytical solution

Let us consider the case of a perfect interface ($\tau_{str} = \infty$, $u^+ = u^- = u$) between materials having different stiffness ($\mu^+ \neq \mu^-$) but the same shear wave speed ($c_s^+ = c_s^- = c_s$). In the absence of fracture, all the equations are linear. If the applied load is

$$\tau^H(x,t) = \tau_0^H e^{iqx} H(t),$$

the interface displacement and the traction stress have the same x-dependence, and are expressed as

$$(u(x,t), \tau(x,t)) = (U(t), T(t))\, e^{iqx}.$$

Considering the linear system made by the juxtaposition of (2.5) and (2.10),

$$\begin{cases} \hat{T} = -\mu^+ \left|q\right| \alpha_s \tanh(a\alpha_s)\hat{U} + \frac{1}{\cosh(a\alpha_s^+)} \frac{\tau_0^H}{p} \\ \hat{T} = \frac{\mu^-}{c_s} p \;\; \hat{U} + \mu^- \left|q\right| \left(\alpha_s - \frac{p}{|q| c_s}\right) \hat{U}, \end{cases}$$

and eliminating $\hat{T}$ leads to

$$\tau_0^H = pq\hat{U}\left(\mu^- \alpha_s \cosh(\alpha_s a) + \mu^+ \alpha_s \sinh(\alpha_s a)\right).$$

An analytical expression of the velocity is thus

$$\dot{U} = \frac{\tau_0^H}{q} \mathscr{L}^{-1} \left(\frac{1}{\mu^- \alpha_s \sinh(\alpha_s a) + \mu^+ \alpha_s \cosh(\alpha_s a)} \right), \tag{3.1}$$

which, after the Laplace inversion (see Appendix A.3), can be written as

$$\dot{U}(t) = \frac{2\tau_0^H c_s}{\mu^+ + \mu^-} \sum_{n=0}^{\infty} \left(\left(\frac{\mu^+ - \mu^-}{\mu^+ + \mu^-} \right)^n J_0 \left(\sqrt{(qc_s t)^2 - (2n+1)^2 a^2} \right) H \left(|q|\, c_s t - (2n+1)a \right) \right). \tag{3.2}$$

Let us now introduce the non-dimensional velocity

$$r(t) = \frac{\dot{U}(t)}{\dot{U}(\frac{H}{c_s})},$$

where $\dot{U}(\frac{H}{c_s})$ is the velocity of the interface when the shear wave reaches it for the first time. Replacing U in (3.2) yields

$$r(t) = \sum_{n=0}^{\infty} \left(\left(\frac{\mu^+ - \mu^-}{\mu^+ + \mu^-} \right)^n J_0 \left(\sqrt{(qc_s t)^2 - (2n+1)^2 a^2} \right) H \left(|q|\, c_s t - (2n+1)a \right) \right). \tag{3.3}$$

3.2 Non-dimensional parameters

Using $t = i\Delta t$, the normalized time-discretized velocity along the interface can be rewritten as

$$r(i) = \sum_{n=0}^{\infty} \left(\Delta_\mu^n J_0 \left(a \sqrt{\left(\frac{i}{\eta} \right)^2 - (2n+1)^2} \right) H \left(\frac{i}{\eta} - (2n+1) \right) \right), \tag{3.4}$$

where we have (re-)introduced the three non-dimensional parameters entering this problem.

The first one is the *relative stiffness mismatch* Δ_μ

$$\Delta_\mu = \left(\frac{\mu^+ - \mu^-}{\mu^+ + \mu^-} \right).$$

By definition, $\Delta_\mu \in [-1, 1]$. A positive value means that the thin film is stiffer than the substrate, while a negative one denotes a more compliant thin film. Looking at (3.4), we can see that this parameter quantifies the decrease rate of the importance of the terms of the sum, and therefore of the amplitude of the jumps at each reflection.

The second parameter is the aforementioned *non-dimensional wave number* a

$$a = |q|\, H,$$

that influences the shape of the terms of the sum and thus the behavior of the solution between the jumps. For small values of the non-dimensional wave number, the solution is essentially flat; but for large values, it keeps oscillating.

The last parameter is the *time-discretization factor* η

$$\eta = \frac{H}{c_s \Delta t},$$

that represents the number of time steps needed for a wave to cross the thin film. Its value does not influence the shape of the solution, but only the precision of the discretiszation. Furthermore, for a same number of shear wave reflections, its value determines the total number of time steps.

3.3 Analytical solution for special cases

Before beginning an error analysis, let us look at the analytical solution (3.3) for some particular values of Δ_μ and for different values of a. To facilitate the discussion, we consider first the case $q = 0$ (i.e., $a = 0$) for which the problem is reduced to the well-known problem of the 1-D propagation of a shear wave and its reflection off an interface. The exact solution (3.3) for the non-dimensional velocity of the interface becomes

$$r(t) = \sum_{n=0}^{\tilde{n}(t)} \Delta_\mu^n, \tag{3.5}$$

where $\tilde{n}(t)$ is the number of reflections that have already occurred

$$\tilde{n}(t) = \lfloor \frac{1}{2} \left(\frac{q c_s t}{a} - 1 \right) \rfloor,$$

with $\lfloor z \rfloor$ denoting the largest integer lower or equal to z. If $\Delta_\mu \neq 1$, (3.5) can be rewritten as

$$r(t) = \frac{1 - \Delta_\mu^{\tilde{n}(t)+1}}{1 - \Delta_\mu},$$

and, in the particular case where $\Delta_\mu = 1$, $r(t) = \tilde{n}(t) + 1$.

3.3.1 Traction free interface $\Delta_\mu = 1$

$\Delta_\mu = 1$ implies that $\mu^- = 0$, which means that the lower boundary of the thin film is traction free. In this case, the solution for $q = 0$ is a sum of step functions of same amplitude, which average rate of increase is the one predicted by the rigid body approximation $\ddot{U} = \tau_0^H / \rho^+ H$, or $\dot{r} = c_s / 2H$ (Figure 3.1). The jump in velocities occurs at each reflection of the initial shear wave off the lower boundary. Since this boundary is traction free, there is no energy loss, which

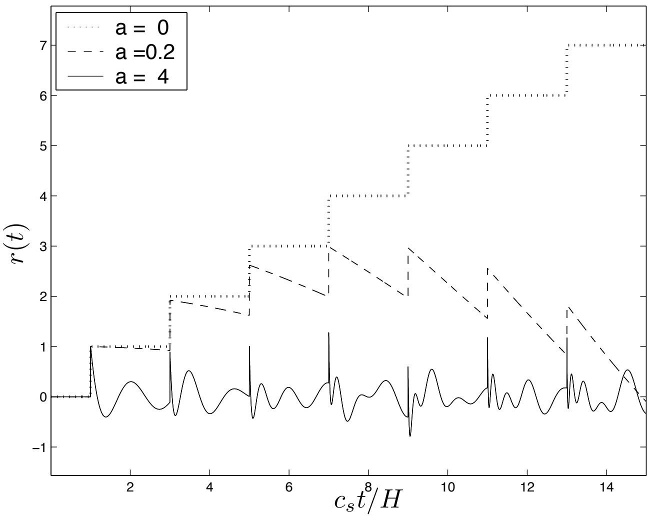

Figure 3.1: Exact solution of the single mode problem: evolution of the non-dimensional interface velocity $r(t)$ for various values of a when $\Delta_\mu = 1$. When $a = 0$, the velocity increases indefinitely at the rate predicted by the rigid body approximation.

explains the constant amplitudes of these jumps. For $q \neq 0$, the solution also has a constant amplitude jump at each reflection of the velocity wave off the lower boundary. However, the velocity does not increase indefinitely anymore.

3.3.2 Stiffer thin film $\Delta_\mu \in (0, 1)$

As indicated earlier, $\Delta_\mu \in (0, 1)$ implies that $\mu^+ > \mu^-$. When the wave reaches the interface a part is transmitted to the substrate and the rest is reflected. Since the thin film is stiffer than the substrate, the reflected velocity wave has the same sign as the incident one. Thus, when the wave comes back after being reflected off the upper boundary, it still has the same sign. Note that the transmitted wave never comes back since the thickness of the substrate is assumed infinite. But, since a part of the wave was transmitted to the substrate, the amplitude decreases at each reflection, following a geometric progression (Figure 3.2). The velocity converges thus monotonically to $\frac{\tau_0^H}{\mu^-} c_s$. We can notice that the stress converges to the stress applied on the upper boundary, in accordance to the static limit. The same behavior can be observed for the jumps when $q \neq 0$.

3.3.3 $\Delta_\mu = 0$

The case $\Delta_\mu = 0$ corresponds to the special situation where the thin film and the bottom material have the same properties ($\mu^+ = \mu^-$). Since no fracture

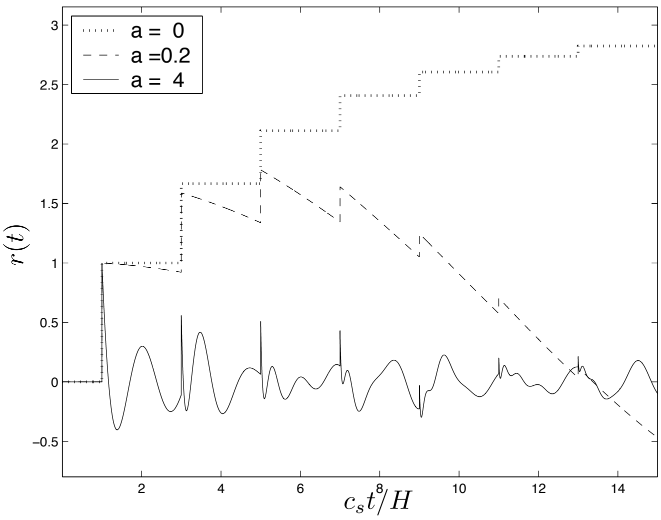

Figure 3.2: Exact solution of the single mode problem: evolution of the non-dimensional interface velocity $r(t)$ for various values of a when $\Delta_\mu = \frac{2}{3}$. For $a = 0$, the velocity converges monotonically to $\tau_0^H \frac{c_s}{\mu^-}$.

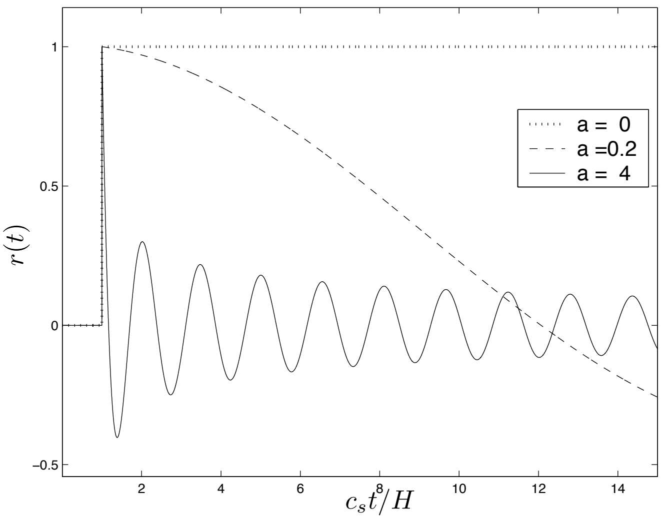

Figure 3.3: Exact solution of the single mode problem: evolution of the non-dimensional interface velocity $r(t)$ for various values of a when $\Delta_\mu = 0$. There is only one discontinuity corresponding to the arrival of the shear wave at $y = 0$, and, if $a = 0$, the velocity reaches immediately its limiting value $\tau_0^H \frac{c_s}{\mu}$.

takes place along the interface, its position is purely arbitrary. When the wave reaches it, it continues to propagate without any reflection. There is thus only one jump in the velocity, that occurs at $t = \frac{H}{c_s}$ (Figure 3.3). When $a \neq 0$, the velocity varies with time but presents only one discontinuity corresponding to the arrival of the shear wave at $y = 0$.

3.3.4 More compliant thin film $\Delta_\mu \in (-1, 0)$

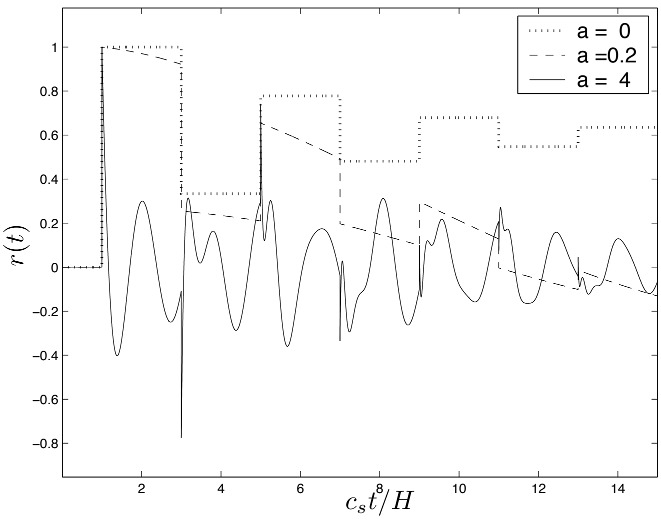

Figure 3.4: Exact solution of the single mode problem: evolution of the non-dimensional interface velocity $r(t)$ for various values of a when $\Delta_\mu = -\frac{2}{3}$. For $a = 0$, the velocity converges to $\tau_0^H \frac{c_s}{\mu^-}$, but this convergence is not monotonous.

In this case, $\mu^+ < \mu^-$. The behavior is similar to that observed in Section 3.3.2 except that since the thin film is more compliant than the substrate the reflected velocity wave has a sign opposite to that of the incident one. This implies the velocity jumps have alternating signs and that the convergence is not monotonous (Figure 3.4).

3.4 Error analysis

Having established the exact solution of the single-mode problem, we now turn our attention to quantifying the precision and stability of the three-convolution scheme described in Chapter 2. Figure 3.5 shows two examples of comparison between the analytical solution and numerical results and illustrates how instabilities may rise for small values of η, i.e., for large time step values Δt.

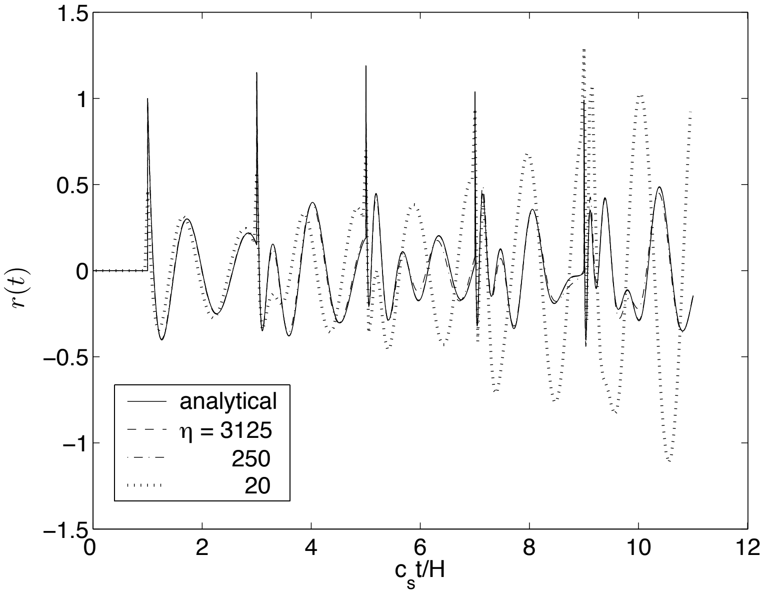

(a)

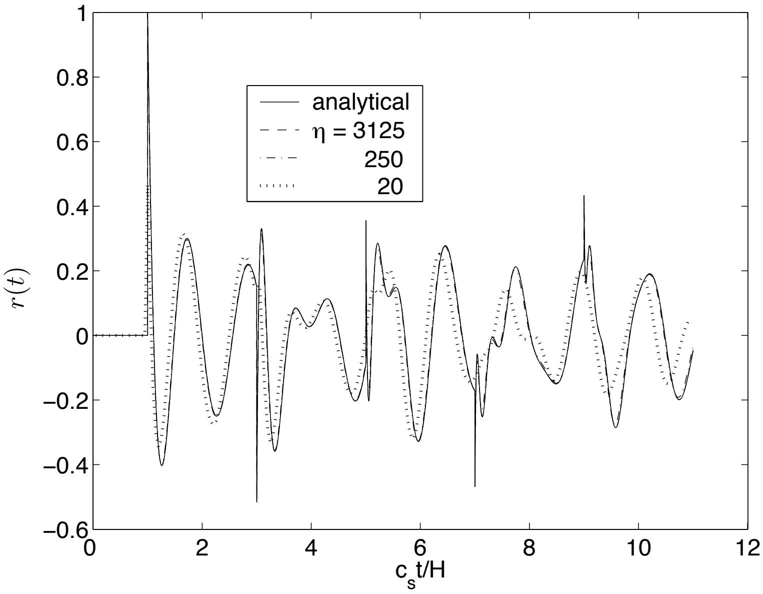

(b)

Figure 3.5: Results for the evolution of the non-dimensional interface velocity $r(t)$ for the single mode problem, with $a = 4.995$. (a) $\Delta_\mu = 1$, (b) $\Delta_\mu = -\frac{2}{3}$. Note the instabilities appearing when $\eta = 20$ for $\Delta_\mu = 1$.

To quantify the error, we use the internal mean square error computed on each period of time n corresponding to the time between the n^{th} and the $(n+1)^{th}$ reflections of the wave off the interface,

$$E_X^2(n) = \frac{c_s^+}{2X(1-\zeta)H} \int_X \int_{(-1+\zeta+2n)\frac{H}{c_s^+}}^{(1-\zeta+2n)\frac{H}{c_s^+}} \left|\dot{u}(x,t) - \tilde{\dot{u}}(x,t)\right|^2 dt.dx, \tag{3.6}$$

where $\dot{u}(x,t)$ is the exact interface velocity and $\tilde{\dot{u}}(x,t)$ is the velocity computed by the numerical simulation. The purpose of the parameter $\zeta \in [0,1]$ is to avoid the influence of some large errors taking place just after or before the reflections, due for example to a small delay between the jump in the analytical solution and the jump in the result of the numerical simulation. In the single mode case, this expression becomes

$$\epsilon^2(n) = \frac{1}{2(1-\zeta)\frac{H}{c_s^+}} \int_{(-1+\zeta+2n)\frac{H}{c_s^+}}^{(1-\zeta+2n)\frac{H}{c_s^+}} \left(r(t) - \tilde{r}(t)\right)^2 dt, \tag{3.7}$$

where $\tilde{r}(t)$ is the non-dimensional velocity computed by the simulation. The main advantage of this error measure appears in the case of a constant loading (in time) of the thin film with a perfect (i.e., non-failing) interface or in the limiting case of a free-standing thin film. In this case, the relative importance of each mode is constant and the velocity can thus be expressed as

$$\dot{u}(x,t) = \sum_q e^{iqx} r(t;q) \dot{U}\left(\frac{H}{c_s^+};q\right). \tag{3.8}$$

So, neglecting the errors produced by the discrete Fourier transform, we have

$$E_X^2(n) = \frac{1}{2(1-\zeta)\frac{H}{c_s^+}} \int_{(-1+\zeta+2n)\frac{H}{c_s^+}}^{(1-\zeta+2n)\frac{H}{c_s^+}} \left|\sum_q e^{iqx}\left(r(t) - \tilde{r}(t)\right)\dot{U}\left(\frac{H}{c_s^+};q\right)\right|^2 dt, \tag{3.9}$$

and, since the discrete mode numbers q_j are always multiple of the fundamental mode $q_0 = \frac{2\pi}{X}$,

$$E_X^2(n) = \sum_q \left|\dot{U}\left(\frac{H}{c_s^+};q\right)\right|^2 \epsilon^2(n). \tag{3.10}$$

We can thus obtain an approximation of the error at each period by performing a discrete Fourier transform on $\dot{u}\left(x_i, \frac{H}{c_s^+}\right)$.

If we consider the propagation of a crack, the zones of the interface that have not been reached yet by the crack behave as if the interface is perfect, while, inside the crack, the boundary of the thin film is traction free. We consider thus two limiting cases in our error analysis, the traction free case ($\Delta_\mu = 1$) and an example of perfect interface ($\Delta_\mu = -\frac{2}{3}$).

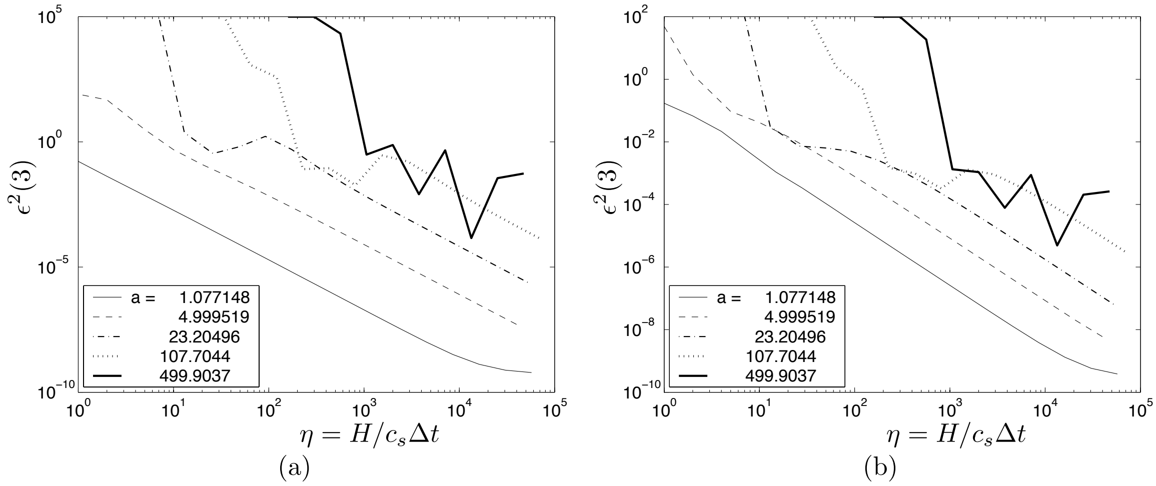

Figure 3.6: Evolution of the internal mean square error of the third period $\epsilon(3)$ with respect to η, for different values of a. (a) $\Delta_\mu = 1$, (b) $\Delta_\mu = -\frac{2}{3}$. For a large set of values of the parameters the error ϵ varies as $1/\eta$.

As shown in Figure 3.6, for a large set of values of the parameters (a, η), the evolution of the error is linear with η^{-1}; the evolution of ϵ^2 is thus quadratic. We can also see that larger values of a or Δ_μ usually imply a larger error (Figure 3.7), but this effect is hard to characterize and the dependance is not always monotonous. However, it is interesting to notice that the case $\Delta_\mu = 0$, corresponding to two materials with the same properties for the film and the substrate, is not optimal from the point of view of the error analysis.

It is also observed in Figure 3.8 that the error often increases geometrically with the period. This fact is true for any value of Δ_μ, but the rate of this progression is more important for large values of Δ_μ as shown in Figures 3.7 and 3.8, especially in the limiting case of the traction free interface (Δ_μ=1). This result is expected since this special case is physically unstable.

For large values of a, the solution becomes unstable after a few periods and eventually diverges totally, as shown in Figures 3.5, 3.6 and 3.8. It is obvious that increasing η delays the apparition of these instabilities, but it is not clear if one can always find a value of η such that the problem is always stable, or if one can always find a number of periods after which the simulation diverges.

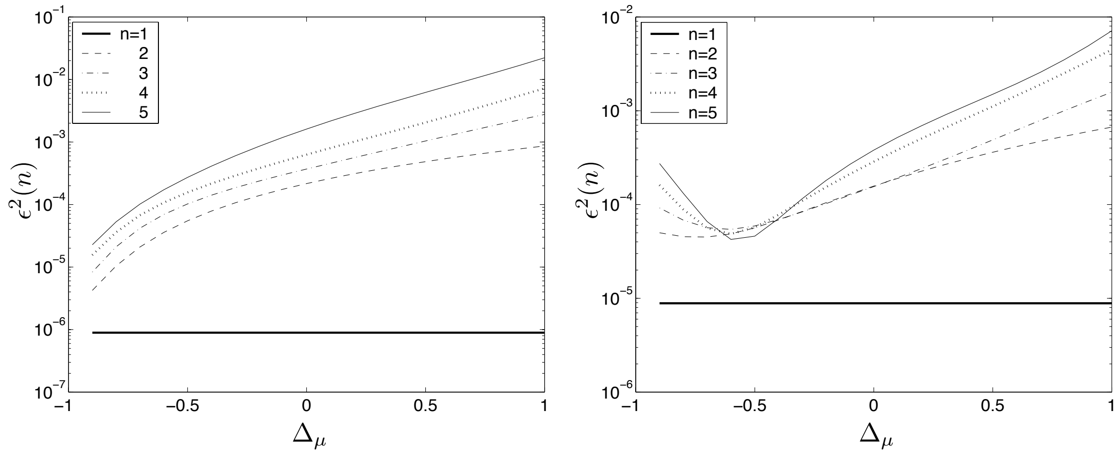

(a) (b)

Figure 3.7: Evolution of the internal mean square error $\epsilon^2(n)$ with respect to Δ_μ, for different periods n: (a) $a = 50$, $\eta = 5000$, (b) $a = 10$, $\eta = 500$. Note that the error increases with the number of reflections n, and that $\Delta_\mu = 0$ is not optimal from the error analysis point of view.

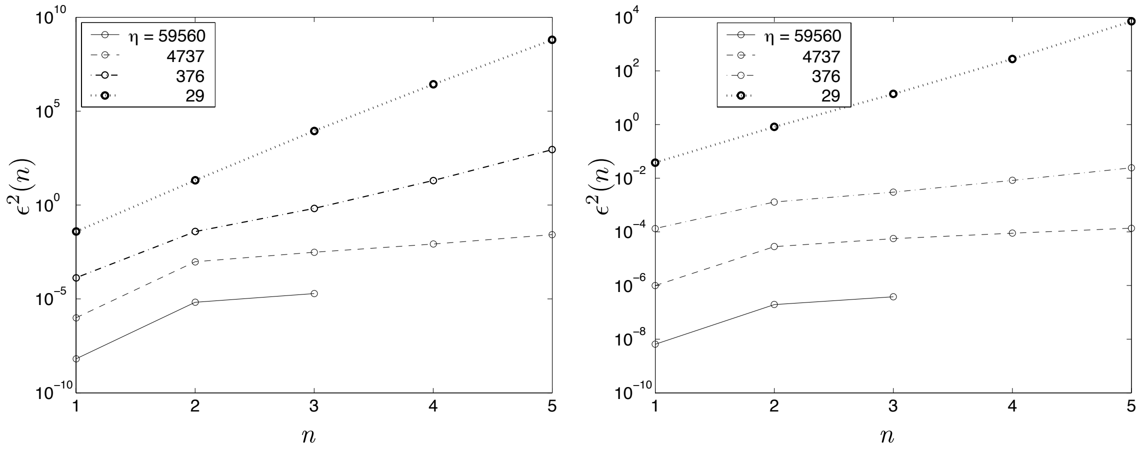

(a) (b)

Figure 3.8: Evolution of the internal mean square error $\epsilon^2(n)$ with respect to the number of reflections n for different values of η, showing a progressive increase of the error at each reflection: (a) $\Delta_\mu = 1$, (b) $\Delta_\mu = -\frac{2}{3}$.

Chapter 4

Stability and precision analysis

4.1 Origin of the instabilities

As shown in Figures 3.5, 3.7 and 3.8, during the first period (i.e. for $\frac{H}{c_s^+} \leq t \leq 3\frac{H}{c_s^+}$), the simulation matches the analytical solution very well even when this solution oscillates a lot. Furthermore, for small values of a, the errors are kept relatively small. This result seems to show that the source of the problem is to be found in the convolution terms F^+ or G^+ defined in (2.15). Note that the term H^+ could also be problematic, but since τ^H is constant in this analysis, its value is basically proportional to the mean value of E_3 on $[0, \frac{t}{|q|c_s^+}]$. This term has thus here no influence on the instabilities. Furthermore, for a varying τ^H, the behavior of H^+ would be similar to that of G^+.

Among the convolution terms, the term involving C_∞ does not lead to instability as long as the chosen time step does not violate the Courant condition, as in [13] and [14]. The four only terms that can lead to instability are thus, in the Fourier domain,

$$
\begin{aligned}
\#1 &= -\mu^+ |q|\, aU^+ \left(t - 2\tfrac{H}{c_s^+}\right), \\
\#2 &= \mu^+ q \int_{2\frac{H}{c_s^+}}^{t} \frac{J_1\left(\sqrt{(qc_s^+ t)^2 - 4a^2}\right)}{\sqrt{(qc_s^+ t)^2 - 4a^2}} U(t - t') q c_s^+ dt', \\
\#3 &= \mu^+ q \int_{2\frac{H}{c_s^+}}^{t} 4a^2 \frac{J_2\left(\sqrt{(qc_s^+ t)^2 - 4a^2}\right)}{(qc_s^+ t)^2 - 4a^2} U(t - t') q c_s^+ dt', \\
\#4 &= 2a \int_{2\frac{H}{c_s^+}}^{t} \frac{J_1\left(\sqrt{(qc_s^+ t)^2 - 4a^2}\right)}{\sqrt{(qc_s^+ t)^2 - 4a^2}} T(t - t') q c_s^+ dt',
\end{aligned}
$$

that appear in the expression of F^+ and G^+ in (2.15) and (2.16). For a constant

η, these terms can be expressed as

$$\begin{array}{lll} \#1 = & -\frac{\mu^+}{H} & a^2 U\left(\frac{H}{c_s^+}(z-2)\right), \\ \#2 = & \frac{\mu^+}{H} & a\int_2^z \frac{J_1\left(a\sqrt{z'^2-4}\right)}{\sqrt{z'^2-4}} U\left(\frac{H}{c_s^+}(z-z')\right)dz', \\ \#3 = & \frac{\mu^+}{H} & 4a^2\int_2^z \frac{J_2\left(a\sqrt{z'^2-4}\right)}{z'^2-4} U\left(\frac{H}{c_s^+}(z-z')\right)dz', \\ \#4 = & & 2a\int_2^z \frac{J_1\left(a\sqrt{z'^2-4}\right)}{\sqrt{z'^2-4}} T\left(\frac{H}{c_s^+}(z-z')\right)dz', \end{array} \tag{4.1}$$

where $z = \frac{t}{\eta\Delta t} = \frac{c_s^+ t}{H}$. It can be shown (see Appendices B.1 and B.2) that for large values of a, the asymptotic behavior of these terms is

$$\begin{array}{llll} \#1 = & -\frac{\mu^+}{H} & a^2 & U\left(t-2\frac{H}{c_s^+}\right) \\ \#2 \simeq & \frac{\mu^+}{H} & & U\left(t-2\frac{H}{c_s^+}\right) \\ \#3 \simeq & \frac{\mu^+}{H} & a^2 & U\left(t-2\frac{H}{c_s^+}\right) \\ \#4 \simeq & & & T\left(t-2\frac{H}{c_s^+}\right), \end{array} \tag{4.2}$$

It seems thus that the instabilities are mainly caused by the terms #1 and #3. Furthermore, when $a \to \infty$, the terms #1 and #3 tend to cancel each other (see Appendix B.1), but their absolute values tend to infinity. So, when a increases, we have to perform a difference between two large numbers that are close to each other, which can lead to large numerical errors. Note that this convergence has to be considered very carefully since it implicitly assumes that U does not vary as quickly as the convolution kernels.

4.2 Low-pass filter

Since the global problems are unstable due to the high frequencies, we choose to damp these using a low-pass filter. In order to chose a convenient filter, let us consider the worst possible distribution of frequencies, i.e., the slowest decreasing rate of the importance of the modes in the Fourier series, and find a filter that would keep the stability for this distribution.

Since Dirac δ-functions are unlikely to appear in the displacement distribution, the worst distribution would correspond to a spatial discontinuity and could be represented here by

$$u(x,t) = \sum_j e^{iq_j x}\frac{k(t)}{q_j} = \sum_j e^{\pm i a_j x/H}\frac{\check{k}(t)}{a_j}.$$

The importance of terms #1 and #3 in (4.1) would in this case be proportional to $a/H = q$. In order to prevent the increase of this importance for high frequencies, we decide thus to apply a filter of the first-order to the function l^+

defined in (2.14). So, instead of using $l^+(x,t) = \mathscr{F}^{-1}(L^+(t;q))$ in (2.18), we use $\tilde{l}^+(x,t) = \mathscr{F}^{-1}\left(\tilde{L}^+(t;q)\right)$, where

$$\tilde{L}^+(t;q) = L^+(t;q)\frac{1}{1+\frac{q}{q_c}} = L^+(t;q)\frac{1}{1+\frac{a}{a_c}}. \tag{4.3}$$

The critical frequency q_c has to be chosen empirically and is the result of a trade-off between the stability and the accuracy of the simulation. Since there is no theoretical way to evaluate the accuracy, we compare the solutions obtained with different critical values with those obtained without filter before the beginning of the instabilities. Note that we do not discuss in this section some very interesting phenomena involving wave propagations and reflections appearing in the results of these tests as this discussion is the purpose of Chapters 6 and 7 for more realistic material systems. The emphasis of the test problems described hereafter is placed solely on assessing the accuracy and stability of the spectral scheme described in Chapter 2.

4.2.1 First test: crack propagation and arrest

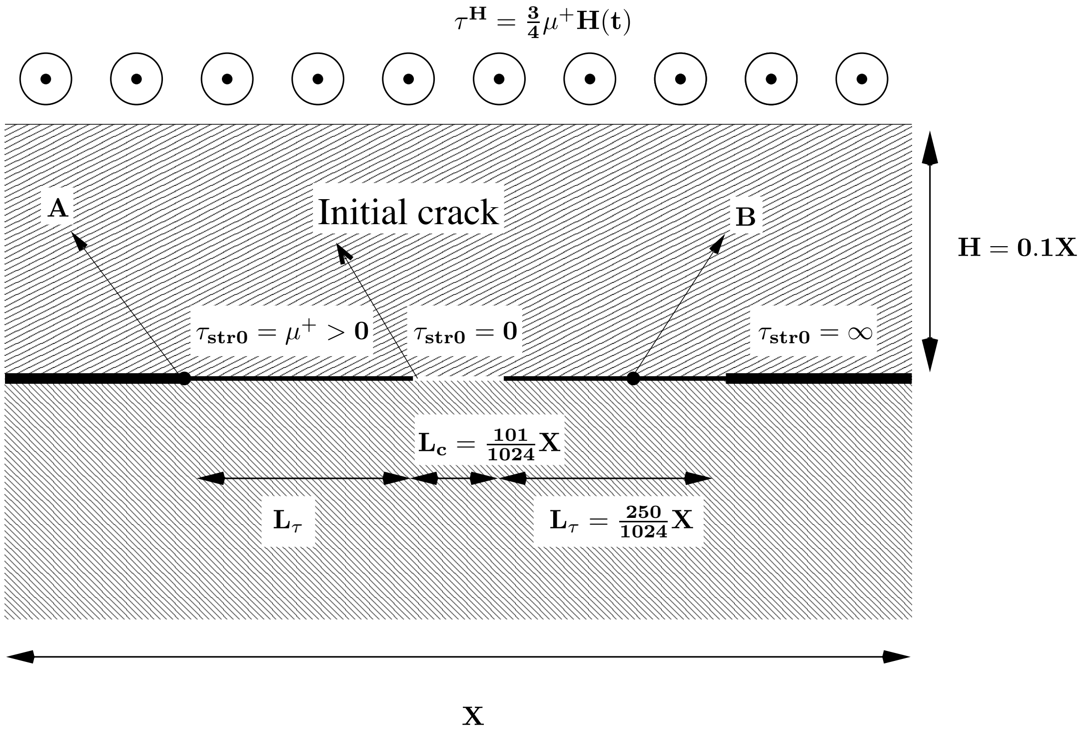

Figure 4.1: First test problem.

For this first stability and precision test, we study the problem of a crack that is allowed to propagate up to a certain point and is then arrested (Figure 4.1). The characteristics of the material are $\mu^+ = \mu^-$, $c_s^+ = 2c_s^-$. The thickness of the thin film is $H = 0.1X$. Since we use 1024 dicretization points and $\beta = 0.05$, where β is defined in (2.19), we have $\eta = 2048$ and $a \in [0, 102.4\pi \simeq 321.7]$ with a non-dimensional frequency discretization step $a_0 = 0.2\pi \simeq 0.63$. The applied stress is $0.75\mu^+$. The initial crack ($\tau_{str0} = 0$) has a length of $L_c = 101\Delta x$ and is located between two zones of initial strength $\tau_{str_0} = \mu^+$, critical distance $\delta_c = 0.05X$, and of length $251\Delta x$, as shown in Figure 4.1. The other points have a virtually infinite initial strength, which prevents the crack from propagating, i.e., arrests it.

In our tests, we considered a point located at the arrested crack tip (point A in Figure 4.1), where the stress takes large values, and a point located in the zone were the crack is allowed to propagate (point B in Figure 4.1). The tested critical frequencies a_c/a_0 entering the first-order low-pass filter in (4.3) are $160, 320$ and 480, which correspond respectively to $a_c \simeq 100, 200$ and 300 since we use $X = 1$.

As we can see in Figures 4.2 and 4.3, the filter removes all the instabilities on the interface displacements u^+ and u^- while affecting the displacement values very little.

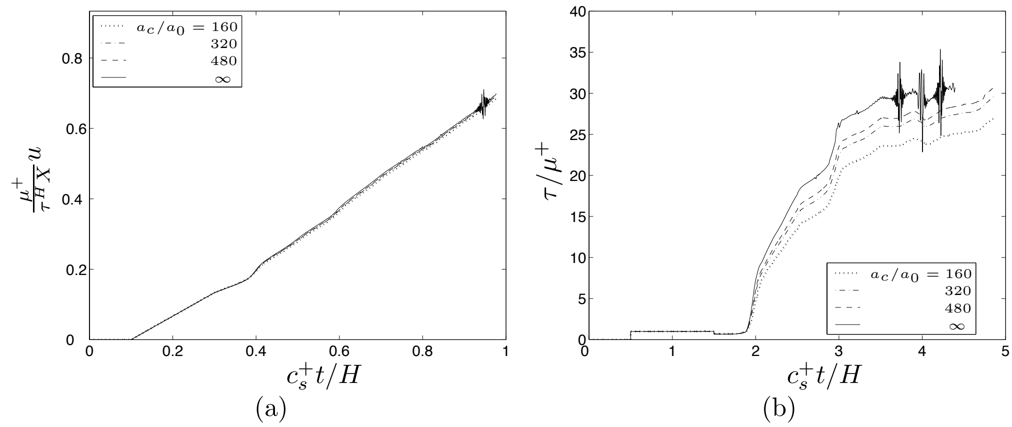

Figure 4.2: Effect of the critical non-dimensional frequency a_c on the evolution of the displacement u (a) and traction stress τ (b) at a point A, located at the arrested crack tip for the first test problem described in Figure 4.1. The results show how the low-pass filtering eliminates the instabilities present in the unfiltered solution ($a = \infty$).

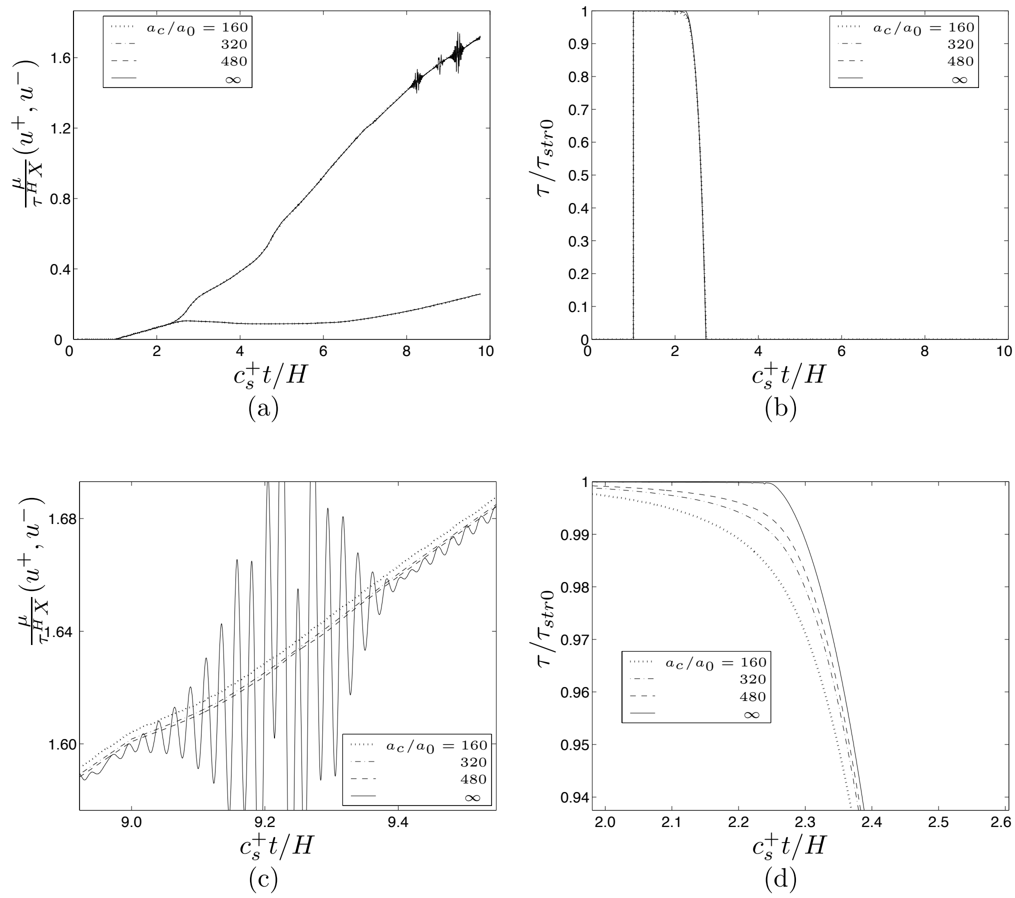

Figure 4.3: Effect of the critical non-dimensional frequency a_c on the evolution of the displacement u^+, u^- (a) and traction τ (b) at point B on the path of propagating crack in the first test problem described in Figure 4.1. Figures (c) and (d) present zoomed-in features. The results show how the low-pass filtering eliminates the spurious oscillations present in the unfiltered solution ($a_c = \infty$) without affecting the displacement and traction evolution.

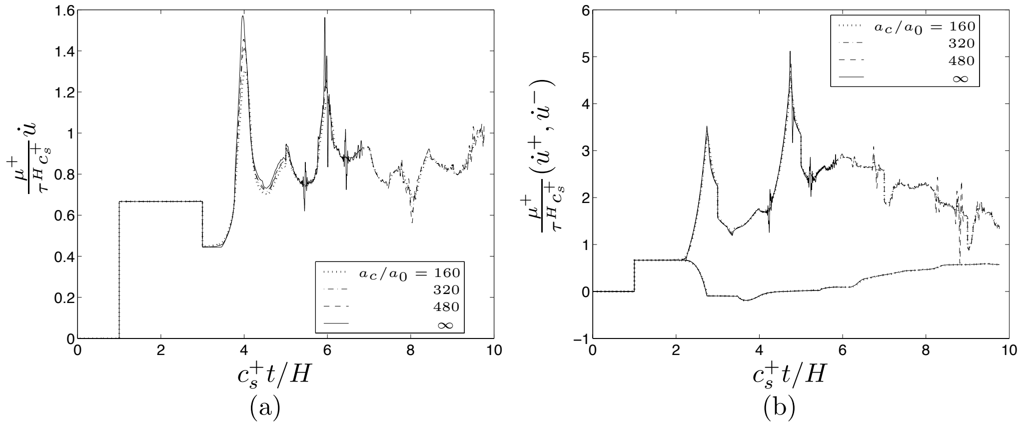

Figure 4.4: Effect of the critical non-dimensional frequency a_c on the evolution of the velocity at point A located at the final crack tip (a), and at point B on the path of propagating crack (b), for the first test problem described Figure 4.1. Figures (4.5a),(4.5c) and (4.5b),(4.5d) present zoomed-in features of respectively (a) and (b). These plots show how the low-pass filtering eliminates the spurious oscillations present in the unfiltered solution ($a_c = \infty$) without affecting the velocity evolution.

The filter also removes the visible instabilities on the stress, even if some very small oscillations can still be seen for $a_c/a_0 = 480$. But, if the stress at B is not influenced very much by the filter except at the beginning of the transition, the stress error at A is relatively large. This is because the stress at this point takes very large values (theoretically there is a singularity) which are the results of constructive interferences of the high frequencies.

The error on the velocity caused by the filter is relatively small except when there are some large accelerations or sharp transitions (see Figures 4.4 and 4.5). We can also see that for $a_c/a_0 = 320$ and 480, there are still some instabilities after $c_s^+ t/H = 7$. An interesting observation is that the displacement does not seem to be affected by the first instabilities in the velocity. This tends to show that the error they cause is symmetric.

4.2.2 Second test

As a second test, we consider the problem of a non-propagating crack. In this case, if x_c is the crack tip location, it can be shown that the traction stress ahead of the crack is given asymptotically by

$$\lim_{x \to x_c} \tau(x,t) = \frac{K_{III}(t)}{\sqrt{2\pi\,|x - x_c|}}, \tag{4.4}$$

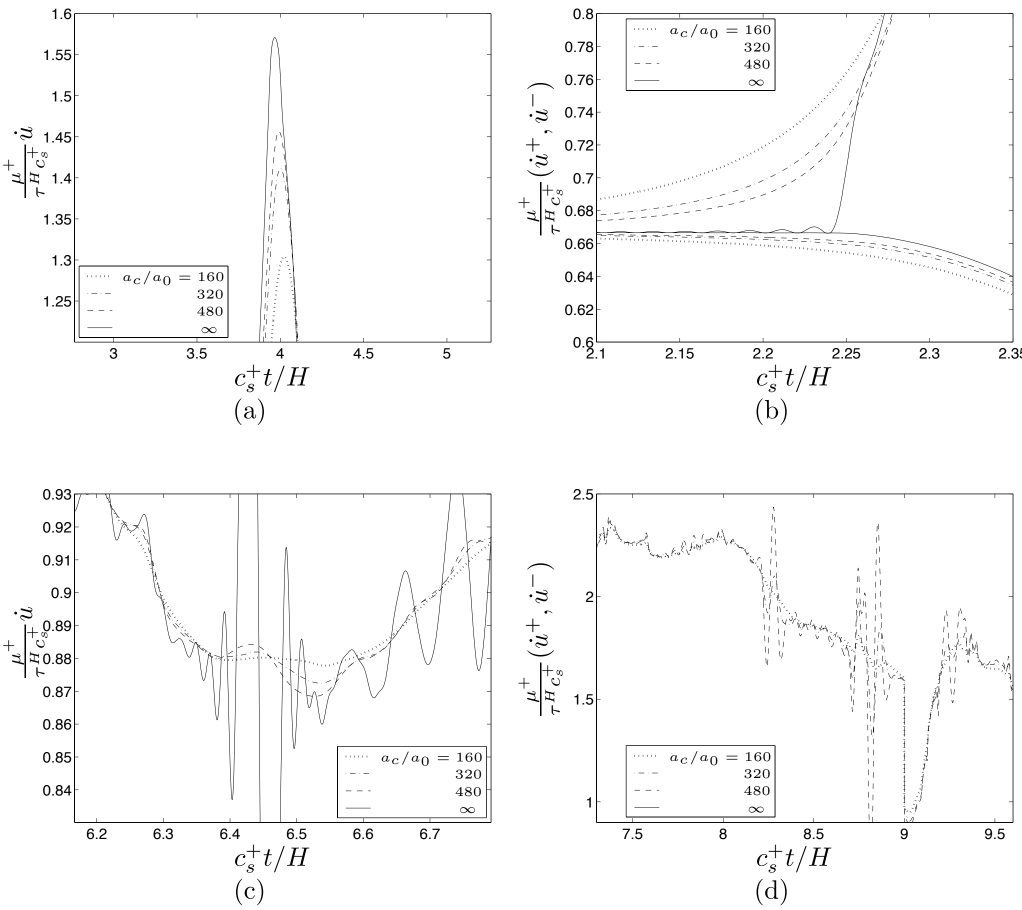

Figure 4.5: Figures (a) and (c) present zoomed-in features of Figure (4.4a), while Figures (b) and (d) present zoomed-in features of Figure (4.4b).

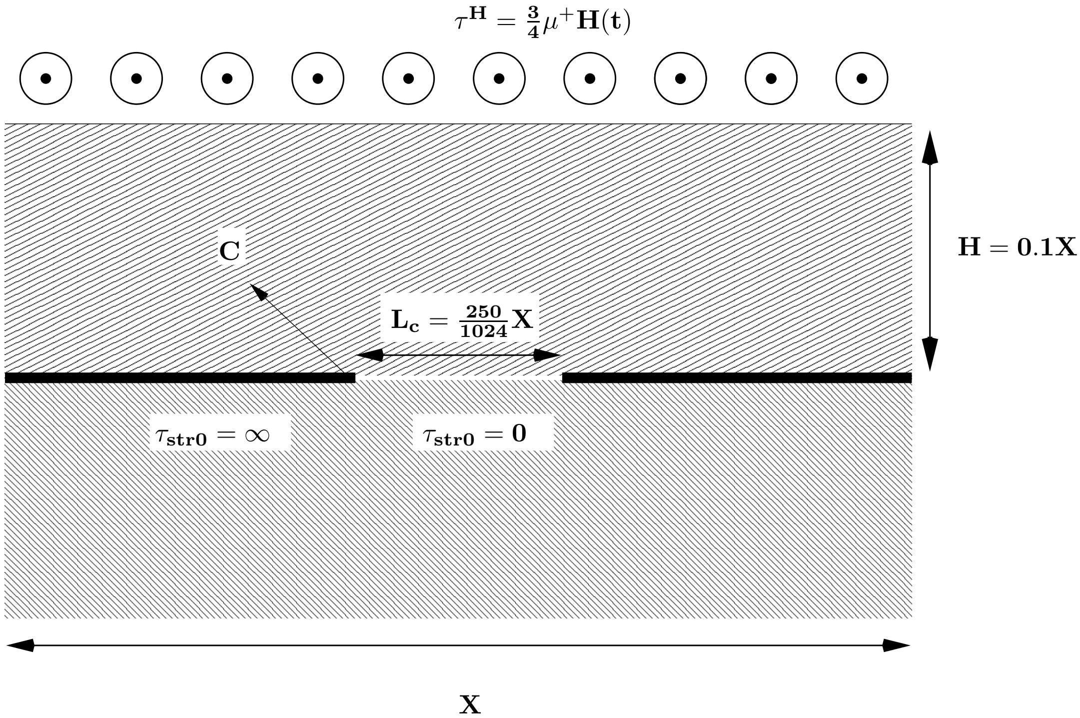

Figure 4.6: Second test problem : non propagating crack.

where $K_{III}(t)$ is the time-dependant stress intensity factor (SIF) that quantifies the intensity of the near-tip singular stress field, and $|x - x_c|$ denotes the distance from x to the crack tip. This constant can also be expressed with respect to the slip inside the crack,

$$K_{III}(t) = \lim_{x \to x_c} \sqrt{\frac{\pi}{2\,|x - x_c|}} \left(\frac{1}{\mu^+} + \frac{1}{\mu^-}\right)^{-1} \left(u^+(x,t) - u^-(x,t)\right). \tag{4.5}$$

In this section, we test the effect of the filter on the evolution of the SIF that we compute using (4.5). For this test, we use the same parameters as in the first test, except that $L_c = 250\Delta x$, and that outside of the crack, the strength is virtually infinite, as shown in Figure 4.6.

As we can see in Figure 4.7, the error caused by the filter is not to be neglected, especially when $a_c/a_0 = 160$. This is mainly due to the fact that, in the neighborhood of the crack tip, many high frequencies are involved. Moreover, even if the biggest part of the instabilities is removed, some small oscillations are still visible when $a_c/a_0 = 480$.

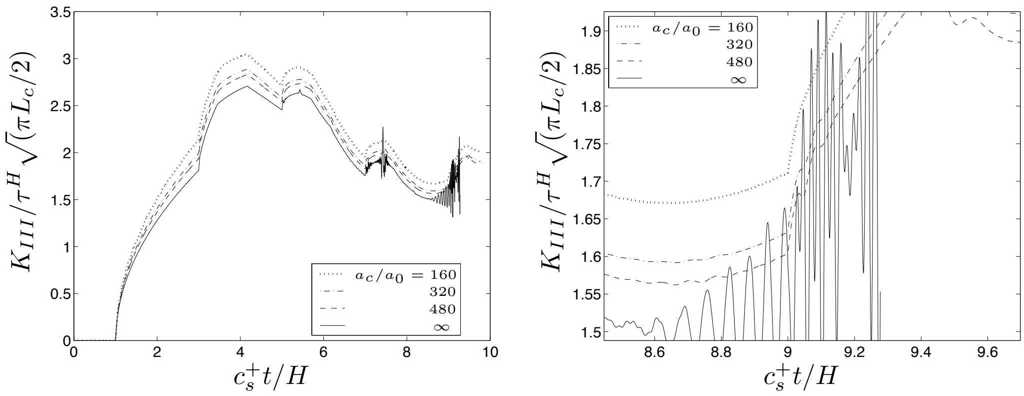

(a) (b)

Figure 4.7: (a) Effect of the critical non-dimensional frequency a_c on the evolution of the stress intensity factor $K_{III}(t)$ defined in (4.5) for the second test problem described in Figure 4.6. Figure (b) presents zoomed-in features.

4.3 Conclusion

The results of these tests show us that applying a low-pass filter on the function $l^+(x,t)$ remove efficiently the spurious oscillations and does in the majority of the cases not affect the rest of the solution, as shown in Figure 4.8. However, if chosen to small, the critical frequency can lead to non negligible errors in some particular situations involving many high frequencies (see Figure 4.7).

Due to the number of different intervening parameters, it is hard to determine, given a physical problem, the optimal critical frequency. However, based on the previous tests and several similar ones, it seems that the value $q_c = 1250/X$ gives usually good results, since it is the highest value that removes all oscillations. We therefore use this value in the following chapters. Note that with, this value of q_c, the numerical simulation is usually stable for $\beta < 0.35$, but, to be more accurate, we prefer to use values close to 0.05.

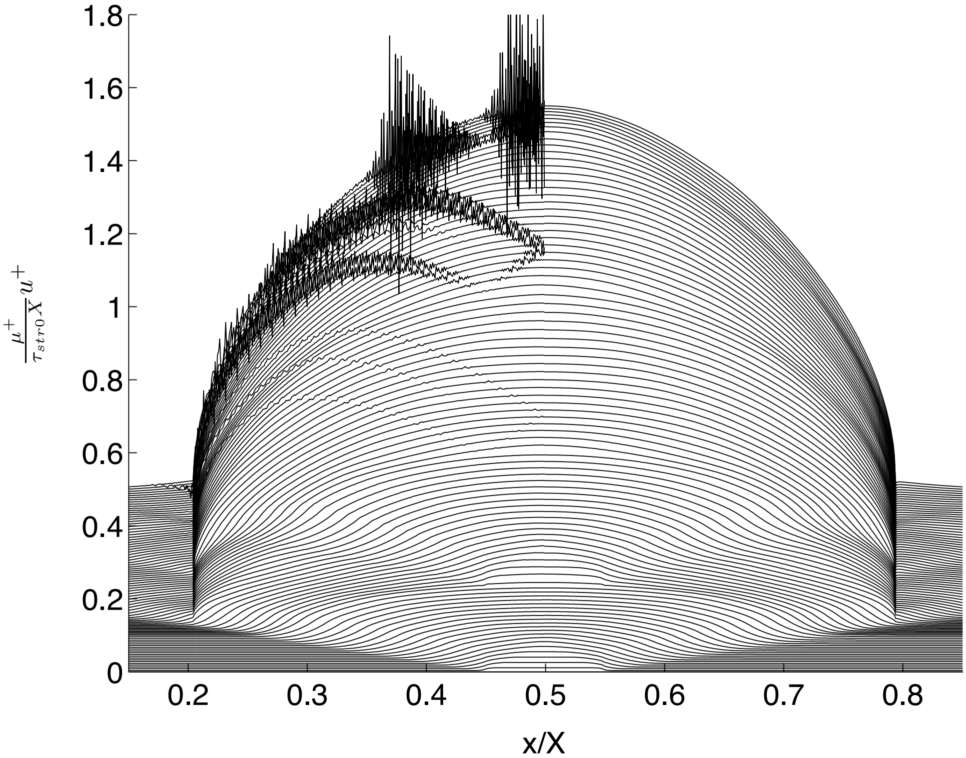

Figure 4.8: Evolution of the displacement of the upper part of the interface u^+ for the first test problem described in Figure 4.1. Left ($0 \leq x \leq X/2$): no filter; Right ($X/2 < x \leq X$): $q_c = 1250/X$. This plot shows that the filter removes all the spurious oscillations without affecting the rest of the solution.

Chapter 5

Motion of thin film surface

In the laser-induced spallation experiments described in Chapter 1, interferometric measurements of the velocity history are made at discrete locations along the thin film surface. It is therefore useful to extend the spectral formulation to compute the displacement an velocity histories along $y = H$.

Let us remember from (2.3) that

$$\hat{\Omega}(y; p, q) = \hat{A}(p, q)e^{|q|\alpha_s y} + \hat{B}(p, q)e^{-|q|\alpha_s y},$$

where $\Omega = \mathscr{L}\left(\mathscr{F}(u_z)\right)$. So, if

$$u^H(x, t) = u_z\left(x, y = H, t\right),$$

and $\hat{U}^H = \mathscr{L}\left(\mathscr{F}(u^H)\right)$, we have

$$\hat{U}^H(p, q) = \hat{A}(p, q)e^{|q|\alpha_s^+ H} + \hat{B}(p, q)e^{-|q|\alpha_s^+ H}.$$

Using (2.9) and the first line of (2.4) to eliminate $\hat{A}$ and $\hat{B}$ in this last relation, we get

$$\hat{U}^H\,|q|\,\alpha_s^+\left(1 + e^{-2a\alpha_s^+}\right) = 2\,|q|\,\alpha_s^+\hat{U}e^{-a\alpha_s^+} + \frac{1}{\mu^+}\hat{T}^H\left(1 - e^{-2a\alpha_s^+}\right). \qquad (5.1)$$

Back in the time and space domains, we obtain (see Appendix A.6)

$$\begin{aligned}\tfrac{1}{c_s^+}\dot{u}^H(x,t) = \quad & \tfrac{2}{c_s^+}\dot{u}\left(x, t - \tfrac{H}{c_s^+}\right) + f^H(x,t) \\ + \quad & \tfrac{1}{\mu^+}\tau^H(x,t) - \tfrac{1}{\mu^+}\tau^H\left(x, t - \tfrac{2H}{c_s^+}\right) + h^H(x,t) \\ - \quad & \tfrac{1}{c_s^+}\dot{u}^H\left(x, t - \tfrac{2H}{c_s^+}\right) - g^H(x,t) \\ = l^H(x,t) & \end{aligned}$$

where the convolution terms are expressed in the Fourier domain as

$$\begin{aligned}
F^H &= \mathscr{F}(f^H) = -|q|\,aU\left(t-\tfrac{H}{c_s^+}\right) &&+2|q| \int_{\frac{H}{c_s^+}}^{t} C'_{H3}(|q|\,c_s^+t')U(t-t')\,|q|\,c_s^+dt' \\
H^H &= \mathscr{F}(h^H) = &&\tfrac{1}{\mu^+} \int_{\frac{2H}{c_s^+}}^{t} D_3(|q|\,c_s^+t')T^H(t-t')\,|q|\,c_s^+dt' \\
G^H &= \mathscr{F}(g^H) = -|q|\,aU^H\left(t-\tfrac{2H}{c_s^+}\right) &&+|q| \int_0^t \left(C_\infty(|q|\,c_s^+t')+C_{H3}(|q|\,c_s^+t')\right)U^H(t-t')\,|q|\,c_s dt'.
\end{aligned}$$

The convolution kernels $D_3(T), C_{H3}(T), C_\infty(T)$ have been defined in (2.7) and (2.16), and

$$C'_{H3}(T) = \left(\frac{J_1\left(\sqrt{T^2-a^2}\right)}{\sqrt{T^2-a^2}} + a^2\frac{J_2\left(\sqrt{T^2-a^2}\right)}{T^2-a^2}\right)H(T-2a).$$

As in Section 3.1, an analytical solution can be found in the case of a perfect interface for a single mode loading $\tau_0^H e^{iqx}H(t)$, and when $c_s^+ = c_s^- = c_s$. In this case, (5.1) becomes

$$p\hat{U}^H\cosh(a\alpha_s) = p\hat{U} + \frac{\tau_0^H}{\mu^+ q\alpha_s}\sinh(a\alpha_s).$$

Reintroducing the analytical expression of $p\hat{U}$ from (3.1) in this equation, and performing an inverse Laplace transform as described in Appendix A.7 yields

$$\dot{U}^H(i\Delta t) = \frac{\tau_0^H c_s}{\mu^+}\left(J_0\left(a\frac{i}{\eta}\right) + 2\sum_{n=1}^{\infty}(\Delta_\mu)^n J_0\left(a\sqrt{\left(\frac{i}{\eta}\right)^2 - 4n^2}\right)H\left(\frac{i}{\eta}-2n\right)\right).$$

Note that in the case $a = 0$, both $\dot{U}$ and $\dot{U}^H$ converge to the same limit velocity

$$\dot{U}_\infty = \frac{\tau_0^H c_s}{\mu^-}, \tag{5.2}$$

which does not depend on any characteristic of the thin film.

Using this analytical solution, we can perform an error analysis similar to what is done Chapter 3. As it is expected, the numerical behavior of this scheme is similar to that of the scheme derived in Chapter 2 to compute the displacement and the traction stress at the interface. It is therefore needed to apply on $l^H(x,t)$ the same filter as on $l^+(x,t)$, as described in Chapter 4.

Chapter 6

Non propagating crack

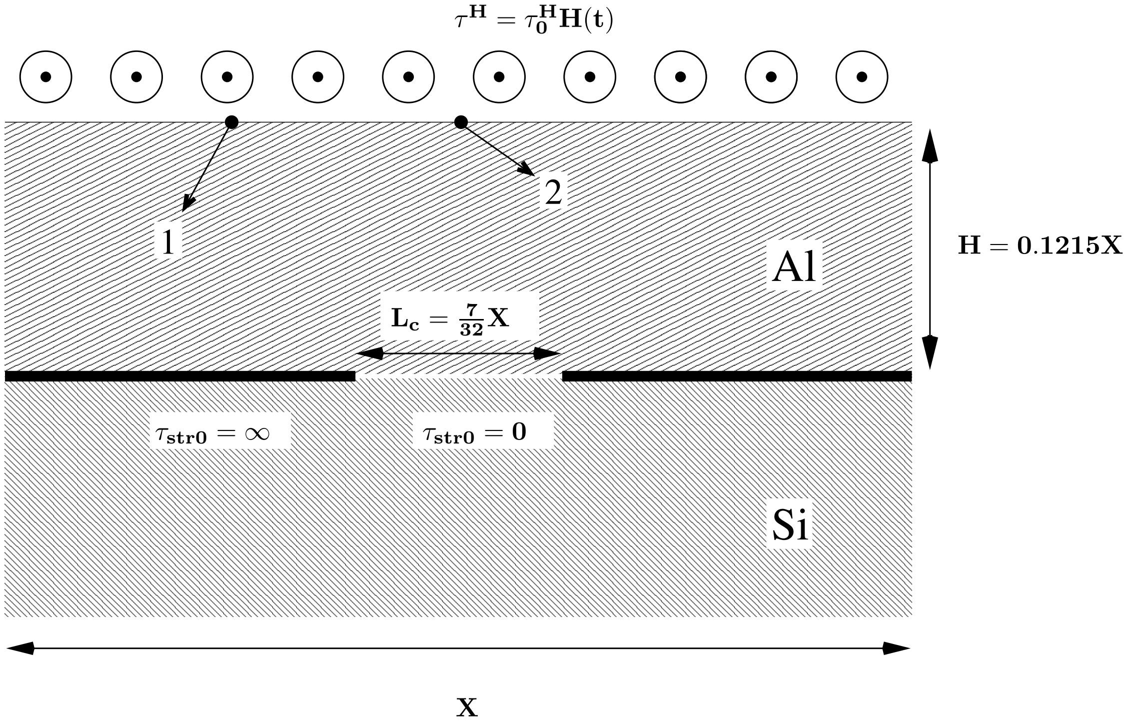

Figure 6.1: Description of the non-propagating crack problem. Node 2 is located above the center of the crack while node 1 is at $1.125L_c$ from node 2. Typical values :$H = 100\mu m$, $L_c = 180\mu m$, $X = 823\mu m$ and $H/c_s^+ = 32.28ns$.

In this chapter, we analyze the behavior of a non-propagating crack located between a substrate made of fused silica and an aluminium thin film (see Figure

6.1) as in the experiments described in [12]. In order to keep the formulations derived in Chapters 2 and 5 valid, we assume the deformations to be small, and both material to be homogeneous and linearly elastic. The properties of the two materials are listed Table 6.1. For these materials, we consider the behavior of the interface, and the evolution of the stress intensity factor, for the case $L_c = 1.8H$ (Figure 6.1). We also look at the evolution of the velocity and the displacement of two points located at the surface of the thin film. One is just above the center of the crack, while the other is outside the crack zone, at a distance $1.125L_c$ from the first one. The discretization parameters of the solved problem are $L_c/X = 7/32$, $\eta = H/c_s^+ \Delta t = 2048$ $\Delta x = X/1024$, and thus $\beta = 0.07$, which satisfies the Courant condition ($\beta < 1$).

Material	μ (GPa)	ρ (kg/m^3)	c_s (m/s)
Fused Silica	30.8	2200	3741.7
Aluminium	26.0	2710	3097.4

Table 6.1: Material properties [12].

As shown in Figure 6.2, our spectral scheme is able to capture the stress concentration at the crack tips. Figures 6.3 and 6.4 show the evolution of the displacement along the interface. One can observe that each reflection of the initial plane wave correspond to an increase of the velocity, followed by a deceleration until the next wave reflection. However, this is mainly visible in the crack zone and for the thin film; this effect can thus also be seen on the slip at the interface, as shown in Figure 6.5. One can also observe Figures 6.6 and 6.7 the influence of the crack on the surface displacement u^H beginning at $t = 2H/c_s^+$. This time is indeed needed by a wave to cross the film, to be reflected off the crack, and to propagates to the film surface. Note that the zone of the surface influenced by the crack grows with time, but that the difference of displacement between the nodes located above the crack ($x \geq 25/64X$) and the other nodes ($x < 25/64X$) diminish with time, even if a sharp acceleration takes place above the crack at each reflection of the initial wave at $t = 2H/c_s^+$. In the zone far from the crack, we can also see Figure 6.7 the very small influence of the wave resulting from the reflection of the initial plane wave off the interface reaching the film surface at $t = 2H/c_s^+$. The reasons of the small amplitude of this wave are discussed Section 7.1. Figure 6.8 shows the evolution of the displacement and the velocity for a point above the center of the crack and a point located outside of the crack. This is the kind of evolution measured by [12]. The behavior of node 1 seems complex, but for node 2 located above the center of the crack, we can see again at each reflection of the initial wave the important discontinuous augmentations of the velocity followed by decelerations.

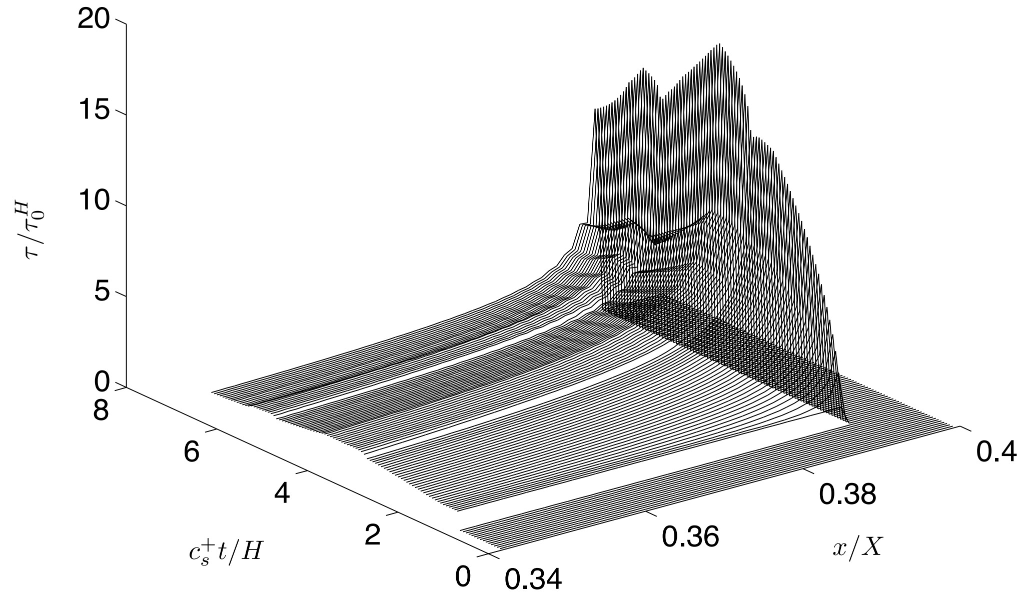

Figure 6.2: Evolution between $t = 0$ and $t \approx 6.5H/c_s^+$ of the stress at the interface, showing a stress concentration next to the crack tip. Note that the evolution of the height of the maximum of the stress is similar to that of the stress intensity factor shown in Figure 6.9.

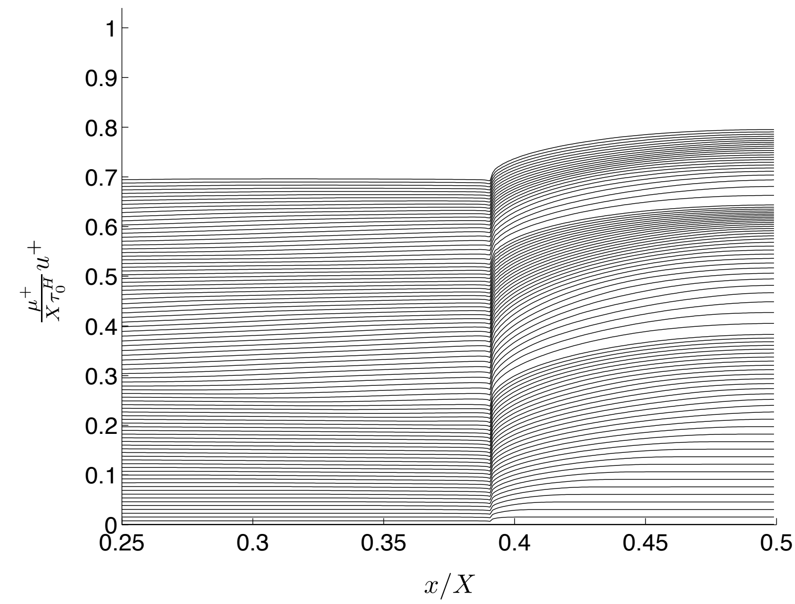

(a)

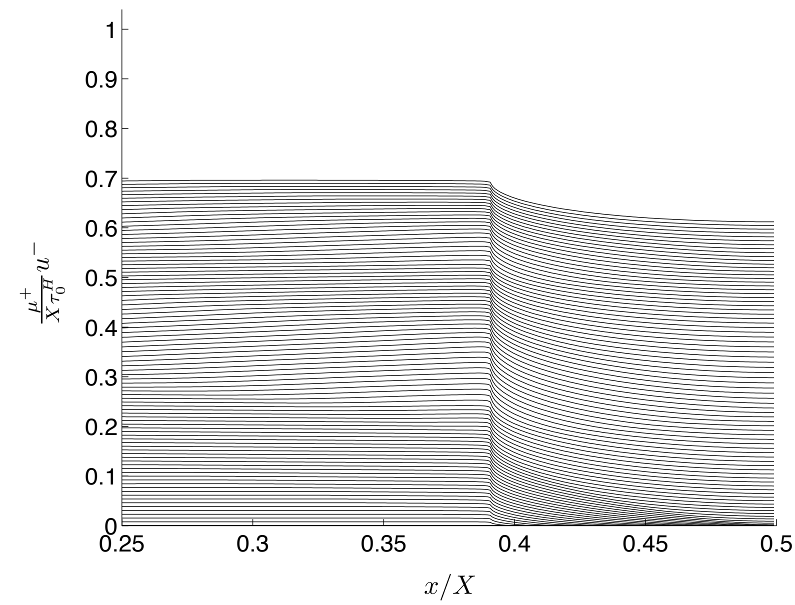

(b)

Figure 6.3: Evolution between $t = 0$ and $t \approx 6.5H/c_s^+$ of the displacements at the interface (time period between the lines: $H/16c_s^+$): (a) thin film interface displacement u^+ showing a variation in the velocity at each reflection of the shear wave, (b) substrate interface displacement u^-.

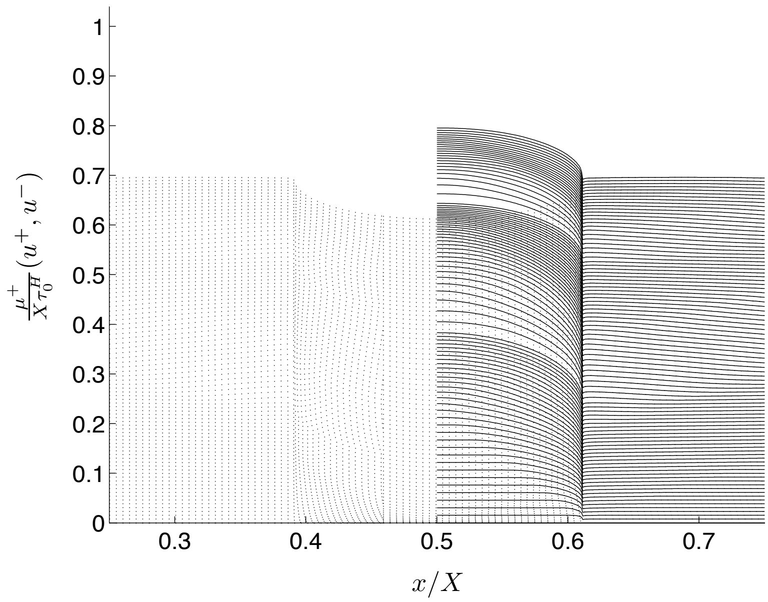

Figure 6.4: Evolution between $t = 0$ and $t \approx 6.5H/c_s^+$ of the displacement at the interface (time period between the lines : $H/16c_s^+$).

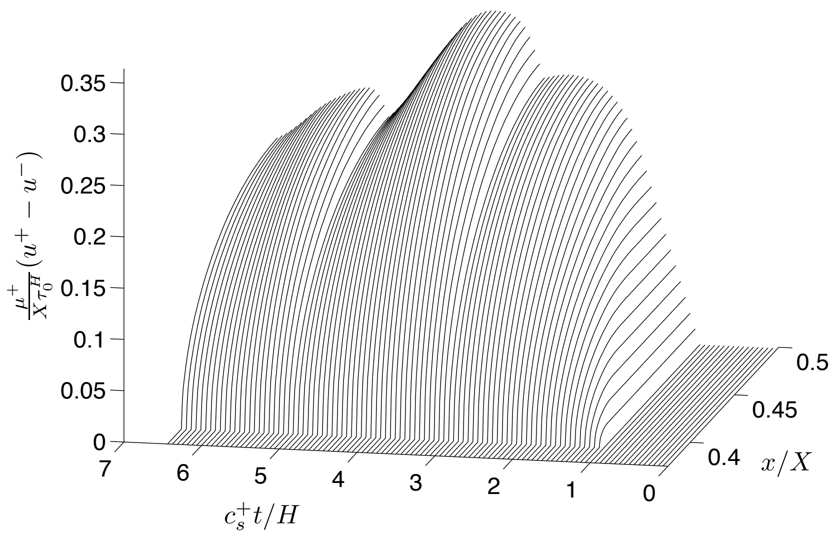

Figure 6.5: Evolution between $t = 0$ and $t \approx 6.5H/c_s^+$ of the slip at the interface, $u^+ - u^-$, showing the effect of the wave reflections at $t = (2n + 1)H/c_s^+$, and the presence of a maximum at $t \approx 4H/c_s^+$.

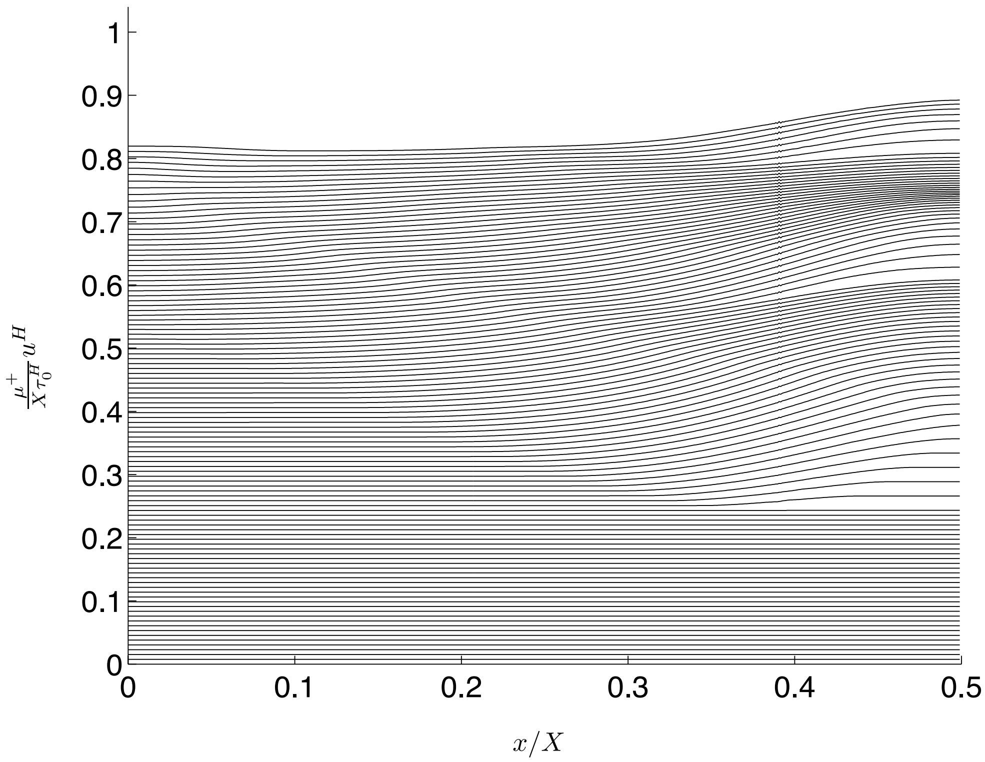

Figure 6.6: Evolution between $t = 0$ and $t \approx 6.5H/c_s^+$ of the displacement at the surface of the thin film (time period between the lines : $H/16c_s^+$).

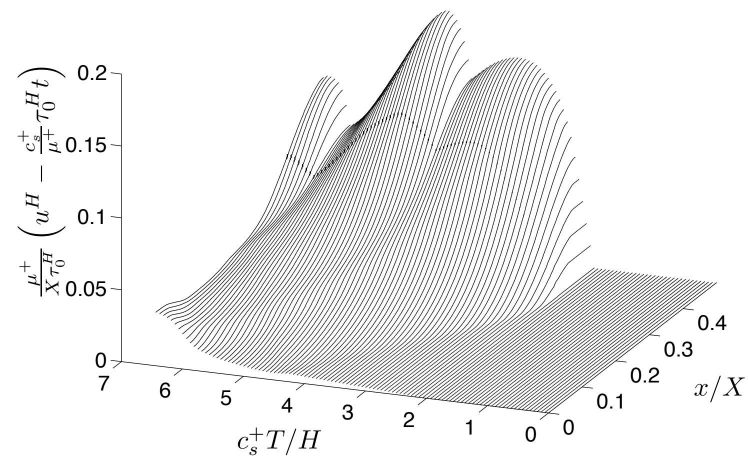

Figure 6.7: Evolution of the difference between the displacement of the surface u^H and the displacement that would be observed if a similar stress was applied along the surface of a semi-infinite aluminium material $\frac{c_s^+}{\mu^+}\tau_0^H t$, showing an acceleration in the zone above the crack at $t = 2nH/c_s^+$. Note that the zone influenced by the crack grows, and that the difference between the displacement of the nodes located above the crack and the other nodes decreases. One can also see in the zone far from the crack the very small influence of the plane wave resulting of the reflection of the initial wave off the interface reaching the surface at $t = 2H/c_s^+$.

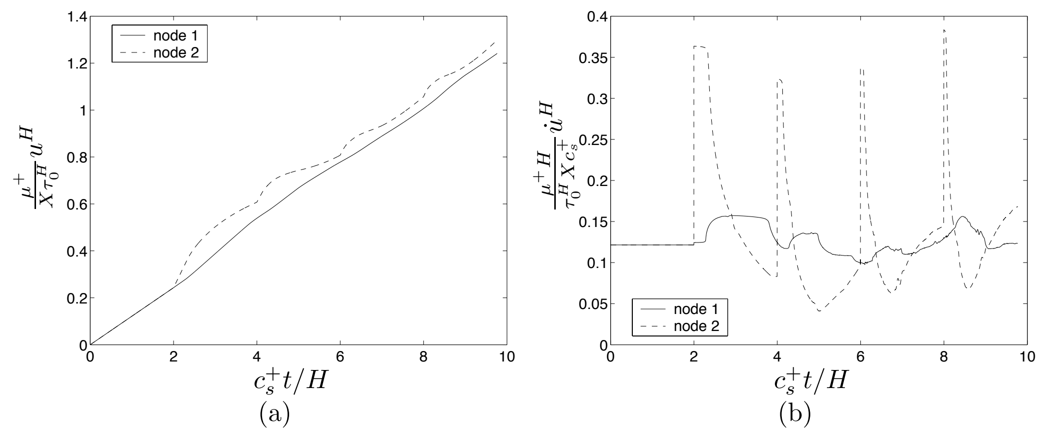

Figure 6.8: Evolution of the displacement (a) and the velocity (b) at two locations along the surface of the thin film (see Figure 6.1). This plot shows the influence of each reflection on the velocity for node 2, while the behavior of node 1 is more chaotic.

We now turn our attention to the evolution of the time-dependant stress intensity factor $K_{III}(t)$ characterizing the near-tip singularity and defined by (4.4) and (4.5).

As it can be observed in Figure 6.9, there are various angular points in the evolution of the stress intensity factor. These points correspond to the reflections of waves off the crack tips. To each angular point (except the first one which correspond to the initial plane wave reaching the interface) corresponds thus a path between one crack tip and either itself or the other crack tip. These different paths are represented in Figure 6.10 and described hereafter.

- Path O corresponds to the initial plane wave propagating from the external boundary of the thin film to the interface and thus to the crack tips. The time t_o needed by a wave to follow this path is

$$\frac{c_s^+}{H} t_o = 1.$$

- Path A corresponds to a wave that propagates from one of the crack tips to itself after being reflected off the surface. The time t_a needed by a wave to follow this path is

$$\frac{c_s^+}{H} t_a = 2.$$

- Path B corresponds to a wave propagating along the crack in the thin film from one crack tip to the other one. The time t_b needed by a wave to follow this path is

$$\frac{c_s^+}{H} t_b = \frac{L_c}{H} = 1.8.$$

- Path C corresponds to a wave propagating along the crack in the substrate from one crack tip to the other one. The time t_c needed by a wave to follow this path is

$$\frac{c_s^+}{H} t_b = \frac{c_s^+}{c_s^-} \frac{L_c}{H} \simeq 1.5.$$

- Path D corresponds to a wave that propagates from one of the crack tips to the other one after being reflected off the surface of the film. The time t_d needed by a wave to follow this path can be expressed as

$$\frac{c_s^+}{H} t_d = \frac{\sqrt{4H^2 + L_c^2}}{H} = 2.6907.$$

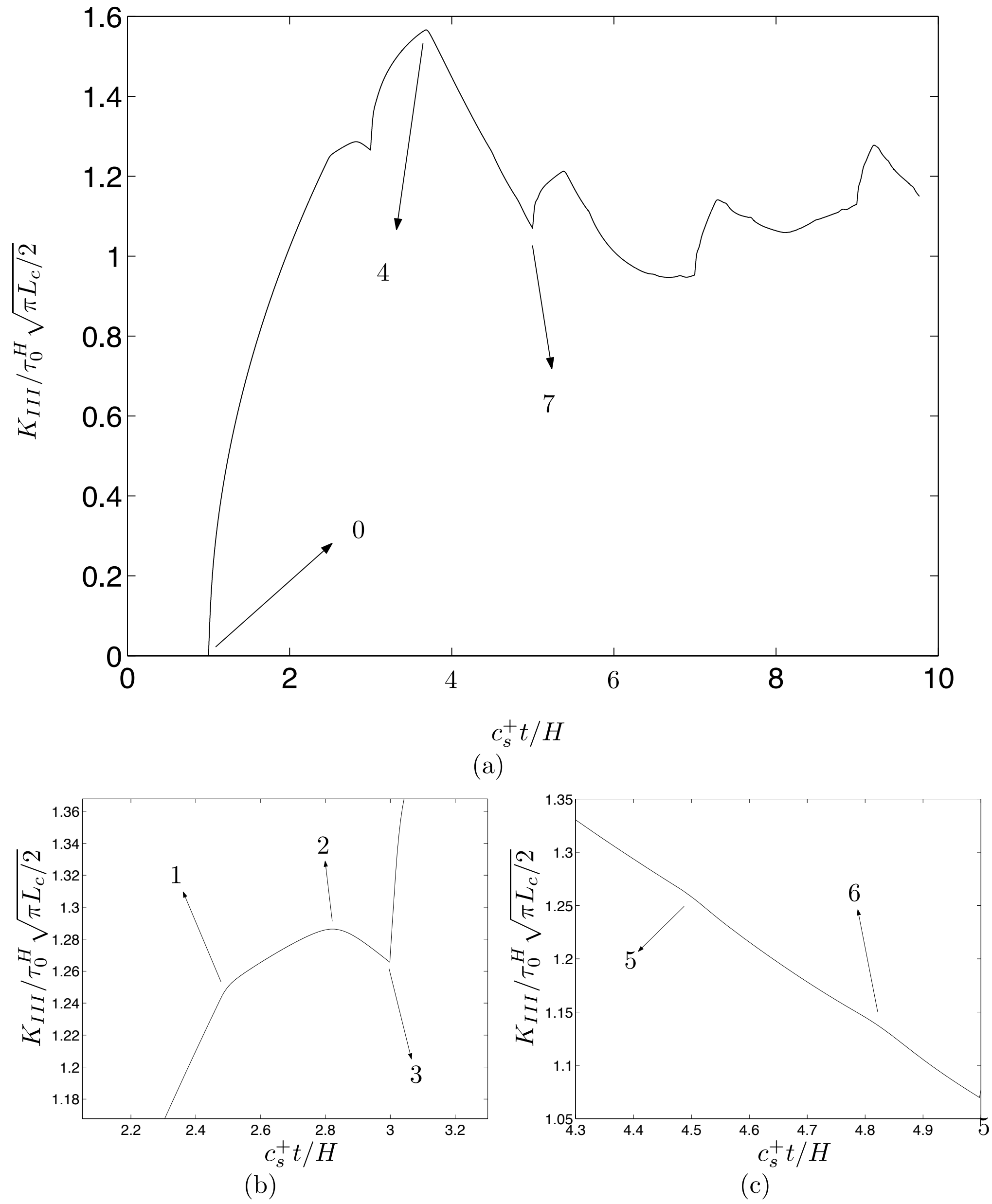

Figure 6.9: Evolution of the stress intensity factor $K_{III}(t)$. Figures (b) and (c) present zoomed-in features of Figure (a), showing different angular points corresponding to wave reflection on the crack tips.

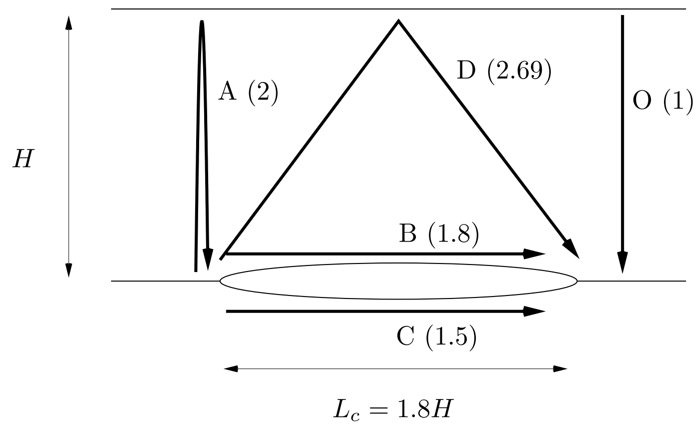

Figure 6.10: Wave trajectories between the crack tips and from the external boundary. The bracketed numbers represent the time (normalized by H/c_s^+) needed for a wave to follow the corresponding path.

point	0	1	2	3	4	5	6	7
time ($c_s^+ t/H$)	1	2.5	2.8	3	3.69	4.5	4.8	5
path	O	OC	OB	OA	OD	OAC	OAD	OAA

Table 6.2: Correspondence table between the angular points appearing in the evolution of $K_{III}(t)$ (Figure 6.9) and the wave propagation paths shown in Figure 6.10.

Comparing the time needed to follow each trajectory to the time at which the different angular points occur, we can deduce the different paths followed by the waves that cause the angular points (see Table 6.2). Note that any permutation of the paths that we propose is also acceptable, as soon as it begins by O. In fact, each angular point is caused by the sum of the contributions of each of these permutations.

Some combinations of path give no visible angular point, for example OBC ($c_s^+ t/H = 4.3$) and OCC ($c_s^+ t/H = 4.6$). This is mainly due to the fact that the amplitude of the waves decreases with every reflection. The corresponding jump in the derivative of the stress intensity factor can then become so small that it cannot be seen.

Chapter 7

Propagating crack

In this chapter, we analyze different cases of propagating interfacial cracks. We begin in Section 7.1 by a problem similar to that studied in Chapter 6, but where the crack is allowed to propagate. In Section 7.3, we consider a system with no loading on the thin film, but with a shear plane wave coming from the substrate, as in the experiments of [12], and see that in that case the crack propagation decelerates until a complete arrest. Finally, we show in Section 7.4 two systems where the mismatch between the materials properties leads to interesting effects involving spallation.

7.1 Dynamic delamination along Al/Si interface with a loading on the film

As indicated before, we consider in this section the dynamic response of a crack located at the interface between a fused silica substrate and an aluminium thin film (see table 6.1 for material properties) as in the experiments of [12]. We look at two different situations: a weak interface where it can be observed that the finite thickness of the film does not influence the propagation, and a stronger interface where the propagation is accelerated due to the waves coming back on the interface after being reflected off the film surface.

Before discussing these two cases, let us consider the dynamic response of the interface in the absence of fracture. The problem is then reduced to a 1-D problem, and one can show using (2.8) and (2.14) that the traction stress and the velocity at the interface are (see Appendix C.1)

$$\tau(t) = \tau_0^H \left(1 - k^{n(t)}\right), \qquad \dot{u}(t) = \tau_0^H \frac{c_s^-}{\mu^-} \left(1 - k^{n(t)}\right), \tag{7.1}$$

where $n(t) = \lfloor \frac{c_s^+ t + H}{2H} \rfloor$ and k denotes the impedance mismatch

$$k = \frac{\frac{\mu^+}{\mu^-} - \frac{c_s^+}{c_s^-}}{\frac{\mu^+}{\mu^-} + \frac{c_s^+}{c_s^-}} = \frac{\frac{\mu^+}{c_s^+} - \frac{\mu^-}{c_s^-}}{\frac{\mu^+}{c_s^+} + \frac{\mu^-}{c_s^-}}. \quad (7.2)$$

Note that the limiting values of the traction stress and the velocity do not depend on the properties of the thin film, which only affect the transitory response.

For the AL/Si system studied here, $k = 0.0098$. So, when the initial shear wave reaches the interface, the traction stress and the velocity take a value close to their limiting value and the further variations are then relatively negligible. Therefore, the plane reflections of the initial shear wave virtually do thus not influence the propagation of the crack. In Section 7.4, we present systems with more interesting value of k.

7.1.1 Weak interface

In this first problem, we apply a shear stress $\tau^H = .8\tau_s H(t)$ along the boundary of the thin film, whose thickness is 1.6 times larger than the initial crack length L_c as shown in Figure 7.1. Outside of the initial crack, the cohesive properties of the interface are $\tau_{str0} = \tau_s$ and $\delta_c = \delta_{c0} = 0.052\frac{\tau_s}{\mu^+}X$. Using $\tau_s = 500MPa$ (from [12]) and the typical length presented in Figure 7.1, this gives $\delta_c \approx 1\mu m$ and $\tau^H = 400MPa$. Since the thin film is mode of aluminium, the time needed for a wave to cross the film is $H/c_s^+ = 32.28ns$. Note that the used discretization parameters are $\Delta x = X/1024, \eta = 2048$ and thus $\beta = 0.06$.

As we can see in Figure 7.2, at $t = 3H/c_s^+$, the plane reflection of the initial wave off the surface and then on the interface causes an acceleration in the zone where the crack was initially located. However this effect does not affect the propagation of the crack, since due to the weak interface, the crack propagates at an intersonic speed as shown in Figure 7.3. No wave propagating in the thin film from the original crack location can thus reach the crack tip and influence the propagation. We can see in Figure 7.5 that the shape of the stress concentration around the crack tip does not vary when the crack propagates, and that in the zones not yet reached by the crack, it takes the value predicted by (7.1). Figure 7.4 shows that after $t = 2H/c_s^+$, the displacement of the film surface is influenced by the interface crack. Since, in this case, the crack propagates, the influence is more important than it was in Figure 6.6. However, there is no visible influence of the other wave reflections off the surface at $t = 2nH/c_s^+$.

Figure 7.6 shows the traction stress rise just before the arrival of the crack for nodes 1 and 2 on the way of the crack (as shown in Figure 7.1). One can also observe the small size of the traction stress variation at $t = 3H/c_s^+$, as predicted by (7.1).

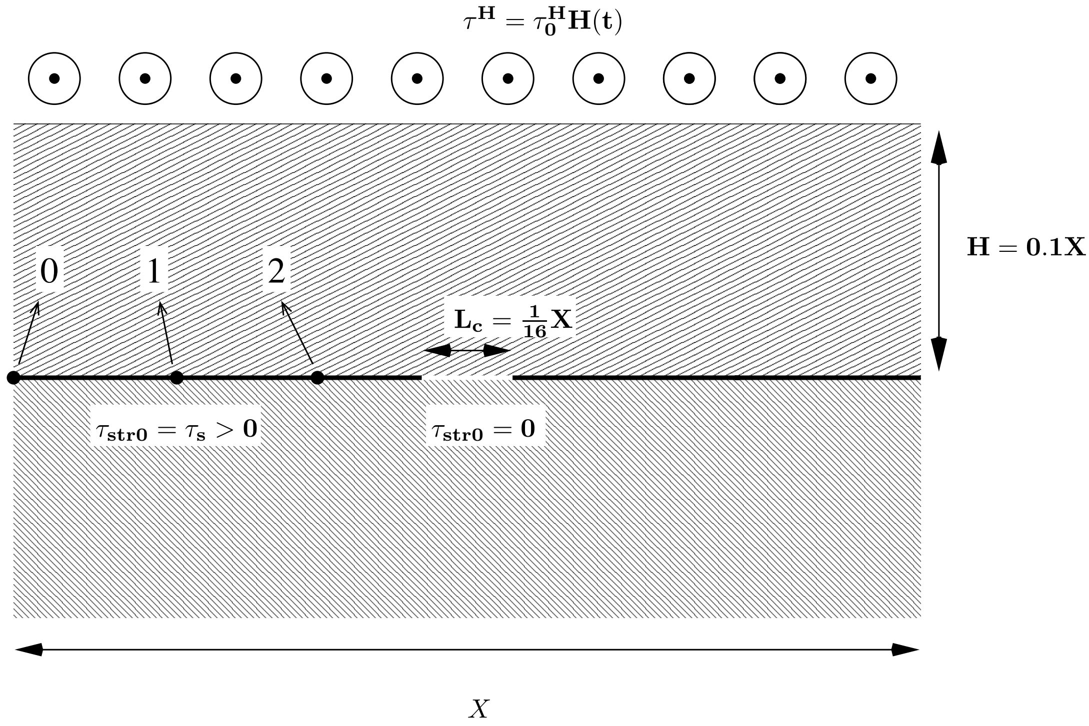

Figure 7.1: Dynamic failure of a weak interface. The nodes locations are $x/X = 0$ for node 0, $x/X = 25/128$ for node 1 and $x/X = 50/128$ for node 2. The distances to the initial crack are thus respectively $7.5L_c$, $4.375L_c$ and $1.25L_c$. Note that typical values are $H = 100\mu m$, $L_c = 62.5\mu m$, $X = 1mm$ and $H/c_s^+ = 32.28ns$.

The evolution of the velocities and displacements at the interface and the surface of the film are shown in Figure 7.7 for a surface point located above node 2. After the large variations following the separation of the two sides of the interface at this point, the velocity of the substrate side seems to keep a quasi-constant value. On the other hand, the velocity of the thin film side of the interface seems then to increase at a constant rate on average, similar to the acceleration of the point located at the surface of the film. This results in a constant acceleration of the slip across the interface, as shown in Figure 7.8. One can also observe that the difference between the displacement at the surface of the film and at the interface is strongly reduced just after the separation of the two sides of the interface.

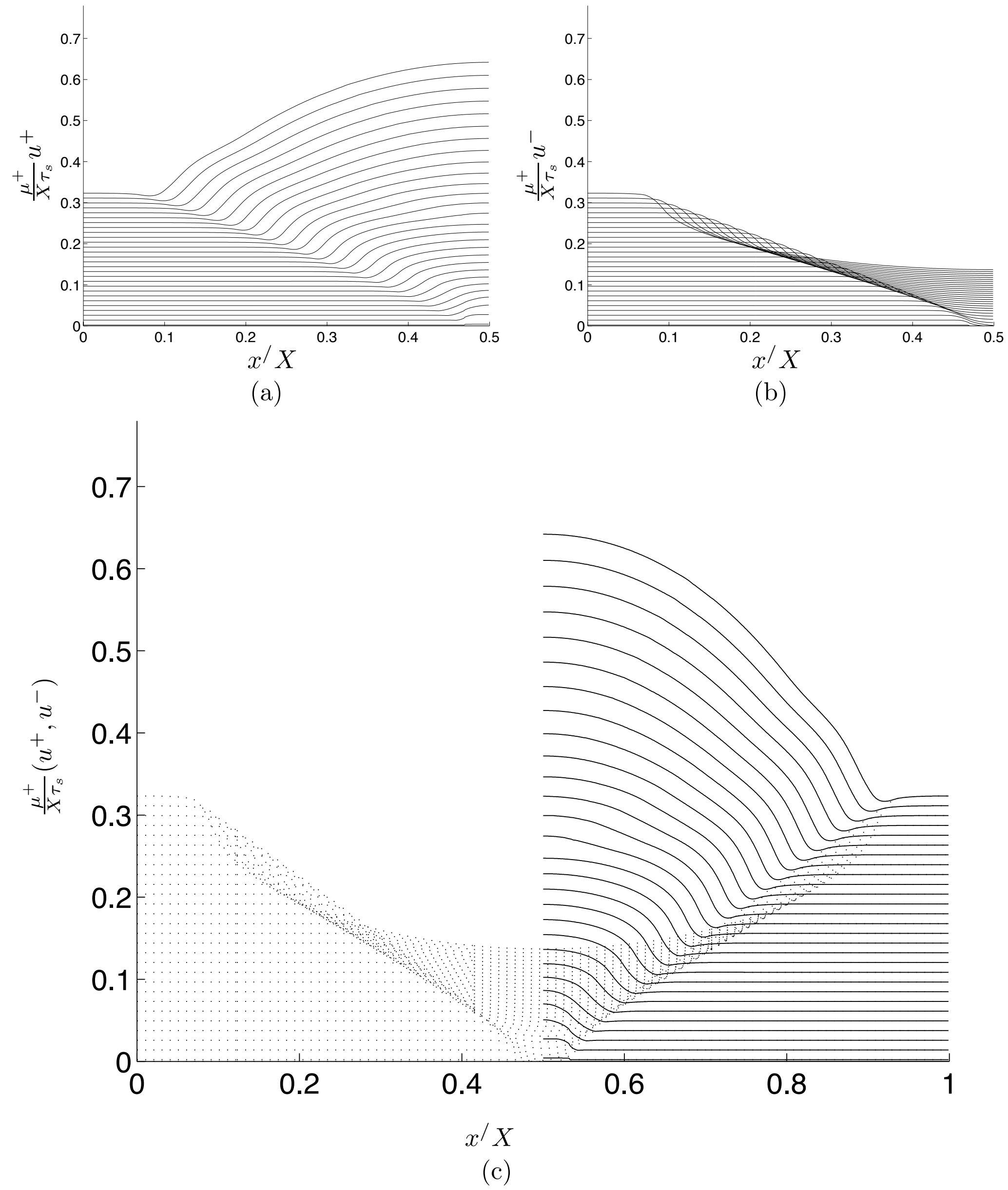

Figure 7.2: Evolution between $t = 0$ and $t \approx 5H/c_s^+$ of the displacement at the interface for the weak interface delamination problem: (a) displacement of thin film at the interface u^+ , (b) displacement of the substrate at the interface u^-, and (c) is a combination of (a) and (b). The time period between the lines is $.1465H/c_s^+$.

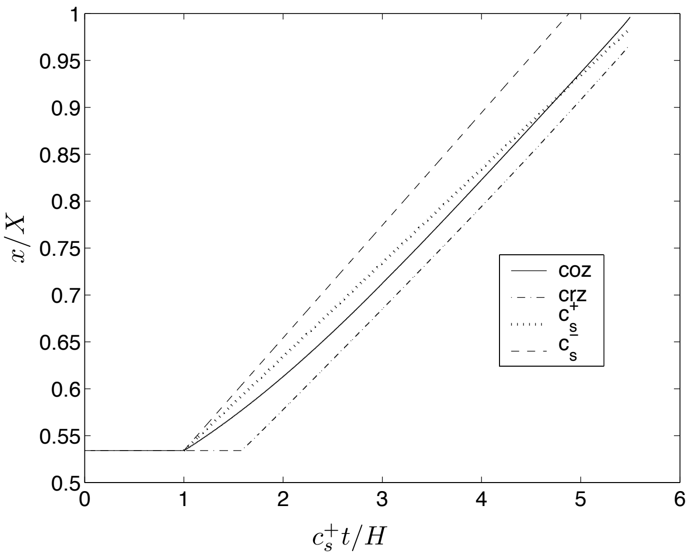

Figure 7.3: Evolution of the tips of the cohesive zone (coz) and the crack tip (crz) for the weak interface delamination problem. c_s^+ and c_s^- denote the propagation of elastic waves in the film and substrate, respectively. Note the intersonic crack motion.

Due to the small value of k in (7.1), the reflection of the initial plane wave does almost not cause any variation of the traction stress. Moreover, due to the large propagation speed, no wave coming from the crack can be reflected off the film surface an then reach the crack tips. From the point of view of the location of the crack, there is thus no difference between the fracture event presented in this section and a similar one that would take place between two semi-infinite media as in [14]. However, the behavior of the part of the thin film located between the crack tips is strongly influenced by the different waves reflected off the film surface.

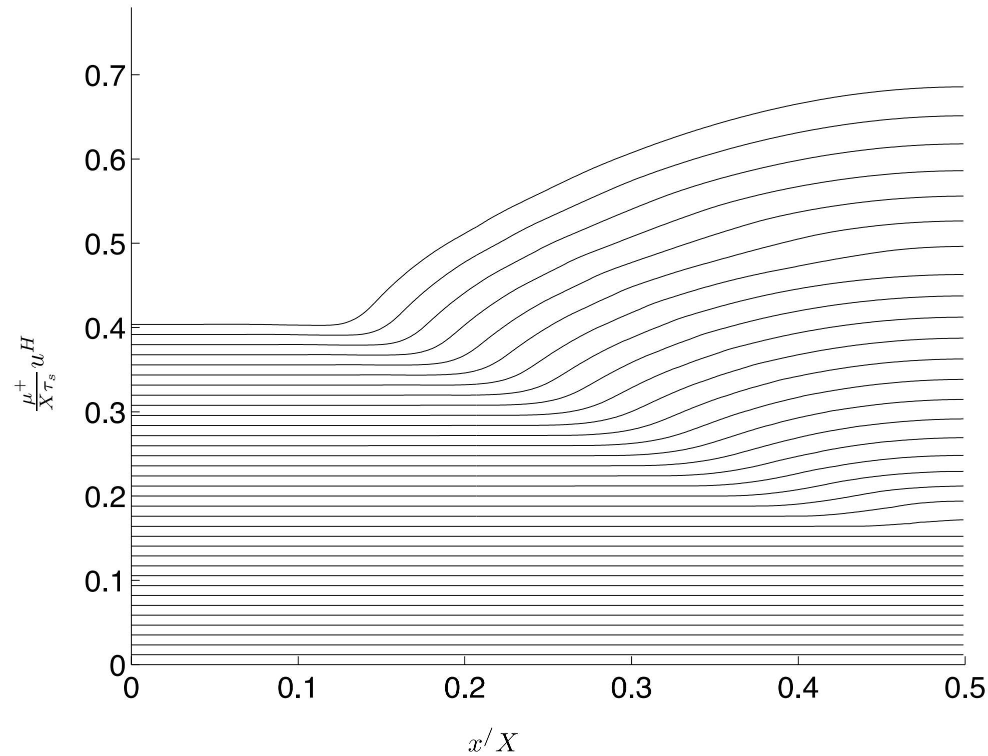

Figure 7.4: Evolution between $t = 0$ and $t \approx 5H/c_s^+$ of the displacement at the surface of the thin film u^H for the weak interface delamination problem. The time period between the lines is $.1465H/c_s^+$. This plot shows the influence of the crack on the surface displacement beginning at $t = 2H/c_s^+$. One can also see that the further reflections do not have a visible influence on this displacement.

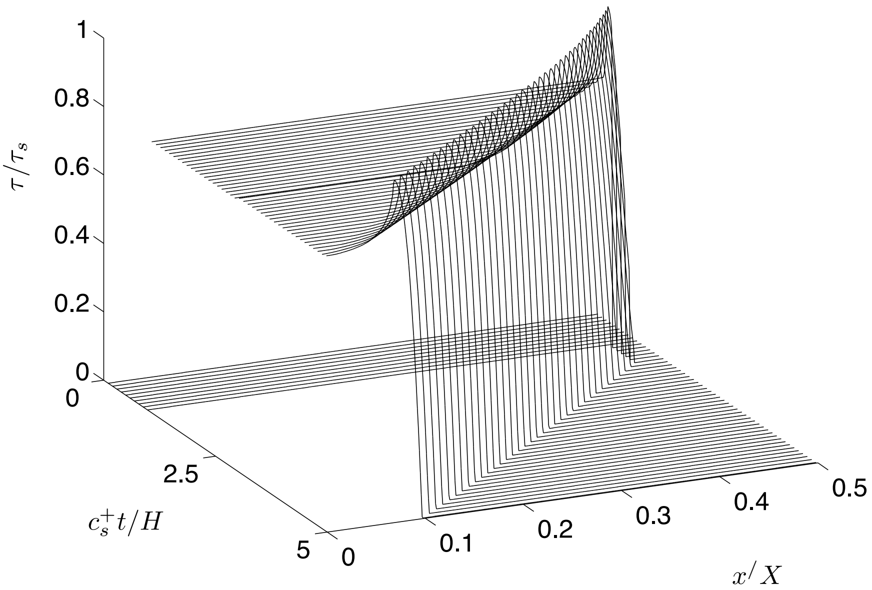

Figure 7.5: Evolution between $t = 0$ and $t \approx 5H/c_s^+$ of the traction stress at the interface τ for the weak interface delamination problem, showing the stress concentration in the neighborhood of the propagating crack tip.

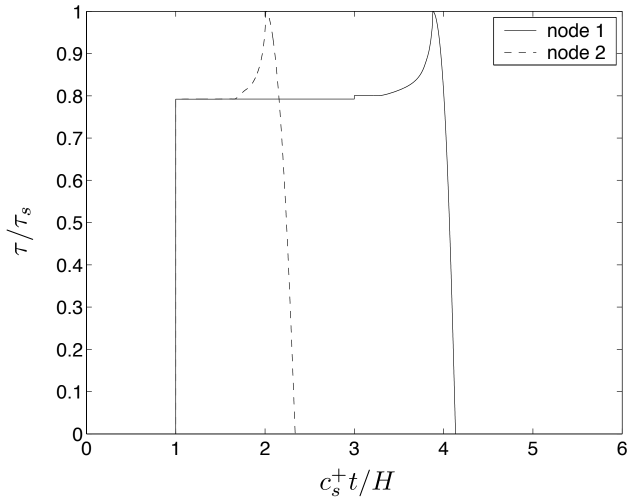

Figure 7.6: Evolution of the stress at the interface for nodes 1 and 2 defined in Figure 7.1 for the weak interface delamination problem, showing the small influence of the wave reflection at $t = 3H/c_s^+$ and the rise of the stress just before the crack reaches the nodes.

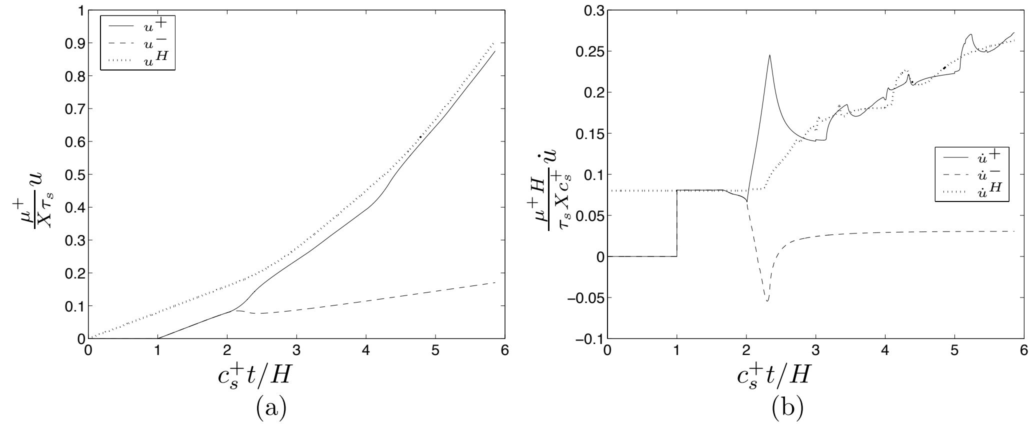

Figure 7.7: Evolution of the interface and external boundary displacements (a) and velocity (b) for a node 2 defined in Figure 7.1. Note that while the velocity of the substrate side stays almost constant after the large variation following the separation of the two sides, the velocity of the thin film side seems to increase at an on-average constant rate, and that the behavior of the interface side of the thin film becomes close to that of its surface.

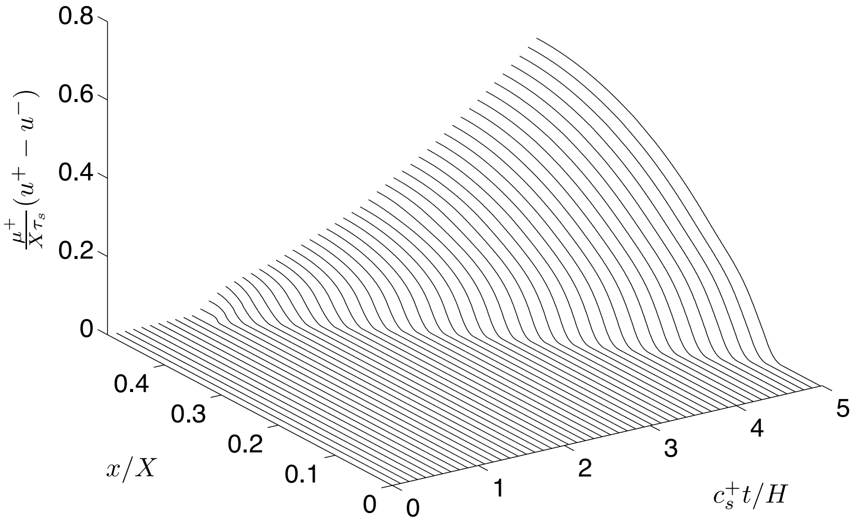

Figure 7.8: Evolution of the slip across the interface for the weak interface delamination problem, showing a continuous propagation of the crack and augmentation of the slip at the center of the crack.

7.2 Strong interface

In order to detect the influence of waves coming from the crack and reaching the crack tips after being reflected off the film surface, we consider here the case of a stronger interface that leads to a slower crack propagation. The geometry of the problem is similar to the one described in Figure 7.1 except that $H/L_c = 0.4$ so that the time needed for the wave to cross the film is relatively smaller. To be more accurate in our observations, we use a zoomed-in version of the system with $L_c = X/4$.

The loading is $\tau^H = 0.8\tau_s H(t)$ as in Section 7.1.1, but the cohesive parameters are now doubled, $\tau_{str0} = 2\tau_s$ and $\delta_c = \delta_{c0} = 0.104\frac{\tau_s}{\mu^+}X$. So, if we use a film thickness of $H = 100\mu m$ and a typical interface strength of $\tau_s = 500MPa$, we have $\tau^H = 400MPa$, $L_c = 250\mu m$ and the parameters of the strong interface are $\delta_0 \approx 2\mu m$ and $\tau_{str0} = 1GPa$. Note that we use again $\eta = 2048$, $\Delta x = X/1024$ and thus $\beta = 0.06$.

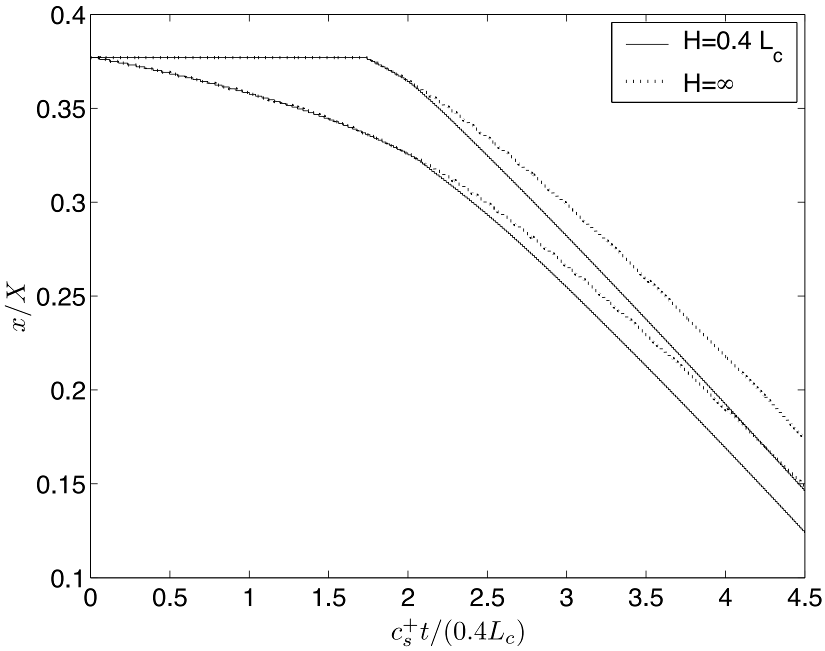

Figure 7.9: Comparison of the evolutions of the crack and cohesive zone tips a for film of finite and infinite thickness in the case of a strong interface, showing an acceleration of the propagation due to the wave reflection of the wave on the surface. $t = 0$ corresponds here to the arrival of the initial shear wave on the interface.

To study the influence of the wave reflections, we compare the dynamic response of this system with the response of a similar system with an infinite thickness. To simulate this infinite thickness, we apply a load $\tau^H(x,t) = \tau_0^H H\left(t - \frac{H}{c_s^+}\right)$, and we take the limit for H tending to infinity of l^+ appearing (2.14). This yields

$$\frac{\mu^+}{c_s^+}\dot{u}^+(x,t) + \tau^+(x,t) = f^{+\infty}(x,t) + 2\tau_0^H H(t),$$

which replaces (2.14) and where the newly introduced convolution term is given in the Fourier domain by

$$F^+(t;q) = -\mu^+ |q| \int_0^t C_\infty(|q|\, c_s^+ t') U^+(t-t';q)\, |q|\, c_s^+ dt'.$$

As shown in Figure 7.9, the waves reflected off the surface and coming back on the lower boundary of the film accelerate the propagation of the crack. The effect is indeed too large to be caused only by the small stress augmentation associated with the reflection of the initial plane wave, since, due to the value of k defined by (7.2), it only causes stress variations smaller than $2\tau_s/100$. One can also see that, before the first reflection, the evolution of the crack does not depend of the possible finite thickness of the film.

7.3 Dynamic delamination along Al/Si interface with a loading on the substrate

In this section, we consider the same system and discretization as in Section 7.1.1, but, to be closer of the experiments of [12], we replace the loading on the film surface by a plane shear wave coming from the substrate.

To simulate this loading, we consider the substrate as a thin film with a thickness H_s on the surface of which a shear stress $\tau^B = \tau_0^B H\left(t - \frac{H}{c_s^-}\right)$ would be applied. We then take the limit of the obtained formulation for an infinite value of H_s, as done for the infinite case in Section 7.1.1. The relation (2.8) derived in Section 2.2 is then replaced by

$$\tau^-(x,t) - \frac{\mu^-}{c_s^-}\dot{u}^-(x,t) + 2\tau_0^B H(t) = f^-(x,t), \tag{7.3}$$

where f^- is defined by in the Fourier domain by (2.6). Note that the formulation for the thin film is unchanged, but some terms may be removed since $\tau^H \equiv 0$.

Before showing the results, it is important to note that the behavior of the stress and velocity in the absence of crack are different than in Section 7.1. One can indeed show (see Appendix C.2) that, for $t \geq 0$,

$$\tau(t) = 2\tau_0^B \frac{1}{1+\frac{\mu^- c_s^+}{\mu^+ c_s^-}} k^{n(t)}, \qquad \dot{u}(t) = -2\tau_0^B \frac{c_s^-}{\mu^-}\left(1+\frac{1}{1+\frac{\mu^- c_s^+}{\mu^+ c_s^-}} k^{n(t)}\right) \tag{7.4}$$

where $n(t) = \lfloor \frac{c_s^+ t}{2H} \rfloor$ and k is defined by (7.2). It is interesting to note that the initial and limiting values of the traction stress and the velocity depend only on the substrate properties. Moreover, at each reflection of the initial wave, the absolute value of the stress decreases and tends eventually to zero while the absolute value of the velocity tends to twice the value that we would have for a same loading applied on the surface of the film. Note that these limiting values would be those observed in the absence of thin film. The decreasing values of the stress implies that the crack should eventually decelerate, leading to a complete arrest. This effect should begin in our case after the first reflection at $t = 2H/c_s^+$, since the small value of k implies that the traction stress would then take value smaller than 1% of the original value.

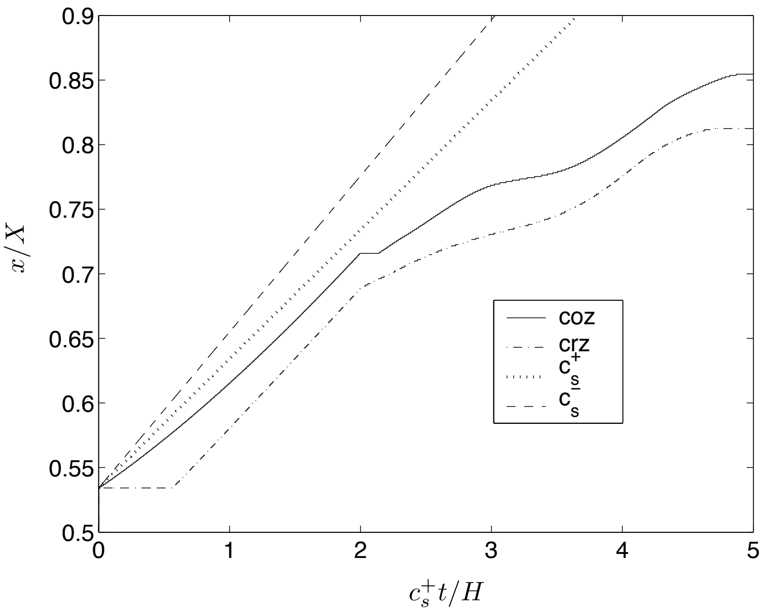

Figure 7.10: Evolution of the tip of the cohesive zone (coz) and of the crack tip (crz) in the case of a shear wave coming from the substrate. c_s^+ and c_s^- denote the propagation of elastic waves in the film and substrate respectively. This plot shows the rapid deceleration of the crack after $t = 2H/c_s^+$ and its arrest at $t = 4.6H/c_s^+$. Note that, before $t = 2H/c_s^+$, the evolution is identical to the case of thin film with an infinite thickness.

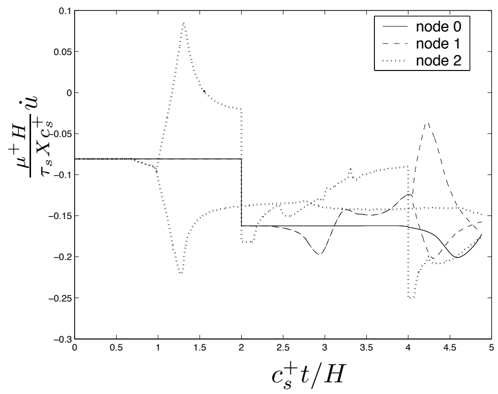

(a)

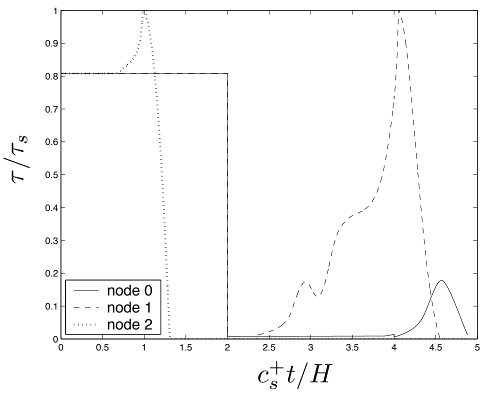

(b)

Figure 7.11: Evolution of the interface velocities (a) and traction stress (b) for nodes 0,1 and 2 defined in Figure 7.1, in the case of a shear wave coming from the substrate. For node 0 located away from the crack, the velocity and traction stress take the values predicted by (7.4) until the arrival of the wave associated with the crack. Unlike in Figure 7.7, the velocities do not tend to increase with time.

We can see in Figure 7.10 that the crack propagation indeed arrests as predicted before, but this does not occur at $t = 2H/c_s^+$. At this time, in the region not yet reached by the crack, the traction stress falls to nearly zero as shown in Figure 7.11. However, the evolution of the traction stress predicted by (7.4) does not apply to the crack zone, where the waves are being reflected off what becomes a traction free lower boundary. There remains thus traction stress concentrations around the crack tips as shown in Figure 7.12, and the crack continues to propagate at a slower rate until approximately $t = 4.6H/c_s^+$. Due to the elasticity of the thin film, the slip across the interfaces begin to decrease after approximately $t = 4H/c_s^+$, as shown in Figure 7.13. This result constitutes another main difference with the problem of Section 7.1.1 and can also be seen by comparing the evolutions of the velocities in Figures 7.7 and 7.11. Unlike in the case of a loading on the film surface, the velocity of the upper part of the interface does not seem here to increase constantly.

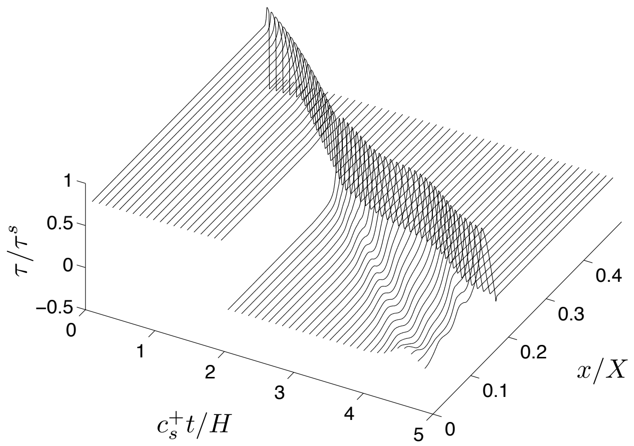

Figure 7.12: Evolution of the interface traction stress in the case of a shear wave coming from the substrate, showing the remain of the stress concentrations around the crack tips after $t = 2H/c_s^+$ while the traction stress outside the crack diminishes to nearly zero. One can also see that while the crack slows down and eventually arrest at $t = 4.6H/c_s^+$, a traction stress wave continues to propagate at the shear wave speed along the fracture plane.

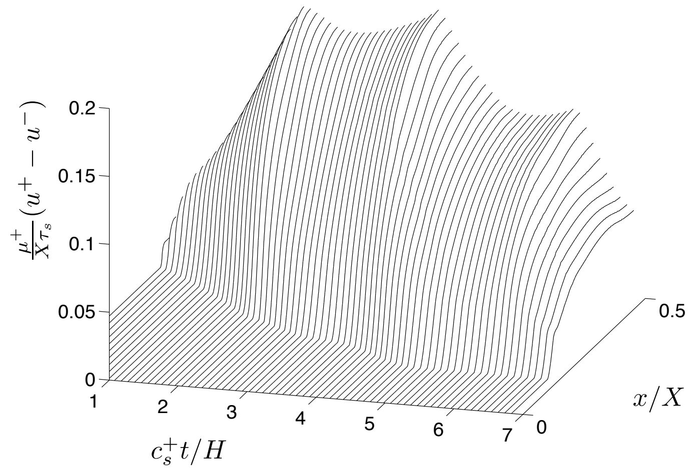

Figure 7.13: Evolution of the slip across the interface in the case of a shear wave coming from the substrate, showing the arrest of the crack at $t \approx 4.6H/c_s^+$ and a diminution of the slip beginning after $t = 4H/c_s^+$. Note that one can also see the influence of the reflections of the initial plane wave after each period of $2H/c_s^+$.

7.4 Delamination and spallation of Al/Steel interface

In this section, we analyze the dynamic behavior of an interface between a substrate an a thin film made of materials with more disparate properties: steel and aluminium (see Table 7.1) for which the absolute value of the impedance mismatch parameter is $|k| = 0.4954$. As in the initial formulation described in Chapter 2, the shear stress is applied at the surface of the thin film. This combination of materials leads to abrupt traction stress variations at the interface, which can cause interesting phenomena. In Section 7.4.1, we analyze the case of a system unstable from the point of view of the static analysis, but where a crack can propagate for a certain period of time before a complete spallation. We consider then in Section 7.4.2 the opposite case of a system stable from the static point of view, but where a spallation take place at the arrival of the initial shear wave. Note that we present here two extreme cases, but, even when no spallation take place, the combination of materials with disparate properties can lead to large variations of the crack speed at each reflection.

Material	μ (GPa)	ρ (kg/m^3)	c_s (m/s)
Aluminium	26.0	2710	3097.4
Steel AISI C120	78.8	7850	3168.3

Table 7.1: Material properties for aluminium and steel from [12] and [18].

7.4.1 Crack propagation in a statically unstable system

We consider here a thin film made of steel on an aluminium substrate. The problem geometry is the same as in Section 7.1, but the loading amplitude is $\tau_0^H = 1.25\tau_s$. The problem is thus unstable from the point of view of the static analysis. However, due to the dynamic stress reduction along the interface, the spallation does not occur immediately and it is thus possible to observe first the propagation of a crack.

As mentioned before, the impedance mismatch parameter k defined by (7.2) is 0.4954 for this material combination. By (7.1), in the absence of a crack, the traction stress should take the following values, as shown in Figure 7.14

$0 \to H/c_s^+$	$H/c_s^+ \to 3H/c_s^+$	$3H/c_s^+ \to 5H/c_s^+$	$5H/c_s^+ \to 7H/c_s^+$
0	$0.6307\tau_s$	$0.9432\tau_s$	$1.098\tau_s$

So, when the initial shear wave reaches the interface, the crack begin to propagates, but when $t = 5H/c_s^+$, the traction stress exceeds the strength. This results in a spallation of the whole thin film as shown in Figure 7.15 and 7.16.

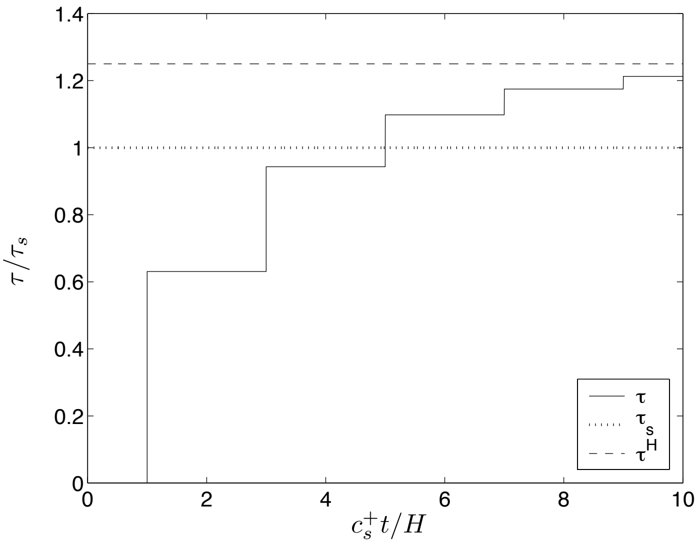

Figure 7.14: Evolution of the traction stress τ in the absence of fracture compared to the strength τ_s and the loading τ^H for an thin steel film and an aluminium substrate. The loading is larger than the strength and the system is thus unstable from a static point of view. However, due to dynamic effects, the traction stress is smaller than the strength until $t = 5H/c_s^+$. A crack propagation can thus be observed before the complete spallation of the thin film.

Note that this effect could not be observed if the shear wave was coming from the substrate as in Section 7.3, since, in that case, the absolute value of the traction stress can only decrease with time. It is also interesting to mention that the relatively important augmentation of the traction stress at $t = 3H/c_s^+$ results in a small abrupt augmentation of the cohesive zone, but does not influence the velocity of the propagation since this velocity is already close to its maximum value.

Note that we use $H = 0.05X$, $\eta = 1024$ and $\Delta x = X/1024$. The critical distance of the interface is $\delta_c = 0.05\frac{\tau_s}{\mu^+}X$ outside of the initial crack. We do not have experimental values for the strength of a steel/aluminium interface, but using $\tau_s = 500MPa$ as in the case of a Si/Al interface and $H = 100\mu m$ gives us $X = 2mm$, $\tau_0^H = 625MPa$ and $\delta_c = 0.63\mu m$

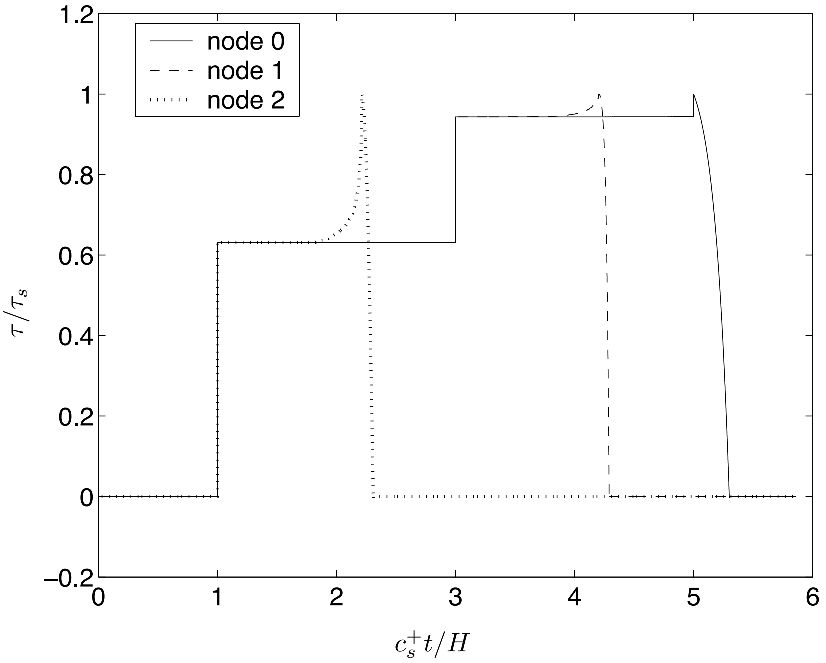

Figure 7.15: Evolution of the stress at the interface for nodes 0, 1 and 2 located on the path of the propagating crack and defined in Figure 7.1. The final rise of stress is continuous for nodes 1 and 2 and corresponds to the crack reaching theses nodes, while it is discontinuous for node 0. It corresponds there indeed to an abrupt augmentation of the stress due to a wave reflection and precedes the spallation.

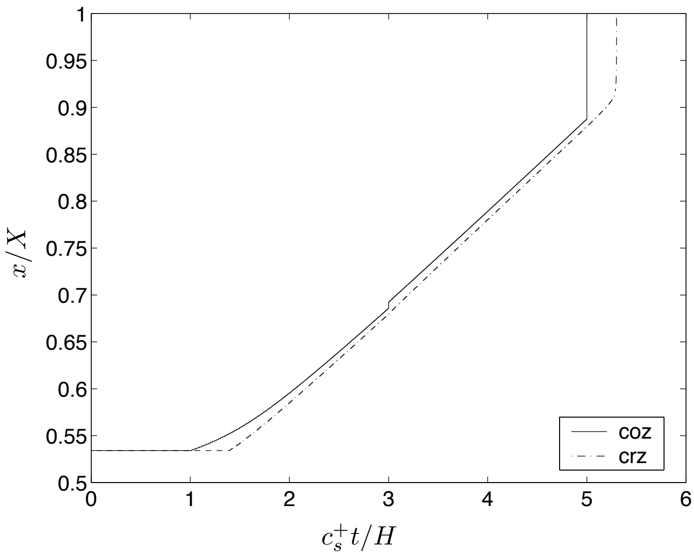

Figure 7.16: Evolution of the location of the cohesive zone tip (*coz*) and the crack tip (*crz*), showing the influence on the cohesive zone of the wave reflection at $t = 3H/c_s^+$, and the spallation beginning at $t = 5H/c_s^+$.

7.4.2 Spallation of a statically stable system

We consider here the case of an aluminium thin film on a steel substrate and show that for these materials it is possible to observe a spallation with a loading smaller than the strength. If the loading is $\tau^H = 0.8\tau_s H(t)$, a static analysis would predict that the system is stable and do not break. But, since the parameter k is in this case -0.4954, in the absence of fracture the traction stress would be $1.1963\tau_s$ for $t \in]H/c_s^+, 3H/c_s^+[$, as shown in Figure 7.17. This results in an immediate spallation of the thin film, as shown in Figure 7.18.

Note that we use the same geometry and discretization as in Section 7.4.1 and a critical distance $\delta_c = 0.01\frac{\tau_s}{\mu^+}X$. So, assuming an interface strength $\tau_s = 500MPa$ gives us $\tau_0^H = 400MPa$ and $\delta_c = 0.384\mu m$.

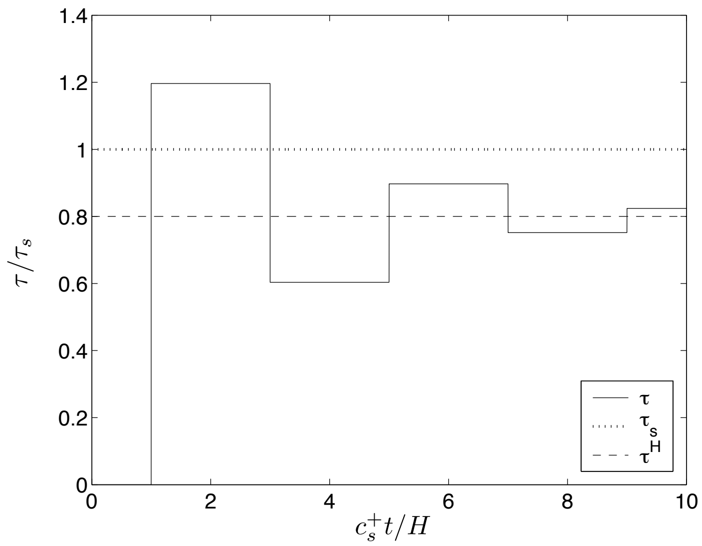

Figure 7.17: Evolution of the traction stress τ in the absence of fracture compared to the strength τ_s and the loading τ^H for an aluminium film and a steel substrate. The strength is larger than the loading and the system is therefore stable from a static point of view. However, due to dynamic effects , the traction stress exceeds the strength for $t \in (H/c_s^+, 3H/c_s^+)$, which causes the spallation of the thin film.

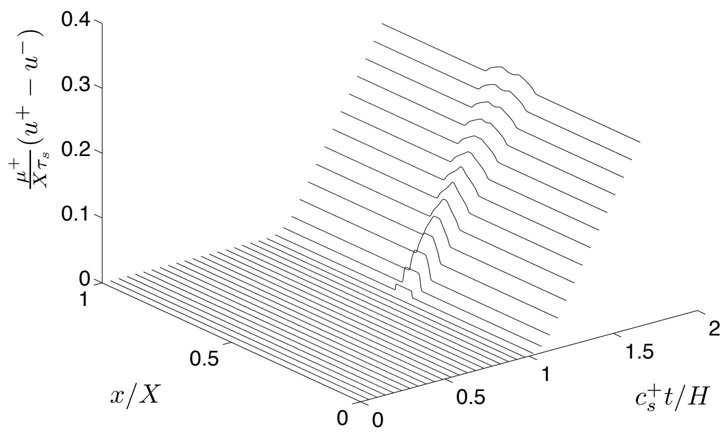

Figure 7.18: Evolution of the slip at the interface $u^+ - u^-$, showing the spallation when the shear waves reaches the interface. Note that in the zone where the initial strength is null, the velocity is larger at the beginning.

Chapter 8

Extension to finite length domains

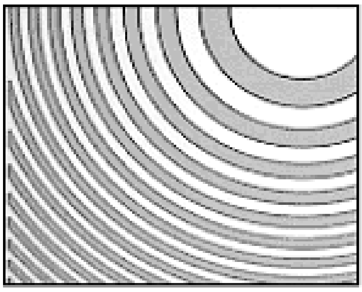

Figure 8.1: Example of pattern used for a piezo transducer (PZT) thin film on a Si substrate. The dark region correspond to the PZT [19],[20]

Some recent thin film applications such as some micro- and nano-electronic, optical, and mechanical devices involve patterned films with complex shapes, as shown in Figure 8.1. A promising avenue for the fabrication of these patterned film devices is provided by the soft lithographic techniques introduced by Whitesides and colleagues in the early 1990s [21], [22]. Interfacial adhesion is a critical parameter for these processes. Successful patterning requires indeed either the complete elimination of crack defects or highly controlled cracking to form the desired pattern. Note that as in the non-patterned case, one of the most successful experimental technique proposed to extract the delamination properties is the laser-induced spallation test

In this chapter, we extend the scheme of Chapter 2 to domains with finite length (Figure 8.2). We apply then the obtained formulation to the case of a thin film with a finite length initially adherent to a semi-infinite substrate (see

Figure 8.3). We show in Section 8.2 that we can capture the stress concentrations around the lower corners of the film in the case of a perfect interface and in Section 8.3 that these stress concentrations can lead to the delamination of the film in the absence of an initial crack.

8.1 Applying the boundary condition by selecting frequencies

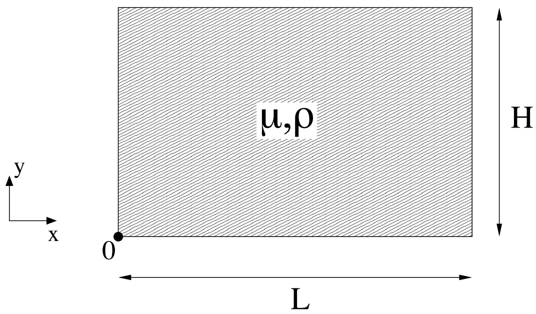

Figure 8.2: Material with finite length. Note that H does not need to be finite.

In this section, we consider a domain with a finite length L from which the two lateral boundaries are traction free and we show that the results of Section 2.1 are still valid if we replace the Fourier transform by a certain sine and cosine series. Note that, thanks to the use of the independent formulation, we can perform all this derivation for one generic domain and then apply the results either to the substrate, to the thin film or to both of them. This also includes the case of two domains with different lengths.

Let us thus consider a linear elastic rectangular material of length L and height H, and define a cartesian coordinate system, such that $y = 0$ is its lower or upper boundary and that the lateral borders are $x = 0$ and $x = L$, as shown in Figure 8.2. The only non-vanishing displacement component $u_z(x, y, t)$ is independent of the z-coordinate and satisfies the scalar wave equation (2.1)

$$c_s^2 \left(u_{z,xx} + u_{z,yy}\right) = \ddot{u}_z,$$

for $(x, y) \in [0, L] \times [0, H]$. Since the lateral boundaries are traction free, we have, in comparison to Chapter 2, two additional boundary conditions,

$$\begin{aligned} \mu u_{z,x}(x = 0) &= 0, \\ \mu u_{z,x}(x = L) &= 0. \end{aligned} \tag{8.1}$$

Instead of using a exponential development as done before, it is more convenient to use here an equivalent development in cosine and sine,

$$u_z(x,y,t) = \sum_{q\geq 0} \Omega_q(t,y)\cos(qx) + \sum_{q>0} \Omega'_q(t,y)\sin(qx), \tag{8.2}$$

where q can take any positive value. The first condition of (8.1) can then be expressed as

$$\sum_{q>0} q\Omega'_q(t,y) = 0, \qquad \forall y \in [0,H], \forall t.$$

This is only possible if $\Omega'_q \equiv 0$, for all q, which means that the second term of (8.2) is null. The second boundary condition thus becomes

$$-\sum_{q>0} q\Omega_q(t,y)\sin(qL) = 0, \qquad \forall y \in [0,H], \forall t,$$

which is only possible if, for all $q > 0$,

$$\Omega_q(t,y)\sin(qL) = 0, \qquad \forall y \in [0,H], \forall t.$$

The only q for which Ω_q can be non identically null are thus the integer multiples of $\frac{\pi}{L}$. So, the displacement can be written as

$$u_z(x,y,t) = \sum_q \Omega_q(y,t)\cos qx, \qquad q = k\frac{\pi}{L}, \qquad k \in \mathscr{N}.$$

As in Chapter 2, (2.1) must be satisfied by all spectral components. We have thus, for each $q = k\frac{\pi}{L}$,

$$\left(\frac{1}{c_s}\right)^2 \ddot{\Omega}_q = -q^2\Omega_q + \Omega_{q,yy}.$$

Taking a Laplace transform with respect to the time, this becomes

$$\hat{\Omega}_{q,yy} = \alpha_s^2 q^2 \hat{\Omega}_q,$$

where

$$\alpha_s = \sqrt{1 + \left(\frac{p}{qc_s}\right)^2},$$

which is exactly the same equation as (2.2). All the further results are thus the same.

This shows thus that the spectral scheme for domains with a finite length is totally similar to the scheme with an infinite length as soon as one replace the Fourier transform and thus the FFT by a cosine development. The implementation is thus similar. However, it is important to note that in the infinite

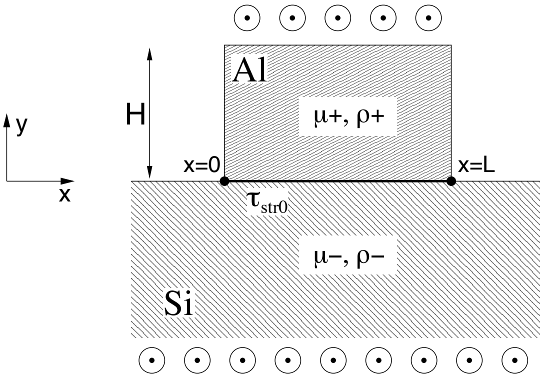

Figure 8.3: Thin film of finite dimension on a semi-infinite substrate. Typical length : $L = 500\mu m$, $X = 2mm$ (where X is the length on which the simulation is performed) and $H = 100\mu m$, which implies $H/c_s^+ = 32.28ns$.

length case the frequency discretization is imposed for computational reasons while in the finite length case it results from the mathematical formulation.

If the lengths of the two materials are different, one needs to make sure that the discretization points are the same for both of them at the interface. It is then also needed to modify slightly the implementation of the cohesive model by imposing a zero traction condition at the points that belong only to one material, for example in the zone before $x = 0$ or after $x = L$ in in Figure 8.3. Note that, for a finite domain, even if the problem solved by the numerical scheme is still theoretically periodic, there is no more influence from the adjacent domains.

8.2 Perfect interface

We consider here the dynamic response of a perfect interface between a semi-infinite substrate made of fused silica and an aluminium thin film with a finite length on the surface of which a shear stress $\tau^H(x,t) = \tau_0^H H(t)$ is applied as shown in Figure 8.3 using $\tau_{str0} = \infty$. Note that we use $\Delta x = X/2048$ and $\eta = 2048$.

As one can see in Figure 8.4, the scheme developed in Section 8.1 is able to capture the stress concentrations appearing on the lower corners of the film. In Figure 8.5, we can see the displacement of the substrate boundary. Note that due to the absence of crack and the small value of k defined by (7.2), there is no visible effect caused by plane reflection of the initial shear wave at $t = (2n+1)H/c_s^+$.

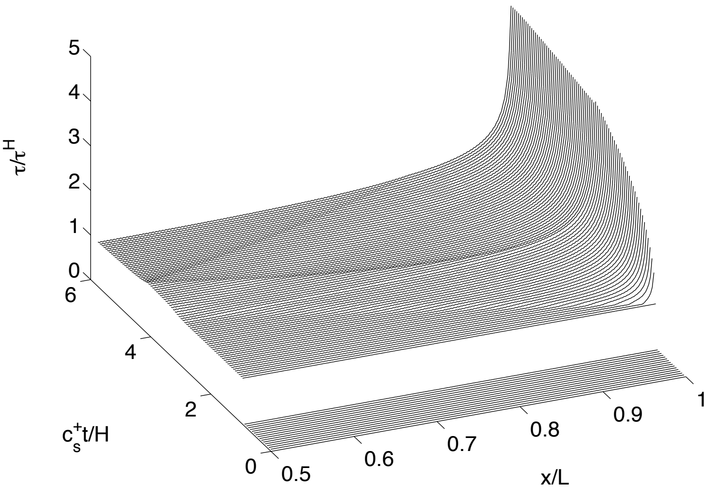

Figure 8.4: Evolution of the traction stress along a perfect interface between the substrate and the film, showing the stress concentrations appearing at the lower corners of the film. The origin $x = 0$ is defined in Figure 8.3.

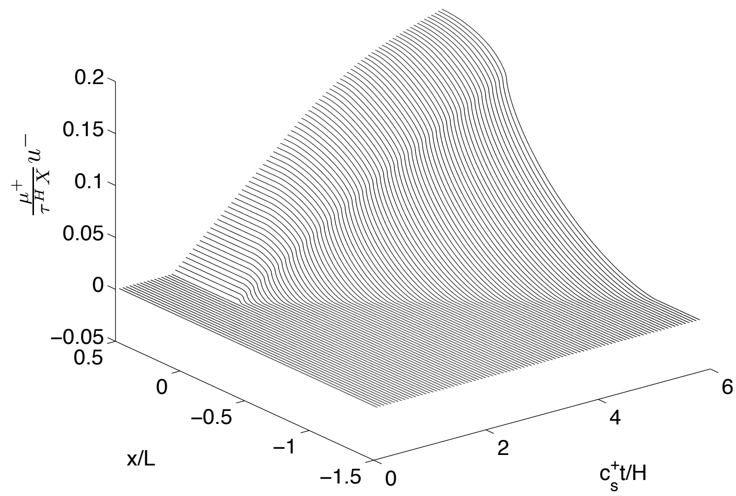

Figure 8.5: Evolution of displacement of the top boundary of the substrate, showing the surface wave generated by the loading of the film, starting at the arrival of the wave at $t = H/c_s^+$. The origin $x = 0$ is defined in Figure 8.3.

.

8.3 Delamination in the absence of an initial crack

In this section, we consider the case of an interface with a finite strength τ_s and show that due to the stress concentrations appearing in the lower corners of the film, a delamination can take place in the absence of an initial crack. We use the same material and geometry as in Section 8.2, but to be closer to a real situation we consider a constant shear wave τ^B coming from the substrate instead of a loading τ^H applied on the film surface. The cohesive properties of the interface are $\tau_{str0} = \tau_s$ and $\delta_c = 0.013\tau_s\mu^+/X$ and the load is $\tau^B = 0.4\tau_s$. So, using a typical strength $\tau_s = 500MPa$, we have $\tau^B = 200MPa$ and $\delta_c = 0.5\mu m$. Note that we use the same space- and time-discretization as in Section 8.2.

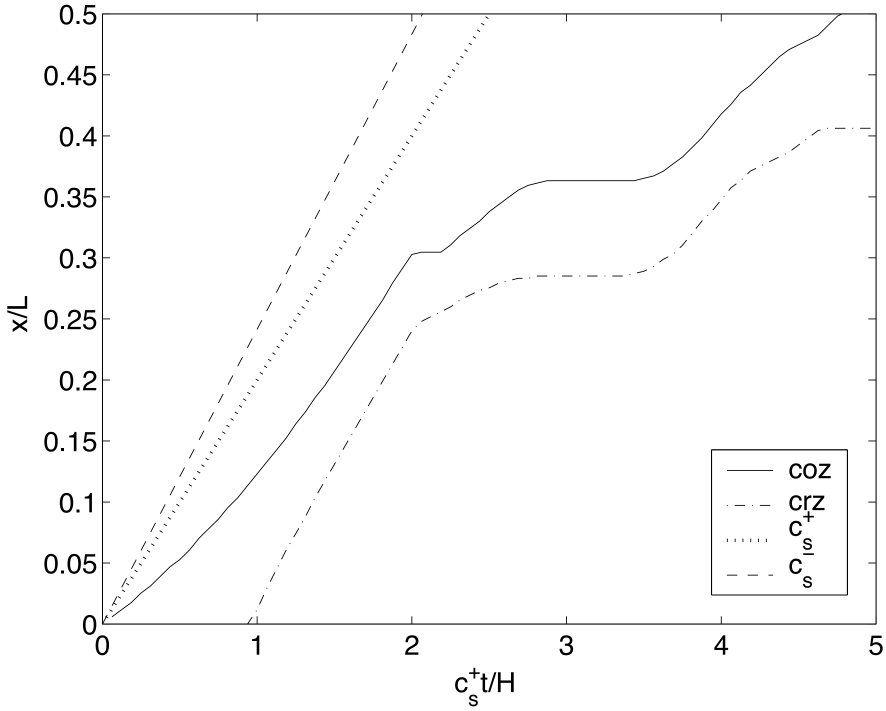

Figure 8.6: Evolution of the location of the left crack tip (*crz* - point at which $\delta = \delta_c$) and left cohesive zone tip (*coz* - point at which $\delta > 0$) for a thin film of length L loaded by a plane substrate wave. $x = 0$ denotes the left corner of the film (Figure 8.3). The lines labelled c_s^+ and c_s^- correspond to the propagation of elastic waves along the film and substrate, respectively. Note the deceleration of the crack beginning at $t = 2H/c_s^+$ leading to a temporary arrest before a new propagation at about $t = 3.6H/c_s^+$.

As in Section 7.3, the small value of k defined by (7.2) implies that, far from the crack tips, the stress should fall to nearly 0 at $t = 2H/c_s^+$. This would lead to a deceleration of the crack. Figure 8.6 shows us that the cracks propagate at an intersonic speed before $t = 2H/c_s^+$ and then begin indeed to decelerate and totaly arrests at $t \approx 2.8H/c_s^+$. But, at $t \approx 3.45H/c_s^+$, propagations begin again.

Looking at the evolution of the interface traction stress in Figure 8.7a, we can see that far from the crack tip the stress falls to nearly zero when the plane reflection of the initial shear wave reaches the interface at $t = 2H/c_s^+$. This diminution causes the crack to decelerate and eventually arrest. But one can see on the zoomed-in features (Figure 8.7b) that, when the propagation decelerates, a wave continues to propagate from each crack tip at the shear wave speed, and that when this wave reaches the other crack tip a small augmentation of the stress concentration takes place and the delamination begins again. The re-acceleration of the crack propagation after a period of arrest could thus be explained by this small wave interfering constructively with the stress concentrations around the crack tips. This would be confirmed by the chronology of the different events. When the crack decelerates, the cohesive zones tips are located at $x \approx 0.3L$ and $x \approx 0.7L$ (see Figure 8.6), and when the propagation re-accelerates they are located at $x \approx 0.36L$ and $x \approx 0.64L$. The time needed for a wave propagating at the substrate shear wave speed to go from one crack tip to the other is thus approximatively $0.14H/c_s^+$, which is very close to the time between the cracks deceleration and their re-acceleration.

In Figure 8.8, one can see in addition of the evolution of the crack that the slip at the extremities take smaller values between angular points occurring at each reflection of the initial shear wave at $t = 2nH/c_s^+$ but that there is nearly no influence of these reflections in the neighborhood of the crack tips. At the extremities, the lower boundary of the film is indeed traction free. The plane wave is thus totally reflected when it comes back on this surface. On the other hand, in the part of the interface not yet reached by the crack the wave is almost totally transmitted. This explains why no visible major change in the slip takes place there at $t = 2nH/c_s^+$.

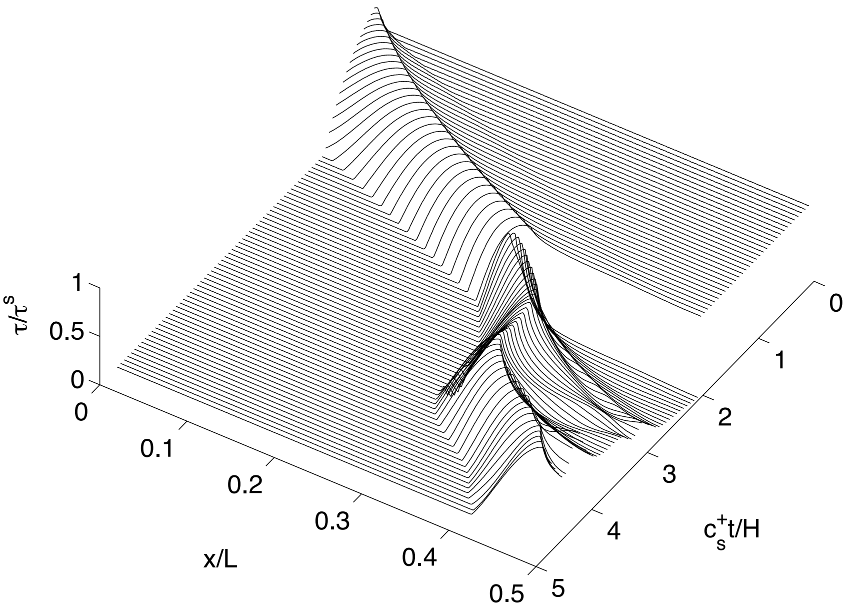

(a)

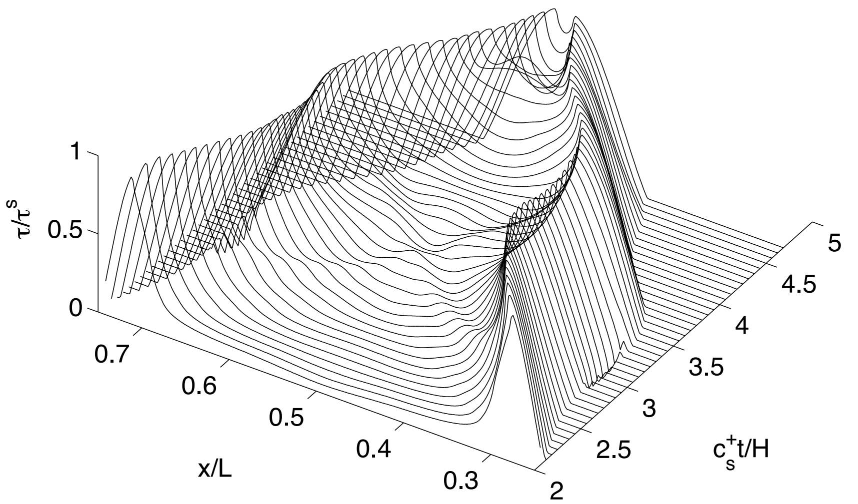

(b)

Figure 8.7: Evolution of the interface traction stress, showing a diminution at $t = 2H/c_s^+$, leading to a deceleration and temporary arrest of the crack. As shown in the zoomed-in features in (b), a stress wave continues to propagate from each crack tip at $t = 2H/c_s^+$, and that when this wave reaches the other crack tip, the cracks re-accelerate. The origin $x = 0$ is defined in Figure 8.3.

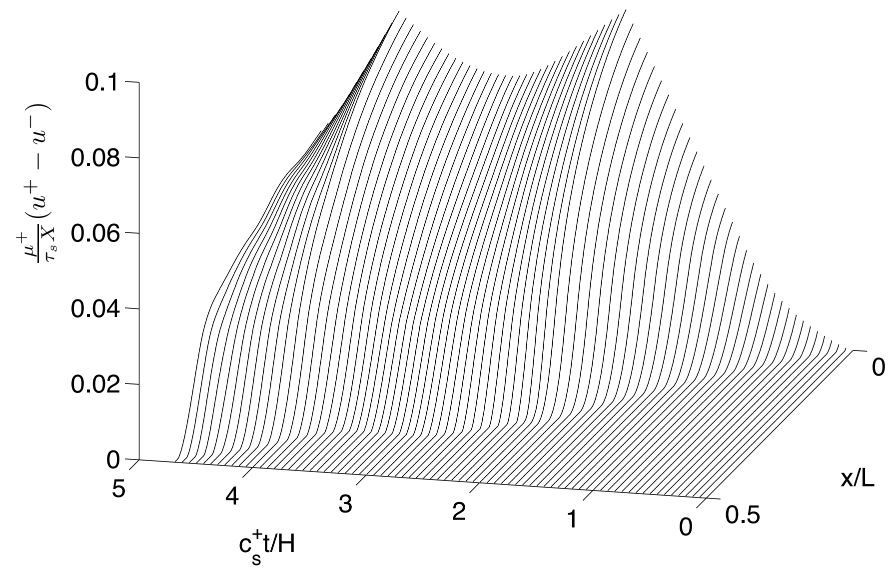

Figure 8.8: Evolution of the slip across the interface, showing a deceleration of the crack beginning at $t = 2H/c_s^+$ leading to a temporary arrest before a new propagation at about $t = 3.6H/c_s^+$. One can also see the diminution of the slip at the extremities of the film after the angular points at $t = 2H/c_s^+$ and $t = 4H/c_s^+$. The origin $x = 0$ is defined in Figure 8.3.

Chapter 9

Conclusions and future works

9.1 Conclusions

A spectral scheme has been derived to analyze various film delamination problem in mode III, leading to a numerical scheme based on an exact spectral representation of the elastodynamic equations in each domain. The accuracy of this scheme was tested by comparing the numerical results to an analytical solution available in the case of a single mode loading. This showed a linear dependance of the error with respect to the time-discretization and an increase of the error at each reflection of the initial wave off the interface. It also showed the appearing of instabilities for large space frequencies cases. To stabilize the scheme, a filter was chosen using a "worst case" frequency analysis of the different terms involved in the mathematical formulation. The use of a first order low-pass filter in the scheme was then proved to remove the instabilities without affecting the rest of the solution.

The improved scheme has shown to provide a very accurate description of the shear stress and out-of-plane displacements along the fracture plane and the surface of the film, including the vicinity of the crack tips. In the case of a non-propagating crack, it could capture with a great accuracy the influence of waves reflected off the crack or the film surface on the evolution of the stress intensity factor characterizing the importance of the stress concentration around the crack tips. It could also show the influence of the crack on the behavior of the film surface where measure can be made.

The scheme was used to analyze the influence of the finite thickness of the film on a propagating crack in the case of a loading applied along the surface or in the case of a shear wave coming from the substrate. This last case was shown to lead to the arrest of the crack after a period of deceleration.

It also showed that the use of materials with disparate properties could lead to interesting phenomena such as an interface crack propagation before a total delamination of the film in a statically unstable system, or the immediate delamination of the film in a statically stable system.

The scheme was extended to the case of a film of finite length. This extended scheme could capture accurately the interface stress concentrations in the neighborhood of the film limits, and showed that these stress concentrations could lead to a delamination even in the absence of an initial crack. In the case of a shear wave coming from the substrate, it also showed some very interesting phenomena such as the temporary arrest of a crack before a re-acceleration.

9.2 In-plane problems

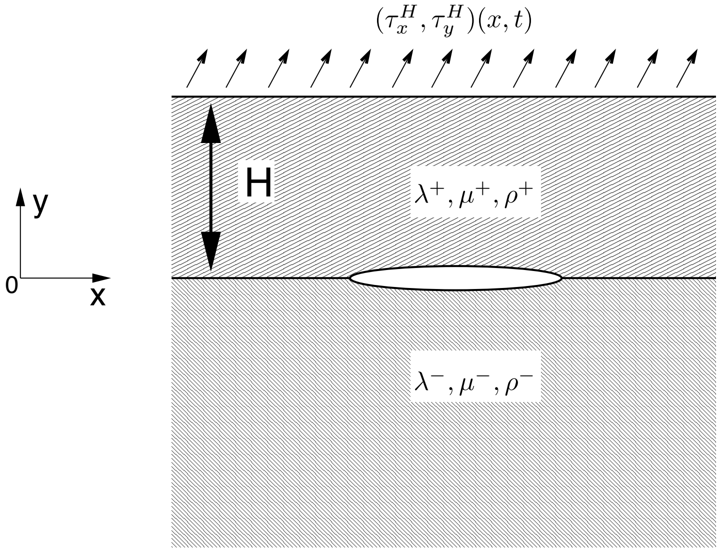

Figure 9.1: In plane problem.

A natural extension of this work is to consider a problem similar to that of Chapter 2, but with an in-plane load, stress and displacement, as shown in Figure 9.1. We have then to consider the 2-D displacement $(u_x(x,y,t), u_y(x,y,t))$, and the applied load is $\left(\tau_x^H(x,t), \tau_y^H(x,t)\right)$. As explained in [15], in order to solve this problem, it is more convenient to introduce the Helmotz decomposition of the displacement in terms of the potential functions ϕ and ψ,

$$u_x = \phi_{,x} + \psi_{,y}; \qquad u_y = \phi_{,y} - \psi_{,x}. \tag{9.1}$$

It can be shown that, inside a linearly elastic material, these potentials satisfy

$$\begin{array}{lclcl} c_d^2 & (\phi_{,xx}+\phi_{,yy}) & = & \phi_{,tt}, \\ c_s^2 & (\psi_{,xx}+\psi_{,yy}) & = & \psi_{,tt}, \end{array} \tag{9.2}$$

where the wave velocities are defined by

$$c_d^2 = \frac{\lambda+2\mu}{\rho} \qquad , \qquad c_s^2 = \frac{\mu}{\rho}.$$

where λ and μ are the Lamé constants. Performing a Fourier/Laplace transform on (9.2) leads to

$$\begin{array}{l} \hat{\Phi}_{,yy}(y;p,q) = q^2\alpha_d^2\hat{\Phi}(y;p,q) \\ \hat{\Psi}_{,yy}(y;p,q) = q^2\alpha_s^2\hat{\Psi}(y;p,q). \end{array} \tag{9.3}$$

The introduced variables α_s, α_d are defined by

$$\alpha_d = \sqrt{1+\frac{p^2}{q^2c_d^2}}, \qquad \alpha_s = \sqrt{1+\frac{p^2}{q^2c_s^2}}, \tag{9.4}$$

Resolving (9.3) in the general case gives us

$$\begin{array}{lll} \hat{\Phi}(y;p,q) & = \hat{\Phi}_A(p,q)e^{q\alpha_d y} & +\hat{\Phi}_B(p,q)e^{-q\alpha_d y} \\ \hat{\Psi}(y;p,q) & = \hat{\Psi}_A(p,q)e^{q\alpha_s y} & +\hat{\Psi}_B(p,q)e^{-q\alpha_s y}. \end{array} \tag{9.5}$$

Since we are mainly interested in the displacement and stress at the interface, let us consider

$$(v_x,v_y)(x,t) = (u_x,u_y)(x,y=0,t),$$

and

$$(\tau_x,\tau_y)(x,t) = \left(\mu\left(\frac{\partial u_x}{\partial y}+\frac{\partial u_y}{\partial x}\right), (2\mu+\lambda)\frac{\partial u_y}{\partial y}+\lambda\frac{\partial u_x}{\partial x}\right)(x,y=0,t).$$

Taking a Fourier/Laplace transform on this newly introduced variables yields

$$\begin{array}{l} (\hat{V}_x,\hat{V}_y)(x,t) = (\hat{U}_x,\hat{U}_y)(x,y=0,t) \\ (\tau_x,\tau_y)(x,t) = \left(\mu\left(\hat{U}_{x,y}+iq\hat{U}_y\right), (2\mu+\lambda)\,\hat{U}_{y,y}+\lambda iq\hat{U}_x\right)(x,y=0,t). \end{array}$$

Using (9.1) and (9.5), we get

$$\begin{array}{rrcrcrcr} \hat{V}_x = & qi\hat{\Phi}_A & + & qi\hat{\Phi}_B & + & q\alpha_s\hat{\Psi}_A & - & q\alpha_s\hat{\Psi}_B \\ \hat{V}_y = & q\alpha_d\hat{\Phi}_A & - & q\alpha_d\hat{\Phi}_B & - & qi\hat{\Psi}_A & - & qi\hat{\Psi}_B, \end{array} \tag{9.6}$$

and

$$\begin{array}{rrcr} \hat{T}_x = & 2\mu q^2 i\alpha_d\hat{\Phi}_A & - & 2\mu q^2 i\alpha_d\hat{\Phi}_B \\ & +\mu q^2(1+\alpha_s^2)\hat{\Psi}_A & + & \mu q^2(1+\alpha_s^2)\hat{\Psi}_B \\ & & & \\ \hat{T}_y = & \left((2\mu+\lambda)\alpha_d^2-\lambda\right)q^2\hat{\Phi}_A & + & \left((2\mu+\lambda)\alpha_d^2-\lambda\right)q^2\hat{\Phi}_B \\ & -2\mu q^2 i\alpha_s\hat{\Psi}_A & + & 2\mu\alpha_s q^2 i\hat{\Psi}_B. \end{array} \tag{9.7}$$

As in Chapter 2, we now need to apply a boundary condition to $(\hat{U}_x, \hat{U}_y)$ in order to eliminate $\hat{\Phi}_A, \hat{\Phi}_B, \hat{\Psi}_A$ and $\hat{\Psi}_B$ in (9.6) and (9.7).

In the substrate, we need to keep the solution finite when $y \to -\infty$. We have thus

$$\begin{array}{lll} \Phi_B^- = \Psi_B^- = 0 & \text{if} & q > 0 \\ \Phi_A^- = \Psi_A^- = 0 & \text{if} & q < 0. \end{array}$$

This relation allows us to bind $(\hat{V}_x^-, \hat{V}_y^-)$ and $(\hat{T}_x^-, \hat{T}_y^-)$. Back in the time/space domain, this leads to a relation between (v_x^-, v_y^-) and (τ_x^-, τ_y^-), as described in [15].

In the thin film, the load applied on the external boundary $(y = H)$ can be expressed as

$$(\tau_x^H, \tau_y^H)(x,t) = \left(\mu\left(\frac{\partial u_x}{\partial y} + \frac{\partial u_y}{\partial x}\right), (2\mu+\lambda)\frac{\partial u_y}{\partial y} + \lambda\frac{\partial u_x}{\partial x}\right)(x, y = H, t).$$

In the Fourier/Laplace domain, this becomes

$$(\hat{T}_x^H, \hat{T}_y^H)(x,t) = \left(\mu\left(\hat{U}_{x,y} + iq\hat{U}_y\right), (2\mu+\lambda)\,\hat{U}_{y,y} + \lambda iq\hat{U}_x\right)(x, y = H, t).$$

Using (9.1) and (9.5), we get

$$\begin{array}{rrcr} \hat{T}_x^H = & 2\mu q^2 i\alpha_d e^{a\alpha_d}\hat{\Phi}_A & - & 2\mu q^2 i\alpha_d e^{-a\alpha_d}\hat{\Phi}_B \\ & +\mu q^2(1+\alpha_s^2)e^{a\alpha_s}\hat{\Psi}_A & + & \mu q^2(1+\alpha_s^2)e^{-a\alpha_s}\hat{\Psi}_B \\ \\ \hat{T}_y^H = & \left((2\mu+\lambda)\alpha_d^2 - \lambda\right) q^2 e^{a\alpha_d}\hat{\Phi}_A & + & \left((2\mu+\lambda)\alpha_d^2 - \lambda\right) q^2 e^{-a\alpha_d}\hat{\Phi}_B \\ & -2\mu q^2 i\alpha_s e^{a\alpha_s}\hat{\Psi}_A & + & 2\mu\alpha_s q^2 i e^{-a\alpha_s}\hat{\Psi}_B, \end{array} \quad (9.8)$$

with $a = qH$. In order to derive a relation between (v_x^+, v_y^+), (τ_x^+, τ_y^+) and (τ_x^H, τ_y^H), one would need to eliminate $\hat{\Phi}_A, \hat{\Phi}_B, \hat{\Psi}_A$ and $\hat{\Psi}_b$ in (9.6), (9.7) and (9.8). Then one would need to perform an inverse Laplace and Fourier Transform on the obtained 4-equation linear system. Using a cohesive model to link this and the results obtained in [15] for a semi-infinite substrate then leads to a formulation of the problem of the in-plane fracture propagation between a thin-film and an substrate, similar to that obtained in Chapter 2.

Bibliography

[1] O.S. Heavans. Some factors infulencing the adhesion of films produces by vacuum evaporation. *Journal of Mechanics and Physics of Solid*, 11:355–360, 1950.

[2] C. Weaver. Adhesion of thin films. *Journal of Vacuum Science and Tehnology*, 12:18–25, 1975.

[3] J.S. Collignon T.R. Hull and A.E. Hill. Measurement of thin film adhesion. *Vacuum*, 37:327–330, 1987.

[4] J. Strong. On the cleaning of surface. *Review of Scientific Instruments*, 6:97–98, 1935.

[5] J.E.E. Baglin and G.C. Clarck. Ion beam bonding of thin film. *Nuclear Instruments and Methods in Physics Reseqrch Section B-Beam Interactions with Materials and Atoms*, B7/8:881–885, 1950.

[6] R. Jacobsson and B. Kruse. Measurement of adhesion of thin evaporated films glass substrates by means of the direct pull method. *Thin Solid Films*, 15(1):71–77, 1973.

[7] R. Jacobsson. Measurement of adhesion of thin films. *Thin Solid Films*, 34:191–199, 1976.

[8] A.N. Gent and L.H. Lewandowski. Blow-off pressures for adhering layers. *Journal of Applied Polymer Science*, 33:1567–1577, 1987.

[9] R.C. White Y.Z. Chu, H.S Jeong and C.J. Durning. Measurement of adhesion of thin evaporated films glass substrates by means of the direct pull method. *MRES Symposium Proceedings*, 276:209–220, 1992.

[10] W.W. Gerberich M.D. Kriese and N.R. Moody. Quantitative adhesion measures of multilayer films: Part i. indentation mechanics. *Journal of Materials Research*, 14(7):3007–3018, 1999.

[11] W.W. Gerberich M.D. Kriese and N.R. Moody. Quantitative adhesion measures of multilayer films: Part ii. indentation of w/cu, w/w, cr/w. *Journal of Materials Research*, 14(7):3019–3026, 1999.

[12] J. Wang. *Thin-film adhesion measurement by laser-induced stress waves.* PhD thesis, University of Illinois.

[13] J.W Morrissey and P.H. Geubelle. A numerical scheme for mode iii dynamic fracture problems. *International Journal for Numerical Methods in Engineering*, 40:1181–1196, 1997.

[14] P.H. Geubelle and M.S. Breitenfeld. Numerical analysis of dynamic debonding under anti-plane shear loading. *International Journal of Fracture*, 85:265–282, 1997.

[15] P.H. Geubelle and J.R. Rice. A spectral method for three-dimensionnal elastodynamic fracture problems. *Journal of Mechanics and Physics of Solids*, 43(11):1791–1824, 1995.

[16] M.S. Breitenfeld and P.H. Geubelle. Numerical analysis of dynamic debonding under 2d in-plane and 3d loading. *International Journal of Fracture*, 93:13–38, 1998.

[17] M.E. Plesha R.D. Cook, D.S. Malkus and R.J. Witt. *Concepts and applications of finite element analysis. Fourth Edition.* Wiley.

[18] http://www.apo.nmsu.edu/telescopes/sdss/eng.papers/ 19950926_conversionfactors/19950926_mproperties.html.

[19] E.A. Mikalsen and D.A. Payne. Mediated patterning of electroceramic thin films. *Journal of Electroceramics*, accepted in 2003.

[20] E.A. Mikalsen. *Mediated patterning of sol-gel thin layers, shrinkage, decohesion, and liftoff.* PhD thesis.

[21] J. P. Mathias G. M. Whitesides and C. Seto. Molecular self-assembly and nanochemistry: A chemical strategy for the synthesis of nanostructures. *Science*, 254:1312–1319, 1991.

[22] Y. Xia and G. M. Whitesides. Soft lithography. *Annual Review Material Science*, 28:153–184, 1998.

Appendix A

Laplace inversions

The purpose of this appendix is to explain how some computations, mainly some inverse Laplace transforms, are performed. Since most of these computations present some similarities, the same methodology is often used to handle them. This methodology is described in A.2. Prior to this, we present some results used in the rest of this Chapter. Note that, in the following sections, in order to avoid some overwhelming notations, we use the convention

$$f\left(\sqrt{z}\right) = f\left(\sqrt{z}\right) H(z), \tag{A.1}$$

and

$$\int_a^b f(z)dz = \left(\int_a^b f(z)dz\right) H(b-a). \tag{A.2}$$

A.1 Some useful results

A.1.1 Laplace inversion of $\frac{e^{-ms}}{ae^{ks}+be^{-ks}}$

Many the Laplace inversions that we have to perform contain some terms that can be expressed as

$$\hat{F}(s) = \frac{e^{-ms}}{ce^{ks} + de^{-ks}}. \tag{A.3}$$

In order to simplify the further computations, we show here the inversion of this generic expression.

We can rewrite $(A.3)$ as

$$\hat{F}(s) = \frac{e^{-(m+k)s}}{c} . \frac{1}{1 + \frac{d}{c}e^{-2ks}}. \tag{A.4}$$

It would be convenient to transform this last equation in order to eliminate the denominator. Let us remember that if $|z| < 1$,

$$\frac{1}{1-z} = \sum_{n=0}^{\infty} z^n.$$

To be able to use this relation in our case, we should verify that

$$\left|\frac{d}{c}e^{-2ks}\right| < 1.$$

Let us assume $R(k) \geq 0$; this is not restrictive, since one could use $k' = -k$ if its value was negative. So, if $\Re(s) > 0$, we only need the next hypothesis,

$$|d| \leq |c|\,.$$

If we assume that this condition is satisfied, we can then rewrite (A.4) as

$$\hat{F}(s) = \frac{e^{-(m+k)s}}{c} \sum_{n=0}^{\infty} \left(-\frac{d}{c}\right)^n e^{-2nks},$$

or

$$\hat{F}(s) = \frac{1}{c} \sum_{n=0}^{\infty} \left(-\frac{d}{c}\right)^n e^{-((2n+1)k+m)s}.$$

Using then the linear properties of the Laplace transform, we get

$$F(t) = \mathscr{L}^{-1}\left(\frac{e^{-ms}}{ce^{ks} + de^{-ks}}\right) = \frac{1}{c} \sum_{n=0}^{\infty} \left(-\frac{d}{c}\right)^n \delta(t - (2n+1)k - m). \quad \text{(A.5)}$$

It is important to remember that this relation is guaranteed only if we assume $k \geq 0$, and $|d| \leq |c|$.

From this result, we can directly see two important corollaries,

$$\mathscr{L}^{-1}\left(\frac{1}{s}\frac{e^{-ms}}{ce^{ks} + de^{-ks}}\right) = \frac{1}{c} \sum_{n=0}^{\infty} \left(-\frac{d}{c}\right)^n H\left(t - (2n+1)k - m\right), \quad \text{(A.6)}$$

and

$$\mathscr{L}^{-1}\left(s\frac{e^{-ms}}{ce^{ks} + de^{-ks}}\right) = \frac{1}{c} \sum_{n=0}^{\infty} \left(-\frac{d}{c}\right)^n \delta'\left(t - (2n+1)k - m\right), \quad \text{(A.7)}$$

where δ' denotes the derivative of the Dirac δ-function.

A.1.2 Integration of $v\delta'(v-k)\frac{J_1\left(\sqrt{T^2-v^2}\right)}{\sqrt{T^2-v^2}}$

Since this integration appears more than once, we perform it now in order to simplify the further computations. Let us define

$$I = \int_0^T v\delta'(v-k)\frac{J_1\left(\sqrt{T^2-v^2}\right)}{\sqrt{T^2-v^2}}dv.$$

Integrating I by part to eliminate the derivative of the Dirac δ-function, we get

$$I = \left[\delta(v-k)v\frac{J_1\left(\sqrt{T^2-v^2}\right)}{\sqrt{T^2-v^2}}\right]_0^T - \int_0^t \delta(v-k)\left(v\frac{J_1\left(\sqrt{T^2-v^2}\right)}{\sqrt{T^2-v^2}}\right)' dv. \quad \text{(A.8)}$$

The first term of this expression can be evaluated

$$\left[\delta(v-k)v\frac{J_1\left(\sqrt{T^2-v^2}\right)}{\sqrt{T^2-v^2}}\right]_0^T = \delta(T-k)T\lim_{z\to 0}\frac{J_1(z)}{z},$$

and since $J_0'(z) = \frac{1}{2}$, we get

$$\left[\delta(v-k)v\frac{J_1\left(\sqrt{T^2-v^2}\right)}{\sqrt{T^2-v^2}}\right]_0^T = \frac{k}{2}\delta(T-k).$$

We have now to compute the integral in (A.8). The derivative that appears in its expression can be developed as

$$\left(v\frac{J_1\left(\sqrt{T^2-v^2}\right)}{\sqrt{T^2-v^2}}\right)' = \frac{J_1\left(\sqrt{T^2-v^2}\right)}{\sqrt{T^2-v^2}} + v\left(\frac{J_1\left(\sqrt{T^2-v^2}\right)}{\sqrt{T^2-v^2}}\right)'.$$

Since,

$$\left(\frac{J_1(z)}{z}\right)' = -\frac{J_2(z)}{z},$$

we get

$$\left(v\frac{J_1\left(\sqrt{T^2-v^2}\right)}{\sqrt{T^2-v^2}}\right)' = \frac{J_1\left(\sqrt{T^2-v^2}\right)}{\sqrt{T^2-v^2}} + v^2\frac{J_2\left(\sqrt{T^2-v^2}\right)}{T^2-v^2}.$$

We can thus now compute the integral in (A.8),

$$\int_0^t \delta(v-k)\left(v\frac{J_1\left(\sqrt{T^2-v^2}\right)}{\sqrt{T^2-v^2}}\right)' dv = \frac{J_1\left(\sqrt{T^2-k^2}\right)}{\sqrt{T^2-k^2}} + k^2\frac{J_2\left(\sqrt{T^2-k^2}\right)}{T^2-k^2}.$$

Finally, reintroducing this result in the expression of I gives

$$I = \int_0^T v\delta'(v-k)\frac{J_1\left(\sqrt{T^2-v^2}\right)}{\sqrt{T^2-v^2}}dv = \frac{k}{2}\delta(T-k) - \frac{J_1\left(\sqrt{T^2-k^2}\right)}{\sqrt{T^2-k^2}} - k^2\frac{J_2\left(\sqrt{T^2-k^2}\right)}{T^2-k^2}. \tag{A.9}$$

Note that this result is true for any value of k, including $k = 0$.

A.1.3 Integration of $H\left(\sqrt{t^2-u^2}-k\right)J_1(u)$

This integration also appears more than once in the further sections. Let us define

$$I(t) = \int_0^t H\left(\sqrt{T^2-u^2}-k\right)J_1(u)du.$$

$I(t)$ can be rewritten as

$$I(t) = \int_0^{\sqrt{t^2-k^2}} J_1(u)du.$$

Since $J_0' = -J_1$ and $J_0(0) = 1$, this yields

$$I(t) = H(t-k)\left(1 - J_0\left(\sqrt{t^2-k^2}\right)\right). \tag{A.10}$$

A.2 Methodology for the Laplace inversions

The purpose of this section is to describe a methodology that is often used to perform some inverse Laplace transform. As we mentioned in the introduction of this chapter, most of the functions that we have to inverse have the same structure. The main steps of their inversion is therefore the same.

Almost all the inversions that we have to perform can be written as

$$\mathscr{L}^{-1}\left(\hat{N}(p)\hat{M}(\alpha_s)\right),$$

with

$$\alpha_s = \sqrt{1+\left(\frac{p}{|q|\,c_s}\right)^2},$$

and where $\hat{M}$ is a function for which we know an explicit expression. On the other hand, $\hat{N}$ is either a constant or an unknown function.

We always proceed in four steps :

- **first step**
  Computation of $M(t)$, the inverse Laplace transform of $\hat{M}(s)$.

- **second step**
  Using the result of the first step, computation of $\mathscr{L}^{-1}\left(\hat{M}(\sqrt{1+s^2})\right)$. To perform this we need one of the two expressions of the next property that we show without demonstration.

Property 1 *If*

$$\mathscr{L}^{-1}\left(\hat{g}(s)\right) = g(T),$$

then

$$\mathscr{L}^{-1}\left(\hat{g}\left(\sqrt{1+s^2}\right)\right) = g(T) - \int_0^T g\left(\sqrt{T^2-u^2}\right) J_1(u)\ du, \qquad \text{(A.11)}$$

where J_1 denotes the Bessel function of the first kind and of order 1. Sometimes, it is more convenient to express this in another way, with a change of variable $v = \sqrt{T^2-u^2}$. It gives

$$\mathscr{L}^{-1}\left(\hat{g}\left(\sqrt{1+s^2}\right)\right) = g(T) - \int_0^T v\ \ g(v)\frac{J_1\left(\sqrt{T^2-v^2}\right)}{\sqrt{T^2-v^2}}\ dv. \qquad \text{(A.12)}$$

- **third step**
  Replacement of s by $\frac{p}{|q|c_s}$ in order to replace $\sqrt{1+s^2}$ by α_s. To perform this, we use the next property.

Property 2 *If*

$$\mathscr{L}^{-1}\left(\hat{g}(s)\right) = g(T),$$

then

$$\mathscr{L}^{-1}\left(\hat{g}(as)\right) = \frac{T}{a} g\left(\frac{1}{a}\right). \qquad \text{(A.13)}$$

So, using the results of the second step, we know

$$\mathscr{L}^{-1}\left(\hat{M}(\alpha_s)\right).$$

- **fourth step**
  If $\hat{N}$ is not a constant, convolution of its inverse Laplace transform with the result of the third step.

$$\mathscr{L}^{-1}\left(\hat{N}(p)\hat{M}(\alpha_s)\right) = \mathscr{L}^{-1}\left(\hat{N}(p)\right) \otimes \mathscr{L}^{-1}\left(\hat{M}(\alpha_s)\right),$$

where

$$\left(f \otimes g\right)(t) = \int_{-\infty}^{t} f(t-t')g(t')dt'.$$

A.3 Laplace inversion for the analytical solution

Our purpose is here to compute the inverse Laplace transform of

$$\mathscr{L}^{-1}\left(\frac{1}{\mu^-\alpha_s\sinh(\alpha_s a)+\mu^+\alpha_s\cosh(\alpha_s a)}\right), \tag{A.14}$$

that appears in (3.1). Note that $a=|q|\,H\geq 0$. Since the Laplace variable p only appears inside α_s, we use the methodology described in A.2.

- **first step**

  We begin by the inverse Laplace transform of

$$\hat{F}_1(s)=\frac{1}{\mu^- s\sinh(as)+\mu^+ s\cosh(as)}. \tag{A.15}$$

  This expression can be rewritten as

$$\hat{F}(s)=\frac{1}{s\left(\frac{\mu^-+\mu^+}{2}e^{as}+\frac{\mu^--\mu^+}{2}e^{-as}\right)}.$$

  So, if

$$c=\frac{\mu^-+\mu^+}{2},\qquad d=\frac{\mu^--\mu^+}{2},$$

  since the shear module μ is non-negative, we have always $|d|\leq|c|$. We can then use (A.6) with $m=0$, and get

$$\mathscr{L}^{-1}\left(\hat{F}(s)\right)=2\sum_{n=0}^{\infty}\frac{(\mu^+-\mu^-)^n}{(\mu^++\mu^-)^{n+1}}H\left(t-(2n+1)a\right). \tag{A.16}$$

- **second step**

  Replacing s in (A.15) by $\sqrt{1+s^2}$ and using (A.11) to adapt the result of the first step, we get

$$\mathscr{L}^{-1}\left(\hat{F}\left(\sqrt{1+s^2}\right)\right)=2\sum_{n=0}^{\infty}\frac{(\mu^+-\mu^-)^n}{(\mu^++\mu^-)^{n+1}}I_n(t),$$

  with

$$I_n(t)=H\left(t-(2n+1)a\right)-\int_0^t H\left(\sqrt{T^2-u^2}-(2n+1)a\right)J_1(v)dv.$$

  Using (A.10) on this integration yields

$$I_n(t)=H\left(t-(2n+1)a\right)J_0\left(\sqrt{t^2-(2n+1)^2a^2}\right).$$

  So, we have

$$\mathscr{L}^{-1}\left(\hat{F}\left(\sqrt{1+s^2}\right)\right)=2\sum_{n=0}^{\infty}\frac{(\mu^+-\mu^-)^n}{(\mu^++\mu^-)^{n+1}}H\left(t-(2n+1)k\right)J_0\left(\sqrt{t^2-(2n+1)^2k^2}\right).$$

- **third step**
Replacing s by $\frac{p}{|q|c_s}$, and using (A.13), we get

$$\mathscr{L}^{-1}\left(\hat{F}(\alpha_s)\right) = 2\sum_{n=0}^{\infty} qc_s \frac{(\mu^+ - \mu^-)^n}{(\mu^+ + \mu^-)^{n+1}} J_0\left(\sqrt{(|q|\, c_s t)^2 - (2n+1)^2 a^2}\right),$$

which is used to transform (3.1) into (3.2).

A.4 Laplace inversions for two-convolution approach

The purpose of this section is to perform the Laplace inversion of two terms of (2.10)

$$\hat{T}^+ = \underbrace{-\mu^+ |q|\, \alpha_s^+ \tanh(a\alpha_s^+)\hat{U}^+}_{\#1} + \underbrace{\frac{1}{\cosh(a\alpha_s^+)}\hat{T}^H}_{\#2}. \tag{A.17}$$

Since the Laplace variable p appears only inside α_s, we use the methodology described in (A.2) for both terms.

A.4.1 term #1: $-\mu^+ |q|\, \alpha_s^+ \tanh(a\alpha_s^+)\hat{U}^+$

- **first step**
Let us first compute

$$\mathscr{L}^{-1}\left(s\tanh(as)\right) = \mathscr{L}^{-1}\left(\tanh(as)\right)'.$$

If we rewrite $s\tanh(as)$ as

$$s\tanh(as) = s\frac{e^{as}}{e^{as}+e^{as}} - s\frac{e^{-as}}{e^{as}+e^{as}},$$

we can use (A.7) on each term, with $c = d = 1$, $k = a$ and $m = \mp a$. This gives

$$\mathscr{L}^{-1}\left(\tanh(as)\right) = \sum_{n=0}^{\infty}(-1)^n\delta'\left(t-2na\right) - \sum_{n=0}^{\infty}(-1)^n\delta'\left(t-(2n+2)a\right).$$

Finally, by changing the index of the second sum, this expression can be rewritten as

$$\mathscr{L}^{-1}\left(s\tanh(as)\right) = \delta'(t) + 2\sum_{n=0}^{\infty}(-1)^n\delta'\left(t-2na\right).$$

- **second step**
Applying (A.12) to the result of the first step yields

$$\begin{aligned}\mathscr{L}^{-1}\left(\sqrt{1+s^2}\tanh(a\sqrt{1+s^2})\right) = &\ \delta'(t) - \textstyle\int_0^t v\delta'(v)\frac{J_1\left(\sqrt{T^2-v^2}\right)}{\sqrt{T^2-v^2}}dv \\ + &\ 2\textstyle\sum_{n=0}^{\infty}(-1)^n\delta'\left(t-2na\right) \\ - &\ \textstyle\int_0^t 2\sum_{n=0}^{\infty}(-1)^n v\delta'\left(v-2na\right)\frac{J_1\left(\sqrt{T^2-v^2}\right)}{\sqrt{T^2-v^2}}dv.\end{aligned}$$

Using (A.9) to compute these integrals yields

$$\begin{aligned}
\mathscr{L}^{-1}\left(\sqrt{1+s^2}\tanh(a\sqrt{1+s^2})\right) = \;& \delta'(t) - C_\infty(t) \\
& +2\sum_{n=0}^{\infty}(-1)^n\delta'\left(t-2na\right) \\
& -2na\sum_{n=0}^{\infty}(-1)^n\delta\left(t-2na\right) \\
& +C_{H2}(t),
\end{aligned} \tag{A.18}$$

where

$$C_{H2}(t) = 2\sum_{n=1}^{\infty}(-1)^n\left(\frac{J_1\left(\sqrt{T^2-4n^2a^2}\right)}{\sqrt{T^2-4n^2a^2}} + 4a^2\frac{J_2\left(\sqrt{T^2-4n^2a^2}\right)}{T^2-4n^2a^2}\right),$$

and

$$C_\infty(T) = \frac{J_1(T)}{T}.$$

- **third step**
  Replacing s by $\frac{p}{|q|c_s^+}$ in (A.18) yields

$$\begin{aligned}
\mathscr{L}^{-1}\left(\alpha_s^+\tanh(a\alpha_s^+)\right) = \;& |q|\,c_s^+\delta'(|q|\,c_s^+t) - C_\infty(|q|\,c_s^+t) \\
& +2\sum_{n=0}^{\infty}(-1)^n\,|q|\,c_s^+\delta'\left(t-2na\right) \\
& -2\sum_{n=0}^{\infty}(-1)^n na\,|q|\,c_s^+\delta\left(t-2na\right) \\
& +C_{H2}(|q|\,c_s^+t).
\end{aligned}$$

- **fourth step**
  Finally we perform the convolution, and obtain

$$\mathscr{L}^{-1}\left(-\mu^+\,|q|\,\alpha_s^+\tanh(a\alpha_s^+)\hat{U}^+\right) =$$

$$\begin{aligned}
- & \;\frac{\mu^+}{c_s^+}\dot{U}^+(t) \\
- & \;2\frac{\mu^+}{c_s^+}\sum_{n=0}^{\infty}(-1)^n\dot{U}^+\left(t-2n\frac{H}{c_s^+}\right) \\
+ & \;2\mu^+\,|q|\sum_{n=1}^{\infty}(-1)^n naU^+\left(t-2n\frac{H}{c_s^+}\right) \\
- & \;\mu\,|q|\int_0^t\left\{C_\infty(|q|\,c_s^+t') + C_{H2}(|q|\,c_s^+t')\right\}U^+(t-t')\,|q|\,c_s^+dt'
\end{aligned}$$

A.4.2 term #2 $\frac{1}{\cosh(a\alpha_s^+)}\hat{T}^H$

- **first step**
  Let us start by the inversion of

$$\frac{1}{\cosh as} = \frac{2}{e^{as}+e^{-as}}.$$

Using (A.5) with $c = d = 1$, $m = 0$ and $k = a$, we get

$$\mathscr{L}^{-1}\left(\frac{1}{\cosh as}\right) = \sum_{n=0}^{\infty}(-1)^n\delta(t-(2n+1)a).$$

- **second step**
  Applying (A.12) to the previous result yields

$$\mathscr{L}^{-1}\left(\frac{1}{\cosh\left(a\sqrt{1+s^2}\right)}\right) = 2\sum_{n=0}^{\infty}(-1)^n\delta\left(t-(2n+1)a\right) - 2\sum_{n=0}^{\infty}(-1)^n I_n, \tag{A.19}$$

  where

$$I_n = \int_0^t v\delta\left(v-(2n+1)a\right)\frac{J_1\left(\sqrt{T^2-v^2}\right)}{\sqrt{T^2-v^2}}dv.$$

  Computing this integral, we can rewrite (A.19) as

$$\mathscr{L}^{-1}\left(\frac{1}{\cosh\left(\sqrt{1+s^2}\right)}\right) = 2\sum_{n=0}^{\infty}(-1)^n\delta\left(t-(2n+1)a\right) - E_2(t)$$

  where

$$E_2(T) = 2\sum_{n=0}^{\infty}(-1)^n(2n+1)a\frac{J_1\left(\sqrt{T^2-(2n+1)^2a^2}\right)}{\sqrt{T^2-(2n+1)^2a^2}}. \tag{A.20}$$

- **third step**
  Replacing s by $\frac{p}{|q|c_s^+}$, and using (A.13), we get

$$\begin{aligned}\mathscr{L}^{-1}\left(\frac{1}{\cosh\left(a\alpha_s^+\right)}\right) = & \quad 2\,|q|\,c_s^+\textstyle\sum_{n=0}^{\infty}(-1)^n\delta\left(|q|\,c_s^+t-(2n+1)a\right)\\ - & \quad 2\,|q|\,c_s^+E_2\left(|q|\,c_s^+t\right).\end{aligned}$$

- **fourth step**
  Performing the convolution with T^H yields

$$\begin{aligned}\mathscr{L}^{-1}\left(\frac{\hat{T}^H}{\cosh a\alpha_s^+}\right) = & \quad 2\textstyle\sum_{n=0}^{\infty}(-1)^nT^H\left(t-(2n+1)\frac{H}{c_s^+}\right)\\ - & \quad \textstyle\int_0^t E_2\left(|q|\,c_s^+t'\right)T^H\left(t-t'\right)|q|\,c_s^+dt'.\end{aligned}$$

A.5 Laplace inversion for three-convolution approach

The purpose of this section is to perform the Laplace inversion of (2.13). As in the previous section, we work term by term,

$$\hat{T}^+ + \underbrace{e^{-2\alpha_s^+a}\hat{T}^+}_{\#1} = \underbrace{-\mu^+\,|q|\,\alpha_s^+e^{-2\alpha_s^+a}}_{\#2} + \underbrace{+\mu^+\,|q|\,\alpha_s^+\hat{U}^+}_{\#3} + \underbrace{2e^{-\alpha_s^+a}\hat{T}^H}_{\#4}.$$

A.5.1 term #1 $e^{-2\alpha_s^+ a}\hat{T}^+$

Since the Laplace variable p appears only inside α_s, we can use the methodology described in A.2.

- **first step**
  Let us remind that
  $$\mathscr{L}^{-1}\left(e^{-2as}\right) = \delta(T-2a).$$

- **second step**
  So, by (A.12), we have
  $$\mathscr{L}^{-1}\left(e^{-2a\sqrt{1+s^2}}\right) = \delta(T-2a) - \int_0^T v\delta(v-2a)\frac{J_1\left(\sqrt{T^2-v^2}\right)}{\sqrt{T^2-v^2}}dv.$$
  Computing this integral yields
  $$\mathscr{L}^{-1}\left(e^{-2a\sqrt{1+s^2}}\right) = \delta\left(T-2a\right) - D_3(T),$$
  where D_3 is defined by
  $$D_3(T) = 2a\frac{J_1\left(\sqrt{T^2-4a^2}\right)}{\sqrt{T^2-4a^2}}.$$

- **third step**
  Replacing s by $\frac{p}{|q|c_s^+}$ and using (A.13), we can get
  $$\mathscr{L}^{-1}\left(e^{-2a\alpha_s}\right) = |q|\,c_s^+\delta(|q|\,c_s^+t) - D_3\left(|q|\,c_s^+t\right)|q|\,c_s^+. \tag{A.21}$$

- **fourth step**
  The convolution of (A.21) with T gives
  $$\mathscr{L}^{-1}\left(e^{-2a\alpha_s}\hat{T}\right) = T\left(t-2\frac{H}{c_s}\right) - \int_0^t D_3\left(|q|\,c_s t'\right)T\left(t-t'\right)|q|\,c_s dt'. \tag{A.22}$$

A.5.2 term #2 $\mu^+\,|q|\,\alpha^s e^{-2a\alpha_s}\hat{U}^+$

Once more, we are going to use the methodology described in A.2.

- **first step**
  Let us remind that
  $$\mathscr{L}^{-1}\left(se^{-2as}\right) = \delta'(T-2a).$$

- **second step**
Applying (A.12) to the results of the first step, we get

$$\mathscr{L}^{-1}\left(\sqrt{1+s^2}e^{-2a\sqrt{1+s^2}}\right) = \delta'(T-2a) - \int_0^t v\delta'(v)\frac{J_1\left(\sqrt{T^2-v^2}\right)}{\sqrt{T^2-v^2}}dv.$$

To compute the integral appearing in this expression, we can use (A.9) with $k=2a$. This yields

$$\mathscr{L}^{-1}\left(\sqrt{1+s^2}e^{-2a\sqrt{1+s^2}}\right) = \delta'(T-2a) - a\delta(T-2a) + C_{H3}(T),$$

where C_{H3} is defined by

$$C_{H3}(T) = \frac{J_1\sqrt{T^2-4a^2}}{\sqrt{T^2-4a^2}} + 4a^2\frac{\sqrt{T^2-4a^2}}{T^2-4a^2}.$$

- **third step**
Replacing s by $\frac{p}{|q|c_s^+}$ and using (A.13), we get

$$\begin{aligned}\mathscr{L}^{-1}\left(e^{-2a\alpha_s^+}\right) = & \ |q|\,c_s^+\delta'\left(|q|\,c_s^+t-2a\right) - a\,|q|\,c_s^+\delta\left(|q|\,c_s^+t-2a\right)\\ & +C_{H3}\left(|q|\,c_s^+t\right)|q|\,c_s^+.\end{aligned} \tag{A.23}$$

- **fourth step**
The laplace transform of the term #2 can now be computed convoluting U with (A.23). This yields

$$\begin{aligned}\mathscr{L}^{-1}\left(\mu^+\,|q|\,\alpha_s e^{-2a\alpha_s}\hat{U}^+\right) = & \ \tfrac{\mu^+}{c_s^+}\dot{U}\left(t-\tfrac{2H}{c_s^+}\right) - \mu^+\,|q|\,aU\left(t-\tfrac{2H}{c_s^+}\right)\\ & +\mu^+\,|q|\int_{\frac{2H}{c_s^+}}^t\left(C_{H3}\left(|q|\,c_s^+t'\right)\right)U(t-t')\,|q|\,c_s^+dt'.\end{aligned}$$

A.5.3 term #3 $\mu^+\,|q|\,\alpha_s^+\hat{U}^+$

This inversion is performed exactly as that performed in 2.2: Extracting the velocity of this expression gives

$$\mu^+\,|q|\,\alpha_s^+\hat{U}^+ = \frac{\mu^+}{c_s^+}p\hat{U}^+ + \mu^+\,|q|\left(\alpha_s^+ - \frac{p}{|q|\,c_s^+}\right)\hat{U}^+.$$

Since

$$\mathscr{L}^{-1}\left(\sqrt{1+s^2}-s\right) = \frac{J_1(T)}{T} \doteq C_\infty(T),$$

we get

$$\mathscr{L}^{-1}\left(\mu^+\,|q|\,\alpha_s^+\hat{U}^+\right) = \frac{\mu^+}{c_s^+}\dot{U}(t) + \mu^+\,|q|\int_0^t C_\infty\left(|q|\,c_s^+t'\right)U(t-t')\,|q|\,c_s dt'.$$

Note that we could have performed this inversion following our four steps scheme.

A.5.4 term #4 $2e^{-\alpha_s^+ a}\hat{T}^H$

We can rewrite this inversion as

$$\mathscr{L}^{-1}\left(2e^{-\alpha_s^+ a}\hat{T}^H\right) = 2\mathscr{L}^{-1}\left(e^{-\alpha_s^+ 2\frac{a}{2}}\hat{T}^H\right),$$

which is exactly the expression of the term #1. Using then (A.22), we get

$$\mathscr{L}^{-1}\left(2e^{-\alpha_s^+ a}\hat{T}^H\right) = 2T^H\left(t - \frac{H}{c_s}\right) - \int_{\frac{H}{c_s^+}}^{t} E_3\left(|q|\, c_s^+ t'\right) T^H(t-t')\, |q|\, c_s^+ dt',$$

where the convolution kernel E_3 is defined by

$$E_3(T) \doteq 2a\frac{J_1\left(\sqrt{T^2 - a^2}\right)}{\sqrt{T^2 - a^2}}$$

A.6 Laplace inversion for the external boundary

The purpose of this section is to perform the Laplace inversion of (5.1). We work term by term,

$$\underset{\#1}{|q|\,\alpha_s^+\hat{U}^H} + \underset{\#2}{|q|\,\alpha_s^+\hat{U}^H e^{-2a\alpha_s^+}} = \underset{\#3}{2q\alpha_s^+\hat{U}^+ e^{-a\alpha_s^+}} + \frac{1}{\mu^+}\hat{T}^H - \underset{\#4}{\frac{1}{\mu^+}\hat{T}^H e^{-2a\alpha_s^+}}.$$

A.6.1 term #1 $|q|\,\alpha_s^+\hat{U}^H$

This term is totally similar to A.5.3. Reusing this results gives us

$$\mathscr{L}^{-1}\left(q\alpha_s^+\hat{U}^H\right) = \frac{\dot{U}^H(t)}{c_s^+} + |q| + \int_0^t C_\infty\left(|q|\, c_s^+ t'\right) U^H(t-t')\, |q|\, c_s^+ dt'$$

A.6.2 term #2 $|q|\,\alpha_s^+\hat{U}^H e^{-2a\alpha_s^+}$

This term is totally similar to A.5.2. We have thus

$$\begin{aligned}\mathscr{L}^{-1}\left(|q|\,\alpha_s^+\hat{U}^H e^{-2a\alpha_s^+}\right) = \;& \tfrac{1}{c_s^+}\dot{U}^H\left(t - \tfrac{2H}{c_s^+}\right) - |q|\, aU^H\left(t - \tfrac{2H}{c_s^+}\right)\\ & + |q| \textstyle\int_{\frac{2H}{c_s^+}}^{t}\left(C_{H3}\left(|q|\, c_s^+ t'\right)\right) U^H(t-t')\, |q|\, c_s^+ dt'.\end{aligned}$$

A.6.3 term #3 $2q\alpha_s^+\hat{U}^+ e^{-a\alpha_s^+}$

This term is similar to A.5.2. We can thus use this result with $\frac{a}{2}$ instead of a, and this yields

$$\begin{aligned}\mathscr{L}^{-1}\left(2\,|q|\,\alpha_s\hat{U}^+ e^{-a\alpha_s}\right) = \;& \tfrac{2}{c_s^+}\dot{U}^+\left(t - \tfrac{H}{c_s^+}\right) - |q|\, aU^H\left(t - \tfrac{H}{c_s^+}\right)\\ & +2\,|q| \textstyle\int_{\frac{H}{c_s^+}}^{t}\left(C'_{H3}\left(|q|\, c_s^+ t'\right)\right) U^H(t-t')\, |q|\, c_s^+ dt',\end{aligned}$$

where the convolution kernel C'_{H3} is defined by

$$C'_{H3}(T) = \frac{J_1\sqrt{T^2-a^2}}{\sqrt{T^2-a^2}} + a^2\frac{\sqrt{T^2-a^2}}{T^2-a^2}.$$

A.6.4 term #4 $\frac{1}{\mu^+}\hat{T}^H e^{-2a\alpha_s^+}$

This term is similar to A.5.1. So, we have

$$\mathscr{L}^{-1}\left(\frac{1}{\mu^+}e^{-2a\alpha_s}\hat{T}^H\right) = \frac{1}{\mu^+}T^H\left(t-2\frac{H}{c_s^+}\right) - \frac{1}{\mu^+}\int_0^t D_3\left(|q|\,c_s^+t'\right)T^H\left(t-t'\right)|q|\,c_s^+dt'. \tag{A.24}$$

A.7 Laplace inversion for the analytical solution for the external boundary

Our purpose is here to compute the inverse Laplace transform of

$$p\hat{U}^H\cosh(a\alpha_s) = pU + \frac{\tau_0^H}{\mu^+q\alpha_s}\sinh(a\alpha_s),$$

with

$$p\hat{U} = \frac{\tau_0^H}{q\mu^-\alpha_s\sinh(\alpha_s a) + q\mu^+\alpha_s\cosh(\alpha_s a)}.$$

This can be expressed as

$$p\hat{U}^H = \frac{\tau_0^H}{q\mu^+\alpha_s\cosh(a\alpha_s)}\left(\sinh(a\alpha_s) + \frac{1}{\frac{\mu^-}{\mu^+}\cosh(a\alpha_s)+\sinh(a\alpha_s)}\right),$$

or, since $\sinh^2(X)+1=\cosh^2(X)$,

$$p\hat{U}^H = \frac{\tau_0^H}{q\mu^+\alpha_s}\left(\frac{\frac{\mu^-}{\mu^+}\sinh(a\alpha_s)+\cosh(a\alpha_s)}{\frac{\mu^-}{\mu^+}\cosh(a\alpha_s)+\sinh(a\alpha_s)}\right).$$

The inversion of the left member of this relation is trivial $\mathscr{L}^{-1}\left(p\hat{U}^H\right) = \dot{U}^H$. In the right member, the Laplace variable p only appears in α_s. We can thus use the methodology described in A.2.

- **firth step**
  We can rewrite

$$\mathscr{L}^{-1}\left(\tilde{U}_1^H(s)\right) = \mathscr{L}^{-1}\left(\frac{1}{s}\left(\frac{\frac{\mu^-}{\mu^+}\sinh(as)+\cosh(as)}{\frac{\mu^-}{\mu^+}\cosh(as)+\sinh(as)}\right)\right)$$

as

$$\mathscr{L}^{-1}\left(\tilde{U}_1^H(s)\right) = \mathscr{L}^{-1}\left(\frac{1}{s}\frac{e^{as}}{e^{as}-\Delta_\mu e^{-as}}\right) + \Delta_\mu \mathscr{L}^{-1}\left(\frac{1}{s}\frac{e^{as}}{e^{as}-\Delta_\mu e^{-as}}\right), \tag{A.25}$$

where

$$\Delta_\mu = \left(\frac{\mu^+ - \mu^-}{\mu^+ + \mu^-}\right).$$

Using (A.6) on these two inversions leads to

$$\mathscr{L}^{-1}\left(\tilde{U}_1^H(s)\right) = H(t) + \sum_{n=1}^{\infty} \Delta_\mu^n H\left(t - 2na\right) + \Delta_\mu^n \sum_{n=0}^{\infty} \Delta_\mu^n H\left(t - 2(n+1)a\right), \tag{A.26}$$

or, changing the index of the second sum,

$$\tilde{U}_1^H = H(t) + 2\sum_{n=1}^{\infty} \Delta_\mu^n H\left(t - 2na\right). \tag{A.27}$$

- **second step**
  Applying (A.11) to the results of the first step yields

$$\begin{aligned}\mathscr{L}^{-1}\left(\tilde{U}_1^H\left(\sqrt{1+s^2}\right)\right) = \quad & H(t) + 2\textstyle\sum_{n=1}^{\infty} \Delta_\mu^n H\left(t-2na\right) \\ - \quad & \textstyle\int_0^t H\left(\sqrt{t^2-u^2}\right) J_1(u)du \\ - \quad & 2\textstyle\sum_{n=1}^{\infty} \Delta_\mu^n \int_0^t H\left(\sqrt{t^2-u^2}-2na\right) J_1(u)du.\end{aligned} \tag{A.28}$$

  Using (A.10) to perform the integrations, this becomes

$$\mathscr{L}^{-1}\left(\tilde{U}_1^H\left(\sqrt{1+s^2}\right)\right) = J_0(t) + 2\sum_{n=1}^{\infty} \Delta_\mu^n H\left(t-2na\right) J_0\left(\sqrt{t^2-4n^2a^2}\right). \tag{A.29}$$

- **third step**
  Replacing s by $\frac{p}{qc_s}$, and using (A.13) yields

$$\begin{aligned}\mathscr{L}^{-1}\left(\tilde{U}_1^H\left(\sqrt{1+\left(\frac{p}{qc_s}\right)^2}\right)\right) = \quad & qc_s J_0(qc_s t) \\ + \quad & 2\textstyle\sum_{n=1}^{\infty} \Delta_\mu^n H\left(t-2na\right) qc_s J_0\left(\sqrt{\left(qc_s t\right)^2 - 4n^2a^2}\right),\end{aligned} \tag{A.30}$$

  and finally

$$\dot{U}^H(t) = \frac{\tau_0^H c_s}{\mu^+}\left(J_0\left(qc_s t\right) + 2\sum_{n=1}^{\infty} (\Delta_\mu)^n J_0\left(\sqrt{\left(qc_s t\right)^2 - 4na^2}\right) H\left(qc_s t - 2na\right)\right). \tag{A.31}$$

Appendix B

Kernel asymptotic analysis

The purpose of this appendix is to analyze the asymptotic behavior of some kernels involved in 2.14, in order to understand the origin off the instabilities and to select an appropriate filter (see Chapter 4).

B.1 asymptotic behavior and convergence of terms #1 and #3

In this section, we show that, for a fixed function $\tilde{U}$, and $z > 2$,

$$I = \lim_{a\to\infty} \int_2^z \frac{J_2\left(a\sqrt{z'^2-4}\right)}{z^2-4} 4a^2\tilde{U}(z-z')dz' = a^2\tilde{U}(z-2). \tag{B.1}$$

Our purpose is not here to give a complete and rigorous demonstration, but to convince the reader that this relation is true. Note that this result was confirmed numerically.

Let us rewrite the first term of (B.1) using $x = \sqrt{z^2-4}$,

$$I = \lim_{a\to\infty} \int_0^{x(z)} \frac{J_2(ax')}{x'\sqrt{x'^2+4}} 4a^2U(x-x')dx',$$

where $U(x(z)) = \tilde{U}(z)$. Since J_2 decays to 0, the inner part of this integral only takes significant values on an interval $[0, M(a)]$ which size decreases to 0 when $a \to \infty$. We can thus assume that for large values of a,

$$\int_0^{x(z)} \frac{J_2(ax')}{x'\sqrt{x'^2+4}} 4a^2U(x-x')dx' \approx \int_0^{M(a)} \frac{J_2(ax')}{x'\sqrt{x'^2+4}} 4a^2U(x-x')dx',$$

where $lim_{a\to\infty} M(a) = 0$. Since U is supposed fixed (i.e. independent of a), we can assume that for large values of a, its value is constant on $[x - M(a), x]$,

$$I = \lim_{a\to\infty} \int_0^{M(a)} \frac{J_2(ax')}{x'\sqrt{x'^2+4}} 4a^2U(x)dx'.$$

Since $M(a) \to 0$, $\sqrt{x'^2+4} \approx 2$ on $[0, M(a)]$, we have thus

$$I = \lim_{a\to\infty} \int_0^{M(a)} \frac{J_2(ax')}{x'} 2a^2 U(x) dx'.$$

The change of variable $y = ax$ leads to

$$I = 2a^2 U(x) \lim_{a\to\infty} \int_0^{aM(a)} \frac{J_2(y')}{y'} dy'.$$

As mentioned before, $\frac{J_2(y')}{y'}$ only takes significant values on $[0, aM(a)]$, we can thus rewrite this last relation as

$$I = 2a^2 U(x) \lim_{a\to\infty} \int_0^{aM(a)} \frac{J_2(y')}{y'} dy' \approx 2a^2 U(x) \lim_{a\to\infty} \int_0^{\infty} \frac{J_2(y')}{y'} dy'.$$

Finally, using

$$\int_0^{\infty} \frac{J_2(y)}{y} dy = \frac{1}{2},$$

we get

$$I = aU(x) = a\tilde{U}(z-2),$$

which was the relation we wanted to show.

B.2 asymptotic behavior of term #2

The purpose of this section is to show that for a fixed function $\tilde{U}$, and $z > 2$,

$$I = \lim_{a\to\infty} \int_2^z \frac{J_1\left(a\sqrt{z'^2-4}\right)}{\sqrt{z^2-4}} a\tilde{U}(z-z')dz' = \tilde{U}(z-2). \tag{B.2}$$

As in Section B.1, we do not intend to give here a complete and rigorous proof, but just to convince the reader that this relation is true. Note that this result was confirmed numerically.

Let us rewrite the first term of (B.2) using $x = \sqrt{z^2-4}$,

$$I = \lim_{a\to\infty} \int_0^{x(z)} \frac{J_1(ax')}{\sqrt{x'^2+4}} aU(x-x')dx',$$

where $U(x(z)) = \tilde{U}(z)$. Since J_1 decays to 0, the inner part of this integral only takes significant values on an interval $[0, M(a)]$, which size decay to 0 when $a \to \infty$. We can thus assume that for large values of a,

$$\int_0^{x(z)} \frac{J_1(ax')}{\sqrt{x'^2+4}} aU(x-x')dx' \approx \int_0^{M(a)} \frac{J_1(ax')}{\sqrt{x'^2+4}} aU(x-x')dx',$$

where $lim_{a\to\infty} M(a) = 0$. Since U is supposed fixed (i.e. independent of a), we can assume that for large values of a, its value is constant on $[x - M(a), x]$,

$$I = \lim_{a\to\infty} \int_0^{M(a)} \frac{J_1(ax')}{\sqrt{x'^2+4}} aU(x)dx'.$$

For large values of a, $M(a) \to 0$. On $[0, M(a)]$, we have thus $\sqrt{x'^2+4} \approx 2$, and

$$I = \frac{1}{2} \lim_{a\to\infty} \int_0^{M(a)} J_1(ax')aU(x)dx'.$$

As mentioned before, $J_2(ax)$ only takes significant values on $[0, M(a)]$. We can thus rewrite this last relation as

$$I = \frac{1}{2}U(x) \lim_{a\to\infty} \int_0^{\infty} J_1(ax')adx' = \frac{1}{2}U(x) = \frac{1}{2}\tilde{U}(z-2).$$

Appendix C

Analytic solution for constant loading and a perfect interface

The purpose of this appendix is to derive an analytic expression for the evolution of the traction stress τ and the velocity of the interface in the case of a perfect interface and an uniform loading. The problems are thus reduced to 1-D problems that can be formulated using recurrence equations. Section C.1 treats the case of a shear stress applied along the film surface, while Section C.2 treats the case of a shear wave coming from the substrate.

C.1 Shear stress applied along the surface of the thin film

As said before, we consider here the evolution of the traction stress and the velocity in the case of a perfect interface between the substrate and a thin film on surface of which a shear stress $\tau_0^H H(t)$ is applied. Since nothing depends on x, (2.8) and (2.14) become

$$\left\{ \begin{array}{ll} \frac{\mu^+}{c_s^+}\dot{u}^+(t) + \tau^+(t) & = \frac{\mu^+}{c_s^+}\dot{u}^+\left(t - 2\frac{H}{c_s^+}\right) - \tau^+\left(t - 2\frac{H}{c_s^+}\right) + 2\tau^H\left(t - \frac{H}{c_s^+}\right) \\ \frac{\mu^-}{c_s^-}\dot{u}^-(t) - \tau^-(t) & = 0. \end{array} \right. \tag{C.1}$$

Using the continuity conditions of the perfect interface $\dot{u}^+ = \dot{u}^- = \dot{u}$, $\tau^+ = \tau^- = \tau$, and assuming $t \geq 0$, we can reformulate (C.1) as a recurrence,

$$\left\{ \begin{array}{ll} \frac{\mu^+}{c_s^+}\dot{u}(n+1) + \tau(n+1) & = \frac{\mu^+}{c_s^+}\dot{u}\,(n) - \tau\,(n) + 2\tau_0^H \\ \frac{\mu^-}{c_s^-}\dot{u}(n) - \tau(n) & = 0, \end{array} \right. \tag{C.2}$$

where $n = \lfloor \frac{c_s^+ t + H}{2H} \rfloor \geq 0$ represents the number of reflections of the shear wave off the interface. From this discrete system, we can isolate two independent discrete equations,

$$\left\{ \begin{array}{ll} \left(\frac{\mu^+}{c_s^+} + \frac{\mu^-}{c_s^-} \right) \dot{u}(n+1) & = \left(\frac{\mu^+}{c_s^+} - \frac{\mu^-}{c_s^-} \right) \dot{u}(n) + 2\tau_0^H \\ \left(\frac{\mu^+}{c_s^+} + \frac{\mu^-}{c_s^-} \right) \tau(n+1) & = \left(\frac{\mu^+}{c_s^+} - \frac{\mu^-}{c_s^-} \right) \tau(n) + 2\frac{\mu^-}{c_s^-}\tau_0^H \end{array} \right.$$

The general solution for the traction stress is the sum of the homogenous solution and a particular solution ($\tau = \tau^H$),

$$\tau(n) = \tau^H + Ak^n,$$

where A has to be determined by an initial condition, and k is defined by

$$k = \frac{\frac{\mu^+}{\mu^-} - \frac{c_s^+}{c_s^-}}{\frac{\mu^+}{\mu^-} + \frac{c_s^+}{c_s^-}}. \tag{C.3}$$

Since $\tau(0) = 0$, we have

$$\tau(n) = \tau_0^H \left(1 - k^n\right).$$

The velocity is obtained by a similar computation, or using the second equation of (C.2),

$$\dot{u}(n) = \frac{c_s^-}{\mu^-}\tau_0^H \left(1 - k^n\right).$$

C.2 Shear wave coming from the substrate

We consider here the evolution of the traction stress and the velocity in the case of a perfect interface. Unlike in section C.1, there is no loading on the thin film, but a plane shear wave of amplitude τ_0^B is coming from the substrate. We use thus the modified formulation explained in section 7.3. Since nothing depends on x, (2.14) and (7.3) give us

$$\left\{ \begin{array}{ll} \frac{\mu^+}{c_s^+}\dot{u}^+(t) + \tau^+(t) & = \frac{\mu^+}{c_s^+}\dot{u}^+ \left(t - 2\frac{H}{c_s^+}\right) - \tau^+ \left(t - 2\frac{H}{c_s^+}\right) \\ \frac{\mu^-}{c_s^-}\dot{u}^-(t) - \tau^-(t) & = -2\tau_0^B H(t). \end{array} \right. \tag{C.4}$$

Using the continuity conditions of the perfect interface $\dot{u}^+ = \dot{u}^- = \dot{u}$, $\tau^+ = \tau^- = \tau$ and eliminating the velocity yields the recurrence relation

$$2\frac{\mu^+}{c_s^+}\tau_0^B \left(H(n+1) - H(n)\right) = \tau(n+1) \left(\frac{\mu^+}{c_s^+} + \frac{\mu^-}{c_s^-} \right) - \tau(n) \left(\frac{\mu^+}{c_s^+} - \frac{\mu^-}{c_s^-} \right). \tag{C.5}$$

where $n = \lfloor \frac{c_s^+ t}{2H} \rfloor$ represents the numbers of reflection of the shear wave off the interface. Note that, unlike in section C.1, we have to solve this equation for

$n \geq -1$ since the initial condition is known for $n = -1$. The homogeneous solution of (C.5) is

$$\tau(n) = A \left(\frac{\frac{\mu^+}{c_s^+} - \frac{\mu^-}{c_s^-}}{\frac{\mu^+}{c_s^+} + \frac{\mu^-}{c_s^-}} \right)^{n+1}.$$

One can verify that a particular solution to C.5 is given by

$$\tau(n) = \begin{array}{ll} -\frac{2\tau_0^B \frac{\mu^+}{c_s^+}}{\frac{\mu^+}{c_s^+} - \frac{\mu^-}{c_s^-}} & \text{if} \quad n = -1 \\ 0 & \text{else.} \end{array}$$

The initial condition $\tau(-1) = 0$ becomes thus

$$A - \frac{2\tau_0^B \frac{\mu^+}{c_s^+}}{\frac{\mu^+}{c_s^+} - \frac{\mu^-}{c_s^-}} = 0.$$

So reintroducing the value of A, we get the expression of the interface traction stress for $n \geq 0$

$$\tau(n) = 2\tau_0^B \frac{1}{1 + \frac{\mu^- c_s^+}{\mu^+ c_s^-}} k^n,$$

where k is defined by (C.3). Performing a similar resolution for the velocity or reintroducing this solution in the second equation of (C.4), one gets

$$\dot{u}(n) = -2\tau_0^B \frac{c_s^-}{\mu^-} \left(1 + \frac{1}{1 + \frac{\mu^- c_s^+}{\mu^+ c_s^-}} k^n \right).$$